# CARBIDE PRECIPITATE DEACTIVATION AND NODULE CHARACTERISTICS IN THIN WALL DUCTILE IRON (TWDI) CASTINGS

By

**OCHULOR Ezenwanyi Fidelia**
B. Eng. (Hons.) FUTO, Owerri, M.Sc. (Lagos)
(019046005)

Thesis Submitted to the School of Post Graduate Studies, University of Lagos in partial fulfillment of the requirements for the degree of Doctor of Philosophy (Ph.D)

in

Metallurgical and Materials Engineering

DEPARTMENT OF METALLURGICAL AND MATERIALS ENGINEERING,
UNIVERSITY OF LAGOS, LAGOS. NIGERIA

JANUARY, 2016

## ABSTRACT

Ductile iron (DI) thin section profiles (≤ 3mm) known as Thin Wall Ductile Iron (TWDI) offer significant potentials in automotive applications because of their high strength with good ductility, wear resistance, castability, machinability and good fatigue properties. "Globally" as-cast TWDIs in many foundries suffer macrostructural and microsructural defects such as solidification shrinkages, coldshuts, misrun, incomplete filling, carbide precipitation, poor graphite morphological characteristics, which jeopardize the enhancement of mechanical properties required for automotive applications. Production of "defect-free" TWDI castings is hindered by difficulty in channeling molten metal appropriately into the mould cavity. This study considers the effect of casting design and sprue/metal head height on mould filling, microstructure and mechanical properties of TWDI casting. The suppression of carbide formation and non-nodular graphite is dependent on the nodularisation and inoculation treatments (liquid treatments), hence the effect of nodularisation treatment temperatures of $1450^0$C-$1550^0$C is investigated. This study also investigates effect of incorporation of 2-12 wt. % aluminum dross (AlDr) and 1-6 wt.% rice husk ash (RHA) on thermal properties of moulding sand, the microstructure and mechanical properties of TWDI castings, as literature on these is found to be scanty. The results show that side feeding casting design enabled completely filled mould cavities. At metal/sprue height of 50 mm the melt could not push through the gating channel, but as it is increased from 100-350 mm, complete mould-fill is achieved. However, between 200 mm and 350 mm, carbide precipitates and flow related defects namely; misrun, coldshut, incomplete filling and air entrapment are evident. These defects significantly lower the strength and ductility of TWDI. Desirable nodularity ratings above 90%, good nodule count of 450-610 nodules/mm$^2$, reduction of deleterious carbides with improved elongations are achieved at $1450^0$C-$1470^0$C melt treatment temperatures. Below $1450^0$C and above $1490^0$C, poor nodularity and nodule count with reduction in ductility are obtained. RHA significantly reduced the thermal conductivity of the moulding sand from 1.631 to 1.141 W/m. K, for 0 to 6 wt. % RHA in sand mix respectively, (a 30% reduction). TWDI castings with nodularity ratings above 90%, high nodule count above 1000 nodules/mm$^2$, high strengths of 564, 575 and 596 MPa for 2, 3 and 4 mm respectively, occurred at 4 wt. % RHA addition. High ductility of 4.7, 5.8 and 6.1 for 2, 3 and 4 mm thick samples respectively occurred at 6 wt. % RHA additions. This study has shown that sound TWDI castings are achievable with proper gating design and dimensions. Sprue/metal height is an important gating system parameter to be considered during casting of TWDIs. Lower treatment temperatures of 1450 $^0$C and 1470 $^0$C are adequate for good nodularity and nodule count. Incorporation of RHA to silica moulding sand significantly reduced thermal conductivity leading to reduction in cooling rate with controlled carbide precipitation and enhancement of nodular graphite of desired morphological characteristics.



**Keywords:** Thin wall ductile iron, Carbide precipitate, graphite structure, solidification, nodularity, nodule count.

# CHAPTER ONE

# 1.0 INTRODUCTION

## 1.1 Background of the Study

Ductile Iron (DI) is a cast iron type with its graphite occurring as microscopic spheroids and constituting about 10 vol. %. DI also referred to as nodular iron or spheroidal graphite iron was first discovered by Keith Dwight Millis in 1948. After a decade of intensive developmental work in the 1950s, DI had a phenomenal increase in use as an engineering material during 1960s, and the rapid increase in commercial application continues today. An unusual combination of properties is obtained in DI because the graphite occurs as spheroids rather than flakes as in grey iron. The spherical morphology is obtained by adding a very small but specific amount of magnesium or cerium or both to molten iron of a proper composition. The base iron is severely restricted in the allowable contents of certain minor elements that can interfere with the graphite spheroid formation. The added Mg reacts with S and O in the molten iron and changes the morphology of graphite formed. Control procedures are being developed to make the processing of DI more effective.

The graphite spherical shape is responsible for enhanced mechanical properties as compared with the flake shape in grey cast iron (Skaland, 1993). The shape (nodularity) and number (nodule count) is established when the metal solidifies, and cannot be altered in any way except by re-melting the metal (www.Mid-AtlanticCasting.com). The difference between the various grades of ductile iron is in the nature of the matrix around the graphite. The microstructure varies with composition and cast cooling rate. The as - cast can be cooled slowly in the sand mould to obtain a minimum hardness and if the casting has sufficiently uniform sections, it can be shaken out of the mould while still at temperature above the critical temperature and then normalized. The matrix structure and hardness can be changed by heat treatment as high ductile grades are usually annealed so that the ferrite matrix is entirely free of carbon (C).

Thin wall ductile irons (TWDI) are DI thin section profiles of thickness $\leq$ 3mm (Labrecque *et al.,* 2005; Fras *et al.,* 2009). Currently TWDI offer viable potential in lightweight automotive parts for energy saving requirements. Some of these automotive parts are control arms, connecting rods, exhaust manifolds and wheel rims (Fras *et al.,* 2013).

Automotive part manufacturers are often faced with challenges such as the need for fuel consumption reduction, emission control and manufacturing cost reduction. The solution to all these challenges is to reduce vehicle weight to save material and energy. For example a reduction of 100 kg translates to a fuel efficiency improvement of 0.4 km per litre (Dogan *et al*., 2003). It should be noted that cast parts (steel and cast irons) constitute a significant proportion of vehicle weight (~ 60%). In view of the current need for light weight materials for energy saving, cast iron part manufacturers are exploring weight reduction through cast redesigns with thinner walls so as to discourage substitution of cast iron parts with low density materials such as aluminium and its alloys, magnesium and its alloys etc. Many automotive components are produced using DI owing to its high strength and good ductility, good castability, machinability and fatigue strength (Fras *et al*., 2013). However, as section thickness is reduced (2-3 mm), metallurgical quality becomes impaired as defects associated with incomplete filling with carbide precipitation and poor graphite morphological characteristics become evident in as-cast structure (Bockus *et al*., 2008; Halvaee and Ardestani, 2014). Thus, many foundries encounter challenges in the production of TWDIs requiring desired microstructure and mechanical properties for automotive applications. If the mechanical properties and flawless nature of standard wall thickness DI castings could be replicated in TWDI, it would be possible to extend its areas of application (Davis *et al*., 2000). In recent years, many researchers such as Bockus *et al*., (2008) and Fras *et al*., (2013) considered TWDI as a substitute for steels and light alloys owing to its properties of high strength, good ductility, good castability, machinability, with high wear and fatigue resistance. However, the inherent problem of improper mould filling, deleterious carbides precipitation, poor nodularity and nodule count has deterred its production in many foundries.

### 1.2 Statement of the Problem

TWDI readily find application in automobile and related manufacturing sector as it offers tremendous weight savings without sacrificing functional properties relative to conventional materials. However, the widespread application of TWDI castings to other critical areas of the automotive industry has been limited by inability to achieve sound/defect free castings resulting from incompletely filled moulds as shown in Figures 1a and 1b vis-a-vis Figure 1c which is properly filled. There is also the

problem of low plasticity associated with the casting resulting in low ductility and poor crack propagation resistance. Literatures in this area identified the presence of massive carbide precipitates and poor graphite shape characteristics (Figure 2a) in TWDI castings (Bockus *et al*., 2008; Halvaee and Ardestani, 2014). These features are responsible for poor functional properties of TWDI castings such as reduced ultimate tensile strength (UTS), low ductility, poor crack propagation resistance and machinability. The carbide precipitate is a brittle phase, which negatively affects the mechanical properties of the iron matrix while poor nodularity and nodule counts negatively affect tensile strength and percent elongation (Davis, 1996). Non-nodular graphite structures act as stress concentration sites which aid crack propagation and ultimately cause untimely failure of TWDI components.


a b c

Figure 1: TWDI melt flow defects (a) Coldshut and Misrun (b) Incomplete filling and sand inclusion (c) Sound TWDI casting

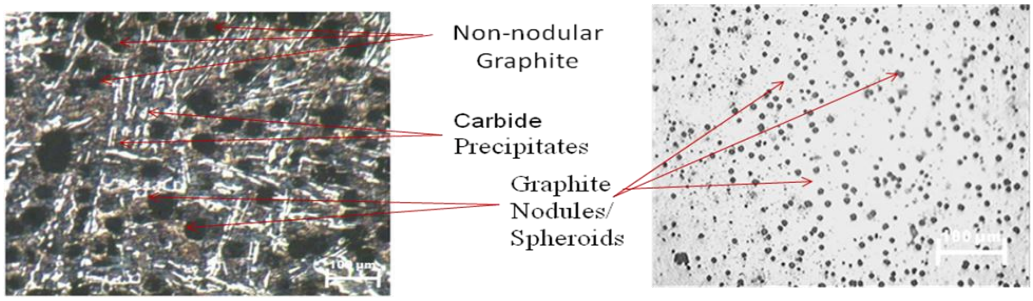


a b

Figure 2: Microstructure of TWDI showing (a) carbide precipitate (b) graphite nodules

**1.3 Aim and Objectives of the Study**

This study is aimed at developing a molten metal processing technique that would eliminate mould fill defects, formation of primary carbides and non-nodular graphite

structures in ferritic/ pearlitic TWDI cast for automotive application. The objectives of the study are to:

1) Eliminate melt flow and solidification related defects in 2-4 mm TWDI through gating and sprue designs and to determine mechanical properties of these castings.
2) Proffer appropriate melt treatment temperatures for the control of carbide precipitates and non-nodular/ deformed graphite structures in TWDI castings.
3) Develop mouldable insulating sand mix for control of cooling rate and solidification during casting of TWDIs exhibiting as-cast microstructure and mechanical properties meeting ASTM Spec. No. A536-80 (grade 80-50-06) for automotive application.
4) Quantitatively determine nodule count and nodularity in relation to carbide precipitate control and mechanical properties of castings using ASTM A247 and E407 standard procedures.

### 1.4 Scope and Delimitation of the Study

This study focuses on the production of defect and carbide free as-cast TWDI through the use of existing charge make-up and melting conditions as practiced in the industry. Silica sand moulds of particle size 250-300 μm incorporating 2-12 wt. % aluminium dross (AlDr) and 1-6 wt. % rice husk ash (RHA) as additives. There is no change in technology and no follow-up heat treatment to avoid increase in production cost. The above procedures will help control nodularisation treatment and cooling rate of TWDI. Thus strength and ductility of TWDIs for automotive application will be enhanced.

### 1.5 Significance of the Study

The need to develop and advance sustainable technology for production of TWDI as lightweight alternative continues to prompt studies on TWDI castings. Current trends in the design of vehicle components have been focused on the production of TWDI casting to save materials and energy. In general, there is an increasing demand for 3 mm thick or less TWDI with high strength to weight ratio (Stefanescu *et al*., 2002). DI application for lightweight components is presently limited by inability to produce defect and carbide free $\leq$ 3 mm wall parts (Sheikh, 2008). This study will help develop and advance sustainable practice for production of defect and carbide free

TWDI castings. Austempered ductile iron (ADI), currently attracting technological and academic interest cannot be achieved without sound DIs. The cost per unit strength ratio of several engineering materials (Gagne, 2006) shown in Figure 3 indicates that DI offsets weight benefits of aluminum alloys, and as such represents a competitive substitute for aluminum alloys, if the challenges associated with TWDI castings production is resolved. This development in TWDI production will help create jobs and enable compliance with Federal Government local content policy in automotive part production.

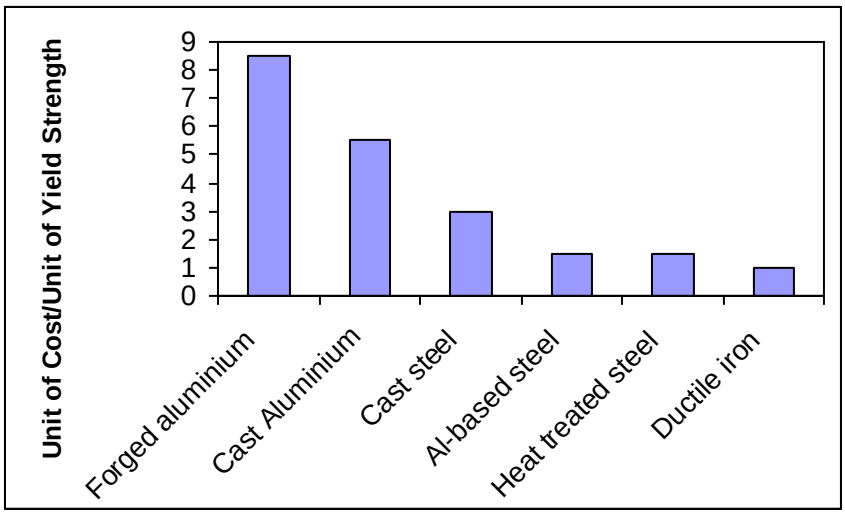


Figure 3: Relative cost per unit Yield strength of various engineering materials (Gagne, 2006).

### 1.6 Definition of Terms

I. **Brinell hardness number (BHN**) - commonly used to determine the hardness of materials like metals and alloys based on a Brinell scale.

II. **Bull Eye Graphite Structure –** DI structure where ferrite envelops around graphite nodules, surrounded by pearlite matrix.

III. **Carbide**- It is an extremely hard brittle compound of carbon with either iron or strong carbide forming elements, such as chromium, vanadium and molybdenum.

IV. **Carbon Equivalence (CE)** - $CE(wt\%) = C + \frac{(Si + P)}{3}$ (1)

V. **Cementite**- It is also known as iron carbide with chemical formula $Fe_3C$.

VI. **Eutectic irons**- Cast irons having 4.3 wt.% carbon content.

VII. **Ferrite**- This is known as α-ferrite (α-Fe) or alpha iron and is a term used for pure iron, with a body-centered cubic B.C.C crystal structure.

VIII. **Head/ Sprue Height –** Height of molten metal in the sprue.

IX. **Hypereutectic irons**- Cast irons having more than 4.3wt. % carbon content.

X. **Hypoeutectic irons**- Cast irons having less than 4.3wt. % carbon content.

XI. **Inoculation**- This is a melt treatment involving the addition of silicon alloy called an inoculant to facilitate heterogeneous nucleation of graphite.

XII**. Mechanical Properties**- These are properties that determine how a metal responds to external load such as tension, compression, shear and torsion; example is hardness, yield strength, ductility, tensile strength and toughness.

XIII. **Microstructure**- This is the structure of a metal as revealed by an optical metallurgical microscope.

XIV. **Nodularisation**- This is a melt treatment involving the addition of magnesium or magnesium alloy to the melt, with the purpose of changing graphite shape from flake to spheroids/nodules.

XV. **Nodularity**- This is the number of graphite particles in a hundred that are sufficiently rounded.

XVI. **Nodule count**- It is the quantity of nodules per square millimeter on a polished surface examined under a microscope at 100 magnifications (100 X).

XVII. N**on-nodular graphite structures**- These are non- spherical graphite.

XVIII**. Pearlite-** It is usually a lamellar (alternate plate) combination of ferrite and cementite ($Fe_3C$), formed by eutectoid decomposition of austenite upon cooling by diffusion of carbon atoms.

XIX. **Percent elongation** (% elong.)- It is a measure of ductility of a metal and is calculated as: Percent Elongation = $\frac{\text{Final length - Initial Length}}{\text{Initial Length}} \times 100$ (2)

XX. **Solidification time (Ts)** –The total time from pouring to the completion of solidification.

XXI**. Thermal conductivity (TC**) - A measure of the ability of a material to conduct heat. Moulds with high thermal conductivity remove heat faster from the molten metal, causing it to solidify rapidly.

XXII. **Ultimate tensile strength (UTS**) - often shortened to tensile strength (TS) or ultimate strength, is the maximum stress that a material can withstand before fracture.

# CHAPTER TWO
# 2.0 LITERATURE REVIEW

## 2.1 TWDI Castings

Applications of DI have continued to increase steadily over the years due to its relatively low production cost, ease of recycling, evolution of a wide range of microstructures and mechanical properties. In recent times, there has been increased attention paid to the production of TWDI castings. Fras *et al*., (2013) in their study on the technological aspects of TWDIs, observed that thin wall wheel rim made of DI can have the same weight but better mechanical properties than their substitutes made of aluminium alloy. It has also been stated (Davis *et al*., 2000) that if the mechanical properties and flawless nature of standard wall thickness of DI castings could be replicated in TWDI, it would be possible to extend its areas of application. The literatures in this study are categorized into: casting and gating design; charge material composition; cooling rate; evolved microstructure i.e., matrix type, nodularity ratings (shape and size of nodules) and nodule count present; melt (inoculation and nodularisation) treatment techniques. The cooling rate directly impacts on the solidification kinetics and consequently influences shape and size of nodules formed, nodule count and matrix phase present.

## 2.2 Casting and Gating Design

The gating and riser systems designs have been identified as critical elements in the production of high quality sand casting (Manjunath *et al*., 2012; Katzarov 2003; Lee *et al.,* 2001). A gating system is expected to lead clean metal into the mould cavity at an optimal rate with efficient temperature distribution and minimal turbulence. Improper design of gating and risering systems would result in cold shut and shrinkage porosities. Therefore, adequate care is necessary in designing gating and risering systems for improved yield of defect free castings. Masoumi *et al.,* (2005) studied the effect of gating design on mould filling, where direct observation was employed to experimentally investigate the flow pattern by pouring molten metal of aluminum alloy A413 into a sand mould. The results showed that an increase in the width of the gate with a constant thickness resulted in the variation of mould filling. A considerable effect of the geometry of a gate with a constant cross sectional area on flow pattern was observed, which primarily resulted from the change of the metal

front pressure at the entrance. The study concluded that casting design is primarily done on a shop floor on trial and error basis and those conventional experimental routes are often used for design and development of product with optimum process parameters. Many gating systems are developed using principles with little or no understanding as to what happens in the mould filling stage. A lack of true gating understanding causes many foundries to produce poor quality castings. A gating system is expected to lead clean metal into the mould cavity at an optimal rate with efficient temperature distribution and minimal turbulence. Gorny (2009) observed that temperature and velocity drop have an effect on heat exchange rate and consequently on cooling during mould filling. A higher cooling rate will produce a higher degree of under-cooling at the beginning of eutectic solidification. Thus, to achieve TWDI castings with homogeneous structure only a few in-gates are necessary in its gating design. When metal flows in a very turbulent manner, excessive liquid metal surface area is exposed to air (Campbell, 2000). This maximizes the possibilities for oxide formation. As the oxide mix with the metal, the oxide films and particles become entrapped within the alloy. These trapped oxide inclusions form regions of high, localized stress when a load is placed on them. Experimental observations by Pavlak (2008) established that the main factor for smooth filling of the mould is the pouring process and the position of in-gates. The shape of the pouring basin also has significant influence on the smoothness of the pouring stream and on the oxide formation. Pouring distance is another significant factor that impacts on the formation of oxides and consequently increases porosity in cast structure. The points at which the falling streams of melt fall down into pouring basin define the smoothness of melt velocity (laminar or turbulent) through the sprue. The adoption of higher pouring distance produced higher density index, which means that the sample has more pores and oxides inclusions. This is expected, because during filling of the cup, the melt stream from higher distance has more time to react with air and get contaminated with oxides. Also, the stream which is flowing from longer distance has higher kinetic energy and causes higher turbulent movement compare to the stream that flows from shorter distance. Design optimization of gating system by fluid flow and solidification simulation of front axle housing (Manjunath *et al.*, 2012) has shown that by adopting the parting line and pressurized gating system, the fluid flow was smooth and air was expelled without any entrapment inside the mould cavity. Thus, fluid heat distribution was good with no cold shuts. The study by Hassan *et al.*, (2010) indicated that stepped

runner gating system improves graphite nodule characteristics, and positively influenced hardness and strength of TWDI casting. The study by Voigt *et al.,* (1997) revealed that fluidity of thin sections increased as head height increased and fluidity dropped as wall thickness is reduced. The head height also influence metal fill velocity (Voigt, 2002); as head height is increased, the fill velocity also increased, and this tends to increase fillability. However, increasing head height can lead to decrease in the temperature of the initial metal entering the mould cavity and in turn decreases fill distance. Thus, increasing head height on thin wall component produced mixed results. Naveen and Sunil (2014) in their study on casting simulation for sand casting of flywheel developed and presented a 3D component model using casting simulation software ADSTEFAN to evaluate possible casting defects for sand casting of flywheel. Notable conclusions from this study are: by adopting the pressurized gating system, the fluid flow was smooth and air was expelled without any entrapment inside the mould cavity. Simulation showed that the molten metal was able to fill the mould within the desired time. Therefore, fluid heat distribution was good and no cold shut was observed.

### 2.3 Charge Material Composition

The study on effect of rare earths (RE) on microstructure formation and mechanical properties of TWDI castings, observed that 2 mm thick specimen with varied RE contents showed uniform distribution of graphite nodules (Choi *et al.,* 2004). Chill zones form in all specimens, but the extent of the chill zones is less in the specimens containing more RE, resulting in increased graphite formation. This suggest that the presence of RE retards the nucleation of cementite (carbide). As the size of the samples increase, more irregular shaped graphite nodules form due to prolonged solidification time (Choi *et al.,* 2004). Graphite nodules enveloped by ferrite in pearlite matrix was obtained by the use of RE. The layer of ferrite around the graphite nodules between the alloys containing RE and without RE suggests that the addition of RE influences the formation of ferrite. The layer of ferrite on the surface of graphite nodules is thicker in the specimens containing RE than in those without RE. The amount of ferrite has a strong influence on the ductility of ductile iron. In specimens that do not contain RE, the spheriodization of graphite nodules is strongly influenced by sample thickness. It was also observed that as the size of the samples increase, more irregular shaped graphite nodules tend to form due to the longer

solidification time. The same tendency is reported by Onsoien *et al.*, (1997) that nodularity decreases with increasing solidification time. With the addition of RE, shorter solidification time is appropriate for obtaining improved nodularity in TWDI castings (2-8 mm thickness samples).

The effect of the use of Lanthanum on DI increased nodule count to 467 but with low nodularity in the range 81-83% (Sheikh and Iqbal, 2007). Inoculants having Calcium (Ca), Barium (Ba) or Strontium (Sr) along with a ferrosilicon alloy can be used to improve nodularity and nodule count in DI castings (Skaland, 2005). Nucleation of graphite starts at higher temperature in the hypereutectic casting than in the eutectic and hypoeutectic castings; the under-cooling is lower for hypereutectic castings (Pedersen and Tiedje, 2007). Therefore, it is necessary to minimize the levels of any carbide promoting elements, as carbides will segregate in the structure. Berdin *et al*., (2001) emphasized on the necessity to minimize the levels of any carbide promoting elements, as carbides will segregate in the structure. Shinde *et al.*, (2012) observed that addition of copper in DI favours nucleation of adequate primary eutectic graphite but decreases overall nodule count. Forrest (2006) recommended that it is important to ensure that the optimum level of sulphur in melt is within 0.008 – 0.012%. The study observed that in situations where pure magnesium is used as a one step desulphurization and nodularization treatment, the control of the sulphur content is less critical because the reaction removes most of the sulphides. However, in this case the inoculation practice becomes more difficult and other materials need to be considered to achieve good nodularity. Mullins (2006) observed that RE elements reduce the magnesium requirement for a particular set of nodule count and nodularity. As some of the magnesium measured is in the form of magnesium sulphide, final iron sulphur level affects the magnesium needed to result in nodular graphite. Maximum nodularity cannot be achieved by keeping magnesium residue at just 0.02% as this quantity will deteriorate the nodule shape from full spheroicity. Increase in the silicon/carbon mass ratio is effective for decreasing chill in TWDI castings and chill is inhibited in melt containing 0.01% bismuth even though the thickness of the specimen is 2 mm (Takeda *et al.*, 2010). Soedarsono1 *et al.*, (2011) in their study on the effect of carbon equivalent (CE) on microstructures of TWDI castings observed insufficient data to conclude the relation between CE and carbide formation. However, it was noted that CE has an effect on nodularity and nodule count of TWDI. Ruxanda *et al.*, (2002) and David *et al.*, (2004) suggested that the minimum CE value

should be 4.3 for general thickness and CE values of 4.75- 4.92 should be used for 3-5 mm thickness. Stefenescu *et al.,* (2002) in their study on the tensile properties of TWDI suggested CE of 4.72 for preventing carbides in 100% ferritic matrix. Javaid *et al.,* (2001) reported that carbide free 3 mm thick DI plates were obtained in sand moulds by using DI having CE ranging from 4.5- 5.08 %.

**2.4 Cooling Rate**

Significant increase in nodule count would occur when cooling rate increases, as a consequence of the thin walls (Borrajo *et al.,* 2002). The result is possible because of the under - cooling that takes place during solidification of the thinner sections, which activates a large number of substrates for heterogeneous nucleation of graphite. Hypoeutectic compositions exhibit smaller nodule count than eutectic and hypereutectic irons, particularly when thin sections are cast. TWDI castings show very large nodule counts, both the nodularity count and the average sphericity increase as the section thickness decreases. Cast section < 6 mm with solidification time < 50 seconds show very high average sphericity and nodularity.

The above reviewed study contradict the observed microstructure of as-cast TWDI castings in many operating foundries, many of which end up with massive carbide precipitation. Sheikh (2008) identified that fast cooling of thin section DI castings requires special consideration to produce carbide-free castings. When changing the cooling rate, effects similar to those discussed for grey iron also occur in DI, but section sensitivity of the material is lower. However, Stefanescu *et al.,* (2003) observed that pouring very thin sections in DI presents danger of massive carbide phases in the as-cast. The work of Pedersen and Tiedje (2008) on under-cooling and nodule count in TWDI castings, shows that the eutectic alloys have higher under-cooling (lower $T_{min}$) but similar nodule count compared with hypereutectic castings. The difference is because the nucleation of graphite takes some time in the eutectic alloys of thin walled castings. As the nucleation of graphite starts at higher temperature in the hypereutectic castings than in the eutectic and hypoeutectic castings, the under-cooling will be lower for the hypereutectic castings. Simultaneous nucleation of graphite and austenite could account for the lower $T_{min}$ in the eutectic casting but experiments with hypoeutectic castings show that this does not have an influence on the $T_{min}$.

Pouring very thin sections in DI presents danger of massive carbide phases in the as-cast (Bockus *et al.*, 2008). Heat exchange in the metal-mould system is essential to the kinetics of cooling and solidifying of TWDI, which starts to solidify during mould filling and is characterized by high cooling rate (Gorny, 2009). The ultimate physical and mechanical properties of cast metal depend partly on intrinsic factors such as chemical composition, cooling rate during solidification, heat and mechanical treatments after solidification. On the other hand, the properties equally depend on extrinsic factors namely metal cleanliness, additives for microstructure control, casting design, riser and gating design, solidification rate control, and temperature control before solidification (Kalpakjian, 2008).

**2.5 Evolved Microstructure (Matrix type and graphite nodule characteristics)**

The solidification microstructure produced directly influence mechanical properties, this is because the amount and form of graphite in DI are determined during solidification and cannot be altered by subsequent heat treatment (Bockus *et al*., 2008; www.Mid-AtlanticCasting.com). The principal factor in determining the different grades of DI is the matrix structure. Graphite particles in DI are characterized by a combination of mechanical properties (tensile strength, toughness, wear and crack propagation resistance). This combination is strongly influenced by metal-matrix microstructure, impurities present and graphite particle morphology. High toughness and good crack propagation resistance are attributed to spheroidal graphite shape. Thus, the morphology of graphite particles is a critical parameter towards improved strength and elongation characteristics of DI. Spherically shaped graphite particles known as “nodules” act as “crack arresters” with increase in toughness, ductility and crack propagation resistance of TWDI part (Figure 4a). This critical shape of graphite can only be obtained by means of good “nodularisation” technique (Iacoviello and Di Cocco, 2003). The wall thickness of spheroidal graphite cast iron has very strong effect on the graphite size and shape (Bockus and Zaldarys, 2009). Li *et al.*, (2000) identified three typical shapes of graphite nodules, which are shown in Figure 4.

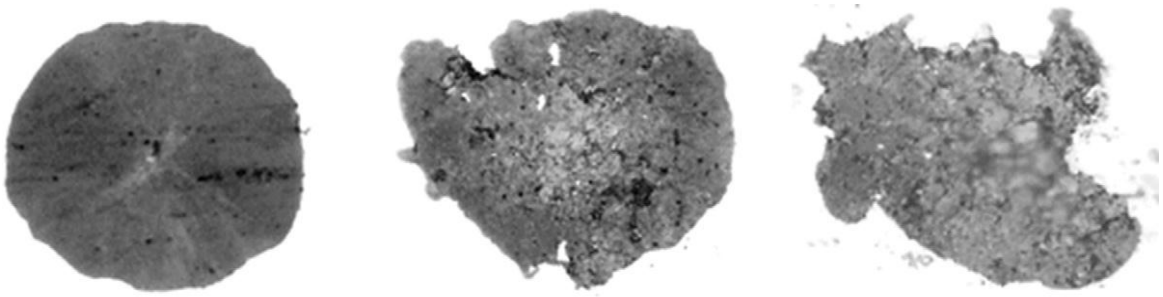

a b c

Figure 4: Types of graphite shapes (a) Spherical/nodular, (b) Slightly nodular and (c) Non-nodular (Li *et al.,* 2000).

The desired shape is that shown in Figure 4a, as it has a high degree of sphericity. Those in Figures 4b and 4c are undesirable as these shapes propagate cracks from stress concentration points and are poor in nodularity, tensile strength, fatigue strength and ductility (Li *et al.,* 2000).

**2.6 Melt Treatment**

Chemically, DI has the same composition as grey iron and is an iron-carbon-silicon alloy. The common feature in all DI's is the spherical shape of the graphite nodules. These graphite nodules are nucleated on small inclusions during solidification. Therefore, the relative possibilities for nucleation and growth depend upon foreign particles in the melt, either as trace impurities or as deliberate additions (Flemings, 1974). When comparing un-inoculated and inoculated irons, differences in microstructure are easily revealed, with strong effect on the final mechanical properties of the cast. Through proper inoculation, the graphite nucleation and eutectic under-cooling of iron can be controlled to give the iron its required service properties and minimize defects (Olsen *et al*., 2009).

Carbide precipitates in these irons are often caused by poor practice or faded inoculants and fast cooling rates rather than by higher levels of carbide promoting elements such as chromium (Olsen *et al.,* 2009). Mullins (2006) also agrees with this assertion that inoculation, if done correctly, controls nodule count, reduces or eliminates carbides, produces the correct mechanical properties, improves machinability and decreases shrinkage. Inoculation introduces additional nuclei that cause graphite precipitation and reduces the under-cooling and formation of carbides.

However the liquid treatment of DI is known to be more complex than that of grey iron (Bockus *et al.,* 2008; Bockus and Zaldarys, 2009). For melts of eutectic and

hypoeutectic compositions used to cast plates of thickness 3-50 mm, the results show that wall thickness of spheroidal graphite cast iron has very strong effect on the graphite size and shape. The time after spheroidal treatment (holding time) affects the graphite shape and elongation, but has negligible effect on the tensile strength and hardness of castings. The graphite shape is also influenced by the holding time as shown in Table 1 (Bockus *et al.,* 2008).

Table 1: Effect of holding time on the mechanical properties of ductile iron (Bockus *et al.,* 2008)

| Parameter | Time after Spheriodization (minutes) | | | | |
|---|---|---|---|---|---|
| | 5 | 10 | 15 | 20 | 25 |
| Tensile Strength (MPa) | 572 | 562 | 582 | 585 | 588 |
| Elongation (%) | 12.8 | 12.8 | 11.4 | 8.6 | 5.7 |
| Hardness (BHN) | 192 | 187 | 199 | 197 | 192 |

The wall thicknesses of spheroidal graphite cast iron are found to have very strong effect on the graphite size and shape of the castings (Bockus and Zaldarys, 2009).
The inoculation effects on microstructure and mechanical properties of DIs have shown that nodule count influences the pearlitic content of as-cast DI (Sangame and Shinde, 2013). Increased nodule count decreases the pearlite content and tensile strength with increase in elongation. This improves ductility and reduces the tendency of chill carbides formation. The matrix consistency is influenced by nodule count. Increase nodule count produces a finer and more homogeneous microstructure. This refinement of the matrix structure reduces the segregation of intercellular harmful carbides or degenerated graphite. Inoculation practices used to improve nodule count often make the nodules more spherical. Thus, high nodule count is generally associated with improved nodularity with increase in toughness.

### 2.7 Summary of Literature review

The review of these literatures show some knowledge gaps in vital areas such as casting designs for proper mould filling, effects of sprue height gating components whose dimensions directly effect metallostatic pressure of advancing melt, nodularisation treatment temperature and mould thermal properties on microstructure and mechanical properties of cast TWDI.

# CHAPTER THREE

# 3.0 METHODOLOGY

## 3.1 Theoretical Framework

This study is predicated on two major concepts; the first is that solidification takes place by nucleation and growth. This is based on the kinetics of phase transformation where the decrease in free energy (ΔG) between the liquid and the solid phase provides the driving force for solidification i.e.

$$\Delta G \approx \frac{\Delta T}{T_m} \quad (3)$$

Where $T_m$ is the melting temperature and ΔT is the under-cooling.

The second concept is based on heterogeneous nucleation theory. Heterogeneous nucleation of graphite is an important aspect of cast iron metallurgy (Minkoff, 1983), where nucleation and growth during solidification is dependent on introduction of foreign particles either as deliberate additions or as trace impurities.

In general, cast iron is an alloy of iron with carbon (up to about 4%) and silicon (up to about 3.5%), which is not malleable in as- cast condition. Depending primarily on composition, cooling rate and melt treatment, cast iron can solidify according to the thermodynamically metastable Fe-$Fe_3C$ (cementite) system or the stable Fe-Gr (graphite) system. The important micro-structural components found in cast irons are graphite, carbide, ferrite, pearlite, martensite, austenite and bainite (Davidson, 2003). Graphite is the stable form of pure carbon in cast iron. Its important physical properties are low density, low hardness and high thermal conductivity and lubricity. Graphite shape, which can range from flake to spherical, plays a significant role in determining the mechanical properties of cast irons. The flakes act like crack in iron matrix and under stress, aid crack propagation while the graphite spheroids act like "crack arresters" resulting in better mechanical properties (Jappes *et al*., 2006). In grey irons, flakes of graphite develop as iron freezes and because of its low specific gravity, may amount to ~ 6 to 17% of the total iron volume.

Carbide or cementite is an extremely hard brittle compound of carbon with either iron or strong carbide forming elements, such as chromium, vanadium and molybdenum (Davis, 1996). Massive carbides precipitation increases the wear resistance of cast iron, but render it brittle and very difficult to machine. Ferrite is the purest phase of iron in cast iron. In conventional DI, the presence of ferrite phase produces lower

strength and hardness, but high ductility and toughness. In austempered DI (ADI), extremely fine-grained accicular ferrite provides an exceptional combination of high strength with good ductility and toughness (Davis, 1996). Ferrite may be defined as a solution of the normal temperature body centered -cubic crystalline form of iron and small amount of carbon and as such is relatively soft, ductile and of moderate strength. In cast irons, silicon is present as solute in ferrite phase. Silicon hardens and strengthens the ferrite, giving it a hardness of 100 - 140 BHN, 20 - 30 percent elongation, and tensile strength of 345 – 483 MPa, depending on the silicon content. Structurally, ferrite in cast irons may occur as free ferrite or as ferrite in pearlite. Free ferrite predominates in malleable irons and nodular irons of maximum ductility. In grey irons, ferrite occurs mainly as a constituent of pearlite when soft iron is desired. For incomplete graphitization, the iron structure will consist of graphite and pearlite (or a mixture of pearlite and free ferrite or pearlite and free cementite). Pearlite consists of a mixture of ferrite and cementite arranged in alternate lamellae. Pearlite in most cast irons is strong (~ 827 MPa) and moderately hard (about 200 - 230 BHN) and has some ductility, which conforms to standard of many engineering applications. The amount of pearlite present in cast irons depends on the degree of graphitization of the iron. In grey and nodular irons, the combined carbon percentage reflects the presence of pearlite. A pearlite grey iron will contain about 0.5 - 0.9 percent carbon in solution. Lower carbon content usually indicates the presence of free ferrite, the latter increasing as the percentage combined carbon decreases.

The chemical composition of DI and the cooling rate of the casting directly affect its tensile properties through evolving matrix structure (Davis, 1996). All regular grades of DI can be made from the same iron provided that the chemical composition is appropriate so that the desired matrix microstructure can be obtained through controlled cooling of the casting or by subsequent heat treatment.

The common grades of DI contain spherical graphite but differ primarily in the matrix structure. The matrix difference is the result of differences in composition, cooling rate and heat treatment carried out on the casting. Faster cooling rates associated with thin sections promote pearlite formation; slower cooling rates favour ferrite formation (Caldera *et al.,* 2005). Minor differences in composition or the addition of alloys may be used to enhance the desired microstructure. DI is not a single material, but a family of materials offering a wide range of properties obtained through microstructural control. The common feature that all DIs is the near spherical shape of the graphite

nodules. These nodules act as crack-arresters and make DI “ductile”. This feature is essential to the quality and consistency of DI and is measured and controlled with a high degree of assurance by competent DI foundries. Mechanical properties are determined by the percentage of graphite nodules present in the DI structure and matrix structure present.

The graphite parameters/characteristics of utmost importance are nodularity and nodule count. Nodularity is usually measured as a percentage, and defined as the number of graphite particles in a hundred that are sufficiently rounded. This percentage must meet or exceed the established internal standard. Nodule count is usually defined as the number of graphite particles in a specified unit of area. It is the quantity of nodules per square millimeter on a polished surface examined under a microscope at 100 magnifications (100 X). To be considered, a nodule should be round or nearly so. When the length of a graphite particle is two or more times its diameter, it is no longer considered a nodule. What is and what is not a nodule is part of what is called the nodularity rating, which can be from 0 - 100%. A 100% rating which is the ultimate target means that all nodules are completely round, no matter how many they are (Mullins, 2003).

The formation of eutectic carbides during solidification affects the volume fraction of graphite produced, because carbide and graphite compete for the carbon present in the liquid iron (www.Mid-AtlanticCasting.com). A carbide content of 15 vol. % would have used 1% C for its formation and thus reduces the available carbon for graphite nucleation by approximately one-third (Davis, 1996). Thus, any treatment or procedure that increases the nodularity and nodule count of DI will control carbide precipitation and non-nodular graphite structures. Castings with poor nodularity display lower ductility (tensile elongation) and often do not meet minimum tensile and/or impact strength requirement. The carbide phase embrittles the castings and non-nodular graphite particles act as stress raisers and reduce the fatigue strength of the iron (Li *et al.,* 2000). As-cast microstructure is governed by the solidification process and also by the subsequent eutectoid transformation. Inoculation practice and cooling rate control the nodule count, while the matrix microstructure depends on the conditions at which the eutectoid reaction occurs. Faster cooling rates associated with thin sections, promote pearlite formations and slower cooling rates favour ferrite formation (Gorny and Tyrala, 2013). Faster solidification rates generally accompany rapid cooling rates through austenite transformation, besides section thickness, the

total mass of the castings relative to the amount of mould material and the nature of the mould medium, influence the cooling and solidification rate.

When discussing the metallurgy of ductile iron, the major factors influencing structure, which need be addressed, are chemical composition, cooling rate, liquid treatment and heat treatment procedure (Ahmadabadi *et al*., 1994; Fras and Lopez, 1998; Ratto *et al*., 2001).

### 3.2 Chemical Composition

Production of TWDI is influenced by a large number of metallurgical, technological, heat transfer and design parameters. The first step in the production of castings is the careful selection of the charge materials. Charge materials determine the average size of graphite spheroids. For 30 percent or > 50 percent steel scrap in the charge the average spheroids diameter are found to be 57 µm and 33 µm respectively (Bockus and Dobrovolskis, 2004). The amount of steel scrap affects metallic matrix structure and increases the pearlite formation (Krestyanov and Some, 1991). Cast irons typically contain 2-4 % C with high silicon concentrations and a greater concentration of impurities than steels. The carbon equivalent (CE) of cast iron determined from Equation 4 helps in distinguishing the grey-irons in the microstructure containing graphite and the white iron where the carbon is present mainly as cementite.

$$CE(wt\%) = C + \frac{(Si + P)}{3} \qquad (4)$$

Where C, Si, P are the weight % of carbon, silicon and phosphorus respectively. A high cooling rate and a low CE favours the formation of white cast iron while a low cooling rate and high CE produces grey cast iron. The graphite structure is affected by the carbon content. If initial metal does not contain enough amount of carbon, then graphite particles are of compact shape. The metallic matrix structure is affected not only by carbon equivalent but also by C/Si ratio. As this ratio increases, the proportion of ferrite decreases and the proportion of pearlite increase. For common cast irons, the main elements of the chemical composition are carbon and silicon. High carbon content increases the amount of graphite or $Fe_3C$. High carbon and silicon contents increase the graphitization potential of the iron and its castability. The manganese content varies as a function of the desired matrix and it can be as low as 0.1% for ferritic irons and as high as 1.2% for pearlitic iron (manganese is a strong

pearlite promoter). The minor elements, phosphorus and sulphur, are the most common and are always present in the composition. These can be as high as 0.15% for low-quality iron and may be considerably less for high-quality iron, such as ductile iron or compacted graphite iron.

The spheroidizing elements (magnesium and cerium) can change graphite shape from flake, through compacted to spheroidal. The most widely used element for the production of spheroidal graphite is magnesium. The amount of residual magnesium required to produce spheroidal graphite is usually 0.03-0.05% and the precise level depends on the cooling rate. A higher cooling rate requires less magnesium while too low a level produces insufficient nodularity, which in turn causes deterioration of the mechanical properties of the iron. But if the magnesium content is too high, carbide precipitation is promoted. The presence of anti-spheroidizing minor elements may result in graphite shape deterioration leading to complete graphite degeneration. Therefore, upper limits are set on the amount of deleterious elements to be accepted in the composition of cast iron. These values can be influenced by the combination of various elements and by the presence of RE elements in the composition (Choi *et al.*, 2004). Furthermore, some of these elements can be deliberately added during liquid processing in order to increase nodule count. Alloying elements have in principle, the same influence on structure and properties as for grey iron because better graphite morphology allows more efficient use of the mechanical properties of the matrix. Alloying is more common in ductile than in grey iron (Soinski *et al.*, 2014).

### 3.3 Cooling rate

The cooling rate is largely dependent on the size of the casting. The section thickness affects solidification and cooling rates through the austenite transformation range (Gorny and Tyrala, 2013). Solidification and cooling rates influence nodule count, presence of carbides and the amount of ferrite and pearlite formed. Solidification time is a function of casting volume and surface area, mould heat extraction rate, pouring temperature and the thermal properties of the solidifying metal. For a given mould medium and solidifying metal, solidification time from Chovrinov's Rule as given in Equation 5 depends on the volume-to-surface area ratio (V: SA).

$$Ts = Bs\left(\frac{V}{A}\right)^2 \qquad (5)$$

The total solidification time is the time from pouring to the completion of solidification; V is the volume of the casting; A is the surface area; and B is the mould constant, which depends on the characteristics of the metal being cast (its density, heat capacity, and heat of fusion), the mould material (its density, thermal conductivity, and heat capacity), the mould thickness, and the amount of superheat (El Rayes, 2007). The smaller the V: SA ratio, the faster the solidification rate. Solidification starts from the outside walls and proceeds inwards. External corners solidify first and quickly. As solidification progresses, the mould is heated and the rate of heat extraction reduces, leading to slower solidification rate at the casting center. When a small portion of mould is surrounded by fairly large sections of metal, the moulding mass is heated to a high temperature leading to reduction in heat transfer from the solidifying metal. If poured at higher temperatures, the solidification rate is slower. The increased heat must be removed before the metal starts solidifying and the mould is heated to a higher temperature with reduction in the heat transfer rate. DI under-cools before the bulk of the eutectic solidify. The degree of under-cooling increased when all other metallurgical factors are kept constant. When the eutectic under-cooling temperature is low ($<1138^0$C), iron is prone to chill carbide formation. Effective inoculation decreases the chill-forming tendency.

Labrecque *et al.,* (2005) demonstrated from experimental study that reducing the heat extraction capacity of the moulding material reduces the under-cooling level and the cooling rate of TWDI castings. This allows the production of such castings exhibiting as-cast microstructure and mechanical properties meeting ASTM specifications. The study also concluded that using a moulding material with a lower thermal conductivity improves the homogeneity of the microstructure and mechanical properties of TWDI castings. Thermal capacity and conductivity of mould material influence the heat transfer and solidification rates. Rates are faster in metal moulds and the resultant DI nodule count is extremely high. As section thickness increases, solidification rate decreases, resulting in lower nodule counts. The as-cast microstructure is governed by the solidification process and also by the subsequent eutectoid transformation. The inoculation practice and the cooling rate control the nodule count, while the matrix microstructure depends on the conditions under which the eutectoid reaction occurs (Skaland, 1991; Venugopalan, 1990). For a given chemistry and nodule count, the cast cooling rate through the austenite transformation range determines the final matrix structure. Faster cooling rates associated with thin

sections, promote pearlite formations and slower cooling rates favour ferrite formation (Gorny and Tyrala, 2013). Faster solidification rates generally accompany faster cooling rates through austenite transformation. When the total weight of metal poured is increased, moulding materials are heated to a higher temperature as the metal solidifies and cools to the transformation temperature range. This slows down the cooling rate, providing longer times for ferrite formation. Nodule count is important in controlling the final matrix. For the same cooling rate, increasing amounts of nodules provides more centers for ferrite nucleation and growth with increasing amounts of ferrite. Owing to this, late and multiple inoculation increases nodule count (Cebanne and Gagne, 2010) and ensures that maximum amount of ferrite is achieved. The conflicting effects of section thickness must be recognized as thinner sections generally promote high nodule count and have a tendency to increase the amount of ferrite. It also increases the cooling rate, and reduces the ferrite content. The final matrix structure depends on nodule count, cooling rate (section thickness) and chemistry (carbon equivalent and other alloy factors).

### 3.4 Liquid Treatment

The liquid treatment of DI is more complex than that of grey iron. The two stages for the liquid treatment are:

- Nodularisation/ Modification: this consists of magnesium or magnesium alloy treatment of the melt, with the purpose of changing graphite shape from flake to spheroids/nodules. This treatment is dependent on the amount of residual magnesium in the melt as the element has strong affinity for both sulphur and oxygen, which are also in the base iron. Sufficient quantities should ensure higher nodule count and high nodularity ratings. A high nodule count in a DI matrix can be an advantage in many casting applications. It generally implies little or no primary carbides, reduction in the tendency to form carbides in thinner casting sections, promotion of ferrite matrix in as-cast, reduction of micro-segregation, reduction of diffusion time during heat treatment and homogenization of the structure. It also implies high graphite fraction, which reduces porosity and improves nodularity and mechanical properties (Goodrich, 1990).

- Inoculation: Post-inoculation is done after the magnesium treatment to increase nodule count and suppress carbide formation. Increasing the nodule count is associated with less chilling tendency and a higher as-cast ferrite/pearlite ratio. Inoculation is very important as it assists in providing enough nucleation sites for the carbon to precipitate as graphite rather than iron carbide i.e., cementite, $Fe_3C$ (Skaland, 2005). This is done by preventing under-cooling to temperatures below the metastable eutectic temperature where carbide (white) structures are formed (Olsen *et al.*, 2009).

In the light of these metallurgical factors, this research will focus on these parameters to investigate their effects on control of carbide precipitates and non-nodular graphite in TWDI.

The desire to improve the mechanical properties of TWDI castings cannot be achieved if sound casting without defects is not achievable. The first approach employed in this study is ensuring proper filling of mould cavity. Some of the defects associated with improper mould filling include cold shut, mis-run, blow holes and sand inclusions. Proper mould filling is dependent on appropriate gating system design and ensuring adequate melt fluidity. The gating design influences molten metal flow pattern, which in turn affects temperature distribution/heat transfer and modifies the progression of solidification (Gorny, 2009). These processes affect final microstructure or phases formed after solidification of the as-cast TWDI component.

It has been stated that good gating system design could reduce the turbulence in the melt flow, minimize air entrapment, sand inclusion, oxide film and dross (Shafiee, 2009; Ahmad and Hashim, 2011; Naveenkumar and Bharat, 2014). Gating system components are choke diameter, sprue height, the runner and in-gate dimensions. Among these components, the sprue height has significant influence on the metallo-static pressure of the melt, which consequently affects mould filling efficiency (Voigt, 2002). Scanty information is available in the literature on its influence in ensuring defect free TWDI castings. Mould filling is the first stage (from pouring to solidus temperature) of metal cooling (Gorny, 2009). Melt flow influences solidification time ($t_s$), and this is an important parameter capable of altering the microstructure and mechanical properties of the cast part. It is therefore, the focus of this study, among other issues, to investigate the effect of casting design and sprue height dimension through three different melt feeding modes namely side, top and bottom, on mould filling and quality of TWDI castings.

The second approach is ensuring adequate treatment (inoculation and nodularisation) to facilitate sufficient number of sites for heterogeneous nucleation of graphite. These two melt treatments are vital, there should be a synergy between them for production of good nodules; high nodule count and carbide free TWDI. Nodularisation treatment is carried out first, followed by a two-step inoculation treatment. Nodularisation treatment is a modification treatment where the shape of the graphite is changed from flake to spheroid or nodules. This shape is responsible for the peculiar properties of DI. Inoculation is followed immediately to facilitate heterogeneous nucleation for increased nodule count and suppression of carbide formation. The ferroalloys of ferro-silicon-magnesium and ferro-silicon used for these treatments have fading tendencies as the time after spheroidal treatment has a significant effect on nodularity (Bockus and Zalgarys, 2009). The practice in the Foundries (Nigerian Foundries, Ota, Ogun State, Nigeria) is to pour the melt into the mould within a maximum period of seven minutes after the nodularisation treatment is done or the treatments would be ineffective. The nucleating property is understood as the number and potency of nuclei formed by the alloy addition (Skaland, 2005). Sufficient graphite nucleation is required to avoid formation of carbides that arise due to high solidification rates in TWDI (Algarasamy, 1992). In industrial practice, this treatment occurs over a wide temperature range. Since temperature is a parameter that affects spontaneity of chemical reactions, it is imperative to experimentally determine the effective temperature or temperature range that will produce best yield of treatment in terms of graphite characteristics. This will be the second focus of study.

During casting, heat transfer occurs between the hot liquid metal and the mould (i.e. the heat transfer medium) and the temperature decreases from that of the cast to the surrounding temperature. The process involves three successive stages namely: initial cooling of the melt, the solidification of the liquid metal and finally the cooling of the solid metal (Abed, 2011). The process of solidification, the change of liquid to solid metal after pouring into the mould, is the defining event in the life cycle of the casting (Rihan, 2010). The time involved in this transition may be as short as seconds or as long as hours depending upon the casting process, the size of the casting, the chemical composition of the metal being cast, the manner in which solidification occurs, and the subsequent solid state treatment, which determines the ultimate microstructure and properties (mechanical and physical) of the casting (Schmidt, 2010). The heat exchange in the metal-mould system is essential to the kinetics of cooling and

solidification of a casting, especially in TWDI, which start to solidify during mould filling (Gorny, 2009). The goal here is to control the solidification event so that the desired microstructure and mechanical properties in the final product is obtained. The modification of thermal properties of mould media to control cooling rate would be the third focus of the study.

### 3.5 Materials

The raw materials are silica moulding sand, steel scraps, DI returns ferro-silicon and ferro-silicon magnesium alloys, aluminium dross and rice husk ash.

### 3.6 Equipment

(1) Optical Emission Spectrometer with calibration standards.
(2) Mechanical Tensile Testing machine
(3) Brinell Hardness Testing machine.
(4) Metallography facilities
(5) Induction Furnace
(6) Metallurgical Optical Microscope
(7) Mould Making Boxes

### 3.7 Experimental Methodology

#### 3.7.1 Materials Preparation

ASTM E2349 standard mould making procedures are employed using the prescribed moulding equipment. The moulding sand consists of silica sand, bentonite, additives (coal dust and starch) and water. The dimensions of the drag and cope are 410 mm x 375 mm with a height of 110 mm. The patterns for the cavity, runners and in-gates are placed in the drag section and rammed adequately, while the sprue pattern of height 100 mm is placed in the cope. Melting is carried out in a Dual Trak induction furnace model 1250-5R. The pressurized casting technique is used in the ratio 3:2:1, which translates to cross sectional area at sprue: cross sectional area at runner: cross sectional area at ingate. A total of two patterns are made for each thickness i.e., 2, 3 and 4 mm. The research samples' pattern is 150 mm by 150 mm for three thicknesses (2, 3 and 4 mm). Tapping is done after appropriate carbon equivalent (CE) of 4.35 - 4.70 % is reached in the molten metal at $1560^0$C. Nodularizing treatment is performed by the sandwich method using ferrosilicon magnesium alloy granules covered with

mild steel chips in a preheated treatment ladle. The ferrosilicon inoculants are added in the melt stream while transferring the molten metal from the treatment ladle to a preheated pouring ladle. Further inoculation is carried out while pouring into the moulds using powdered ferrosilicon in the stream by using a perforated pipe. The moulds and contents are allowed to cool for eight hours before shake out. The composition of the charge materials used is shown in Table 2. These standard procedures are maintained for all experiments performed during the study.

Table 2: Chemical composition of charge materials

| Charge | wt. (Kg) | % of Charge | C (Ch.Comp. %) | Si (Ch.Comp.%) | Mn (Ch.Comp.%) |
|---|---|---|---|---|---|
| Mild Steel | 300 | 60 | 0.1 | 0.1 | 0.2 |
| Ductile Iron Returns | 170 | 34 | 0.6 | 0.4 | 0.2 |
| Ferro Silicon | 7 | 1.4 | 0.00 | 70 | 0.00 |
| Graphite | 23 | 4.6 | 70 | 0.00 | 0.00 |

### 3.7.2 Gating/Feeding Design

Different gating process assembly/feeding modes are designed namely: (1) Bottom Feeding (2) Top Feeding and (3) Side Feeding. Figures 5(a, b and c) are the process assembly diagrams for the studied process.

In the top feeding mode (Figure 5a) the molten metal enters into the mould cavity directly from the top with no runners or in-gates, however, a ceramic filter is installed at bottom of the pouring basin to remove slag impurities. In side feeding, the melt flows from the sprue to side gates through a runner placed at the side of mould cavity as shown in Figure 5b. Lastly, in the bottom feeding (Figure 5c), the in-gates are placed under the mould cavity so as to fill the mould by gravity and then by capillary action. A total of three moulds are prepared for each feeding mode for the three thicknesses.

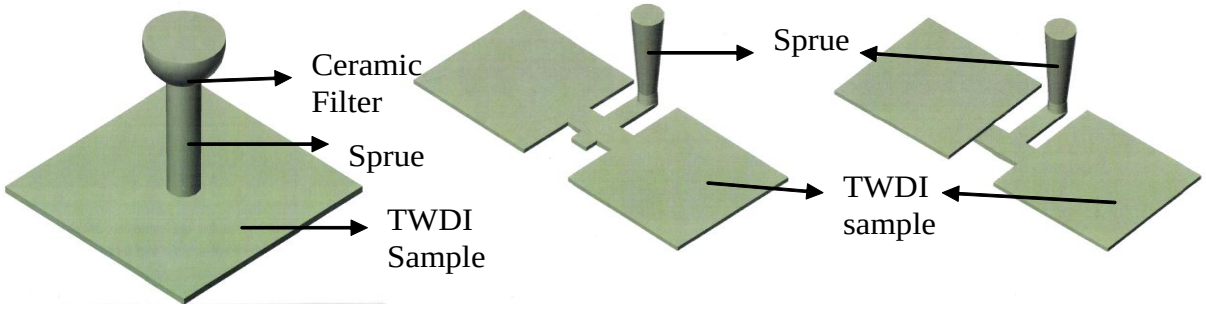


a b c

Figure 5: Process assembly diagram for (a) Top (b) Side (c) Bottom Feeding

A total of three moulds are prepared for each feeding mode for the three thicknesses. The dimensions of the gating components and pattern plates are shown in Tables 3a and 3b respectively.

Table 3a: Dimension of Gating Components

| Component | Bottom Feeding(mm) | Top Feeding (mm) | Side Feeding (mm) |
|---|---|---|---|
| Sprue (inlet/outlet diameter) | 2mm- 14.74/11.22<br>3mm- 15.90/12.09<br>4mm- 16.73/12.72 | 2mm-12.40/9.44<br>3mm-13.40/10.1<br>4mm- 14.07/10.7 | 2mm-14.74/11.22<br>3mm-15.90/12.09<br>4mm-16.73/12.72 |
| Runner | 8.119 X 8.119 | - | 8.119 X 8.119 |
| Ingates | 2mm- 2 X 8.24<br>3mm- 3 X 5.49<br>4mm- 4 X 4.12 | - | 2mm- 2 X 8.24<br>3mm- 3 X 5.49<br>4mm- 4 X 4.12 |

Table 3b: Dimension of Pattern Plates

| Plate Thickness (mm) | Length (mm) | Width (mm) | Volume ($mm^3$) | Mass (kg) |
|---|---|---|---|---|
| 2 | 150 | 150 | 45,000 | 0.324 |
| 3 | 150 | 150 | 67,500 | 0.486 |
| 4 | 150 | 150 | 90,000 | 0.648 |

Macro-examination of the as-cast samples are done to determine best casting design in terms of mould cavity filling, surface finish properties and surface defects.

### 3.7.3 Effective Metal Head Height

Metal head height/pressure head/metal head is the vertical distance between the metal pouring height and the top surface of the casting or simply the height of the metal in the sprue. This parameter directly influences metallo-static pressure as shown in Equation 6. A higher metallo-static pressure gives higher velocity of molten metal resulting in higher fluidity. The head height should be sufficient to overcome the effects of surface tension, which inhibit filling of the mould cavity (Capadona and Albright, 1978). This is important to give the melt a longer flow distance.

*Metallostatic Pressure*, $P_m = \rho gh$ (6)

Where ρ is the metal density (kg/m$^3$), h is the height of liquid metal column (m) above the filling point and g is acceleration due to gravity (m/s$^2$).

The 2, 3, 4 mm thick patterns are used to make another set of moulds according to ASTM E2349 standard mould making procedures. The charge materials as shown in Table 3 are melted using the induction furnace and tapped at 1560$^0$C. The sandwich inoculation treatment method is used. The treatment is carried out in a preheated ladle by adding ferrosilicon-magnesium alloy as done previously and then transferred to the pouring ladle for discharge into the moulds. Pre and post inoculation using ferro-silicon is done in the melt stream during ladle transfer and also melt stream during mould filling. In this part of the work, a gating system component called the sprue height is varied in other to determine mould filling efficiency and properties of TWDI cast samples. Seven sprue heights are selected namely 50, 100, 150, 200, 250, 300 and 350 mm and patterns for these are made. The gating components dimensions used is shown in Table 4 for the side feeding as this design produces superior results in terms of proper mould filling. The moulds are labeled as shown in Table 4 and casting of the samples is done. It is observed that the castings made with a sprue height of 50 mm are defective and this is attributed to incomplete filling or poor run. Cast samples obtained with sprue heights of 100 – 350 mm appeared properly cast and thus subjected to property tests.

Table 4: Sprue height and sample designation

| S/No | 1 | 2 | 3 | 4 | 5 | 6 | 7 |
|---|---|---|---|---|---|---|---|
| Sprue Height (mm) | 350 | 300 | 250 | 200 | 150 | 100 | 50 |
| Sample Name | A1 | A2 | A3 | A4 | A5 | A6 | A7 |

### 3.7.4 Melt Nodularisation Treatment Temperature

The requirements of ASTM E2349 standard mould making procedures are employed as previously done. The side feeding design with sprue height of 100 mm is adopted here. The molten metal is first tapped at $1550^0$C into a preheated treatment ladle for the first treatment temperature using the sandwich method. This same procedure is repeated for treatment temperatures of $1530^0$C, $1510^0$C, $1490^0$C, $1470^0$C, $1450^0$C and $1430^0$C. The samples are labeled as in Table 5.

Table 5: Sample Designation and Treatment Temperatures

| S/N | 1 | 2 | 3 | 4 | 5 | 6 | 7 |
|---|---|---|---|---|---|---|---|
| Sample Name | T1 | T2 | T3 | T4 | T5 | T6 | T7 |
| Treatment Temperature, $^0$C | 1550 | 1530 | 1510 | 1490 | 1470 | 1450 | 1430 |

### 3.7.5 Modification of Thermal Properties of Moulding Sand

Aluminum dross is a by-product of aluminum smelting or aluminum foundries. It is a mixture of metallic aluminum and non-metal part mostly aluminum oxide, which usually forms on the surface of molten aluminum or its alloys by oxidation. It can be recycled to recover the valuable aluminum. The dross used is collected from Aluminum Rolling Mills, Ota, Nigeria after a recovery process is carried out on it. Its chemical composition is shown in Table B2 in the appendix.

Sieve analysis is carried out on the dross and only those with particles sizes of 250-300 µm were used. This is important so as to ensure uniform particle size to that of the silica sand used, as good surface finish in the TWDI castings is required in order to achieve desired mechanical properties.

Fifty (50) kg of rice husk, a by-product of rice milling is obtained from Ifo in Ogun State, Nigeria. Combustion of this agro-waste took place in a Gemco CFR 90337 electric furnace at $700^0$C, at the Foundry Shop of Federal Institute of Industrial Research (FIIRO), Oshodi, Lagos, Nigeria. After combustion and cooling, sieve analysis is conducted and only RHA particles between 250-300 µm are used for the moulding sand preparation. Chemical analysis of RHA is shown in Table B3 in appendix.

Using the standard composition of moulding sand as shown in Table 6, six different compositions of the moulds are prepared by adding varying weight percentages of

AlDr and RHA to the moulding sand as in Tables 7 and 8 respectively. The sand constituents are mixed using a Rhino model IRM-500 sand mixer with a mixing time of 5 minutes. It is important to note that the choice of the weight percentages of the additives used is based on a preliminary trial test conducted on 600 g of moulding sand in the Quality Control Laboratory of Nigerian Foundries Limited.

Table 6: Control Composition of green moulding sand

| S/No | Materials | Wt (%) |
|---|---|---|
| 1 | Silica Sand | 96.4 |
| 2 | Bentonite | 2.2 |
| 3 | Starch | 0.8 |
| 4 | Water | 0.4 |
| 5 | Coal Dust | 0.2 |

Table 7: Sand Specimen with wt% of Aluminum Dross (AlDr)

| S/No | 1 | 2 | 3 | 4 | 5 | 6 | 7 |
|---|---|---|---|---|---|---|---|
| Specimen | D | D1 | D2 | D3 | D4 | D5 | D6 |
| Wt.% AlDr | 0 | 2 | 4 | 6 | 8 | 10 | 12 |

Table 8: Sand Specimen with wt. % of RHA

| S/No | 1 | 2 | 3 | 4 | 5 | 6 | 7 |
|---|---|---|---|---|---|---|---|
| Specimen | RH | RH1 | RH2 | RH3 | RH4 | RH5 | RH6 |
| Wt.% RHA | 0 | 1 | 2 | 3 | 4 | 5 | 6 |

The result helped in the determination of the upper limit (i.e. 12 wt. % Al dross and 6 wt. % RHA) that are used, as higher weight percent produced adverse effect on the moulding sand properties based on the moulding sand property test conducted. The thermal property of importance in this work is thermal conductivity (which is the inverse of Thermal resistivity). This property of the sand mix is determined using KD 2 Pro Thermal Conductivity Meter (see Figure 6a), during moulding after the pattern is removed i.e. before coupling. The TR-1 sensor (Figure 6b) is used for thermal conductivity assessment. The read temperature is $29^0$C.

a b

Figure 6 (a) KD 2 Pro Thermal Conductivity Meter, (b) TR-1 sensor

Regression analysis of plots for the relationships studied are done, equations and regression coefficients predicted, to establish that the independent and dependent variables have significant relationships.

### 3.7.6 Microstructural characterisation of experimental TWDI castings

Samples for microstructural analysis are cut, ground and polished according to standard procedure outlined in ASTM Standard E3 for metallograghic analysis. The prepared samples are viewed in their unetched and etched (using 2% nital solution) conditions using a CETI Optical Metallurgical Microscope Model No. 0703552 at magnification of X100. Microstructural analysis i.e. nodularity, nodule count and matrix type are determined using manual procedure as outlined in ASTM A247 and E407 standard procedures.

$$\text{Nodularity \%} = \frac{Area\ (number)\ of\ acceptable\ particles}{Area\ (number)\ of\ all\ particles} \text{ X } 100 \qquad (7)$$

Nodule Count (graphite nodules/mm$^2$) is the quantity of nodules per square millimeter on a polished surface examined at X100 magnification.

### 3.7.7 Mechanical property characterisation of experimental TWDI castings

Brinell hardness test is carried out using a 10/3000kg indenter ball on tester model Foundrax/B.H.D/1003402 in accordance with ASTM E10 standard. Hardness test sample is shown in Figure 7a. Tensile property test (UTS and percent elongation) is carried out on a test piece with dimensions as shown in Figure 7b in accordance with ASTM E8 standard.

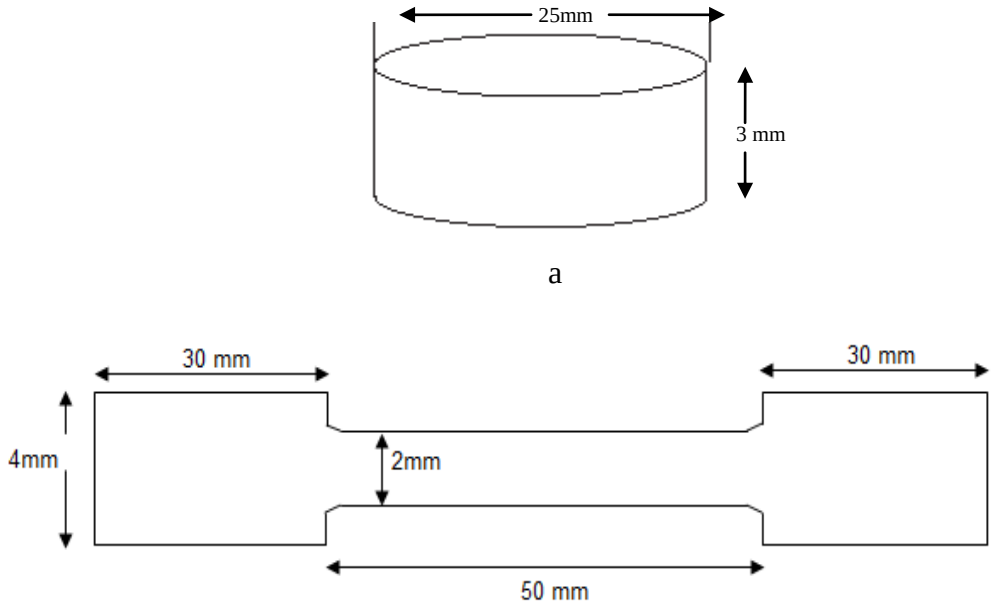


Figure 7: Dimension for standard test pieces a) Hardness Test b) Tensile Test

# CHAPTER FOUR

# 4.0 RESULTS AND DISCUSSION

## 4.1 Introduction

Microstructural and mechanical property variations are identified with respects to the parameters investigated. Nodularity, nodule count and matrix type are analyzed under microstructural properties while brinell hardness number, tensile strength and percent elongation values are analyzed under mechanical properties of TWDI cast samples.

## 4.2 Effect of casting/feeding procedure design

Observation by visual inspection revealed that the castings that are top fed, increased in thickness. This can be attributed to the metallo-static pressure exerted during casting owing to gravity pull and turbulence at the entry point. The pressures lift the cope and drag part of the mould up resulting in an expanded mould cavity. Consequently increased thickness of the cast occurs with defect in terms of larger thickness.

The castings obtained through bottom pouring/feeding are found defective due to incomplete mould filling. This is caused by inadequate pressure and velocity to push melt to fill mould cavity situated above in-gates. Thus, bottom feeding negatively affect mould filling efficiency for TWDI castings.

The castings produced through side gate feeds are properly filled for the three thicknesses used except for some of the 2 mm thickness, for which some are not completely filled. The success here can be attributed to reduction in turbulence. Visual observation has shown that side feeding procedure produces the best results in terms of effective mould filling and surface finish, but the problem of incomplete filling of some 2 mm thick castings need to be addressed. There is the need to improve on the molten metal fluidity and velocity for better mould filling and surface finish. These could further improve both the physical and mechanical properties of the TWDI castings. This need gave rise to the second part of the gating analysis experiment where the sprue/molten metal height are varied to determine its effect on mould filling ability and mechanical properties of the casting.

### 4.3 Effect of molten metal head / sprue height

The effect of sprue height on filling efficiency of TWDI castings is studied to solve the problem of incomplete filling observed in 2 mm samples. This parameter directly affects the metallo-static pressure of the melt as shown in Equation 6, which consequently affect fluidity and velocity of the melt. The gating design influenced the molten metal flow pattern. This in turn affects temperature distribution/heat transfer and modifies the progression of solidification. These processes affect final microstructure or phases formed after solidification of the as-cast TWDI component. It is important to note that castings obtained using sprue heights of 50 mm are defective and this is traceable to incomplete filling or poor run. This is attributed to insufficient metallo-static pressure to push melt into mould cavity. Cast samples obtained using sprue heights of 100 – 350 mm appeared properly cast and these are subjected to microstructure and property tests.

#### 4.3.1 Microstructural Analysis (Metal head / sprue height)

The micrographs of samples A1 (2, 3 and 4mm, Plates1-3) show smaller nodule count of 55, 105 and 190 nodules/mm$^2$ for 2, 3 and 4 mm thick samples respectively and presence of large proportion of carbide precipitates. This is also observed for A2 castings where the sprue height reduces to 300 mm. The A1 and A2 samples reveal some micro-voids and micro-porosity. These voids are also observed visually during sample preparation by metallography and could be attributed to air entrapment (Manjunath *et al.,* 2012) and insufficient graphitization (fast cooling from longer sprue heights). Microscopic observation reveals solidification related defects as seen in Plates 1-11, where transformation is stopped abruptly due to fast cooling and this is more evident in the 2 mm plates (Gorny, 2009). This feature is clearly observed in the unetched samples while the etched samples reveal massive primary carbide precipitates. The occurrence of significant temperature drop (under-cooling) at the advancing melt front in the samples is attributed to the use of longer sprue heights (Gorny, 2009). This initiate's early start of austenite transformation with insufficient time for the nucleation of the graphite phase as cooling rate is rapid in the thin plates (Skeikh, 2008). Heat transfer from high cooling rate leading to fast solidification rate through the austenite transformation region occurs. It is recommended that the sprue height should not be too high, but should be high enough to achieve the required

fluidity and velocity to push molten metal through to the mould cavity. The A4 samples (Plates 10-12) show improve nodule count of 520, 480 and 420 nodules/mm$^2$ and good nodularity > 90% for 2, 3 and 4 mm thick samples respectively with control of carbides. The A5 and A6 range samples demonstrate very good nodule count and nodularity but the samples A6 (2, 3 and 4 mm, Plates 16-18) possess desired microstructures in terms of nodule count, nodularity and absence of carbide precipitates. Typical bull's eye structure of graphite nodules surrounded by ferrite in a matrix of pearlite is evident in the A5 and A6 samples. However, the micrographs of samples A7 (2, 3 and 4mm, Plates 19-21) show poor nodularity and nodule count, non-nodular graphite and large proportion of carbide precipitates in its structure. The poor mechanical properties of these samples can be attributed to incomplete filling.

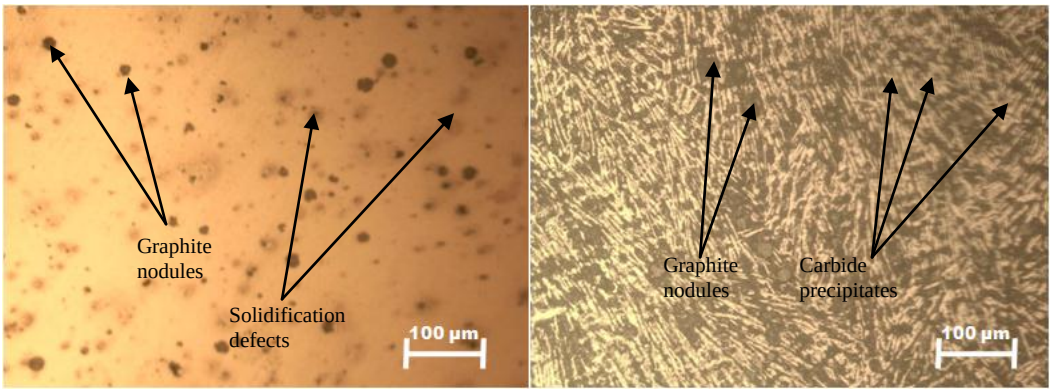


a b

Plate 1: Optical micrograph of 2mm thick section (a) unetched (b) etched of A1

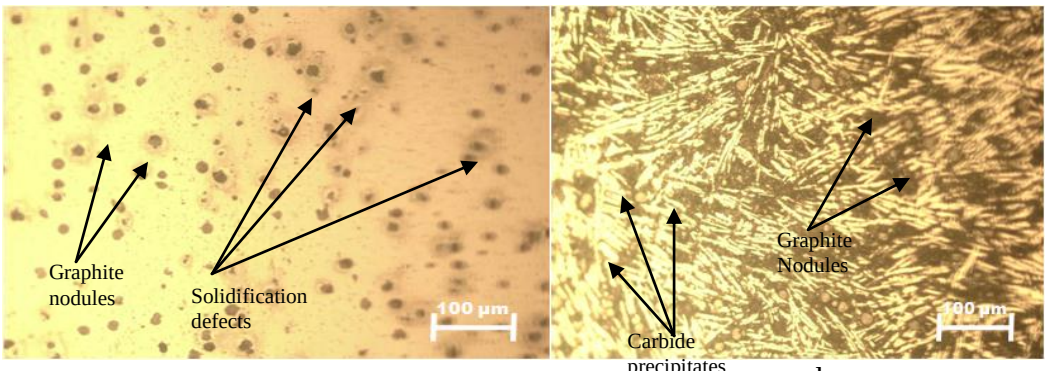


a b

Plate 2: Optical micrograph of 3mm thick section (a) unetched (b) etched of A1

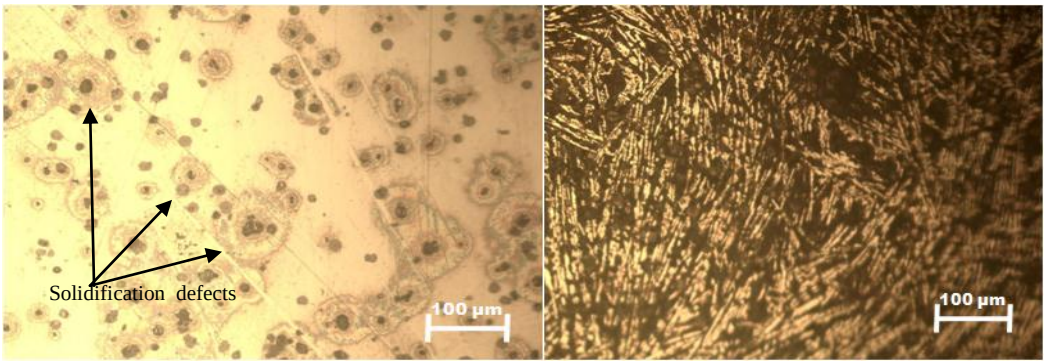


a b

Plate 3: Optical micrograph of 4mm thick section (a) unetched (b) etched of A1

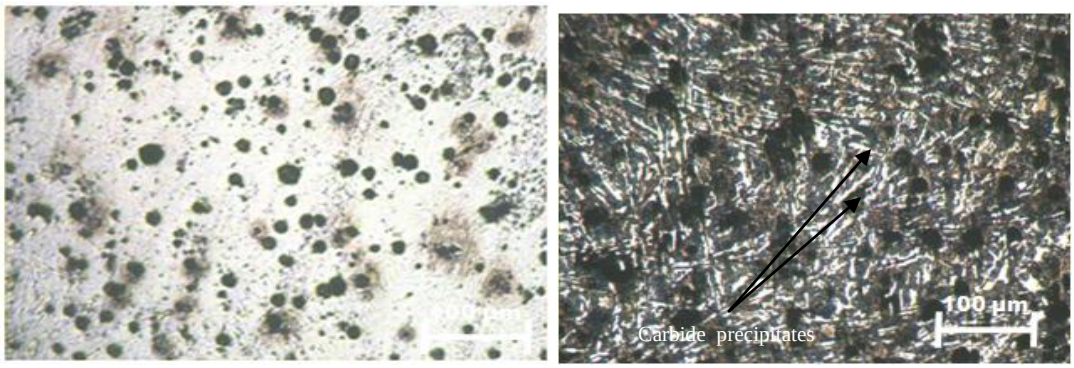


a b

Plate 4: Optical micrograph of 2mm thick section (a) unetched (b) etched of A2

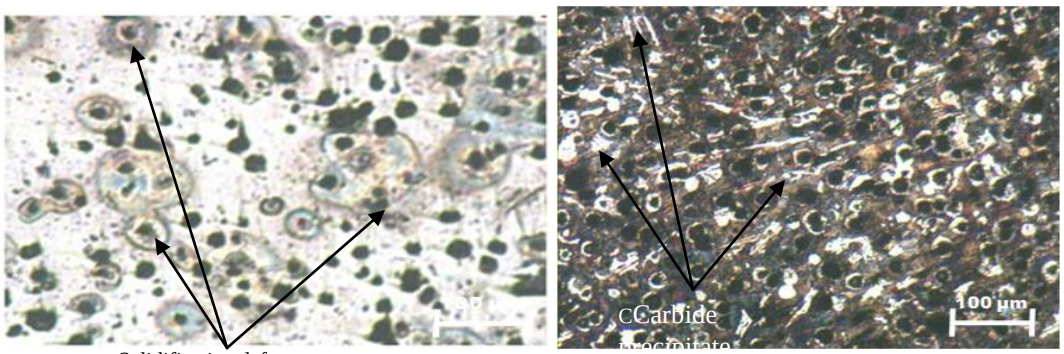


a b

Plate 5: Optical micrograph of 3mm thick section (a) unetched (b) etched of A2

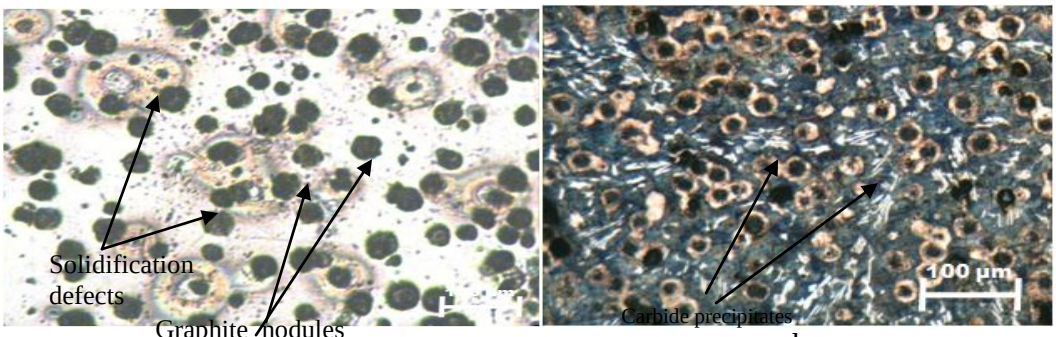


a b

Plate 6: Optical micrograph of 4mm thick section (a) unetched (b) etched of A2

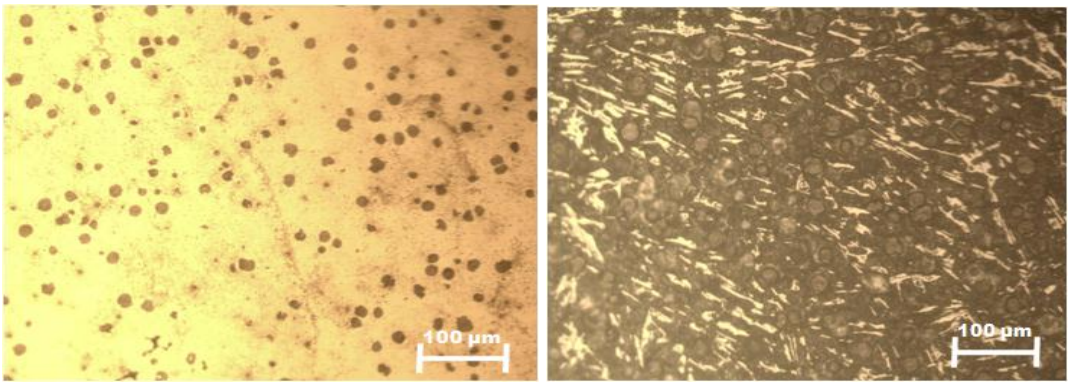


a b

Plate 7: Optical micrograph of 2mm thick section (a) unetched (b) etched of A3

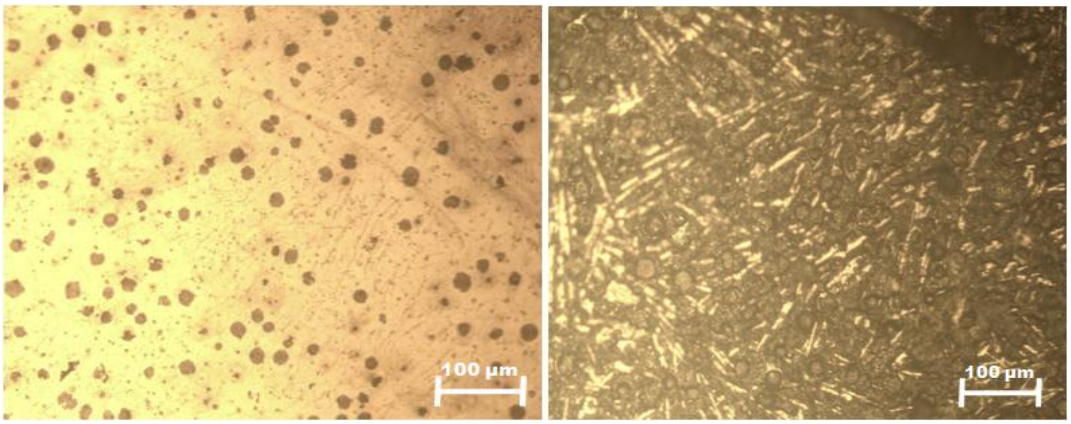


a b

Plate 8: Optical micrograph of 3mm thick section (a) unetched (b) etched of A3

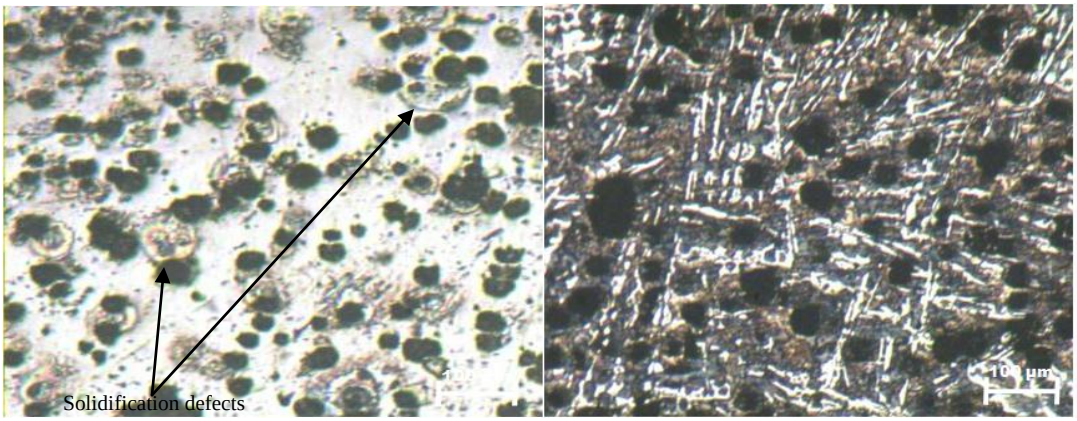


a b

Plate 9: Optical micrograph of 4mm thick section (a) unetched (b) etched of A3

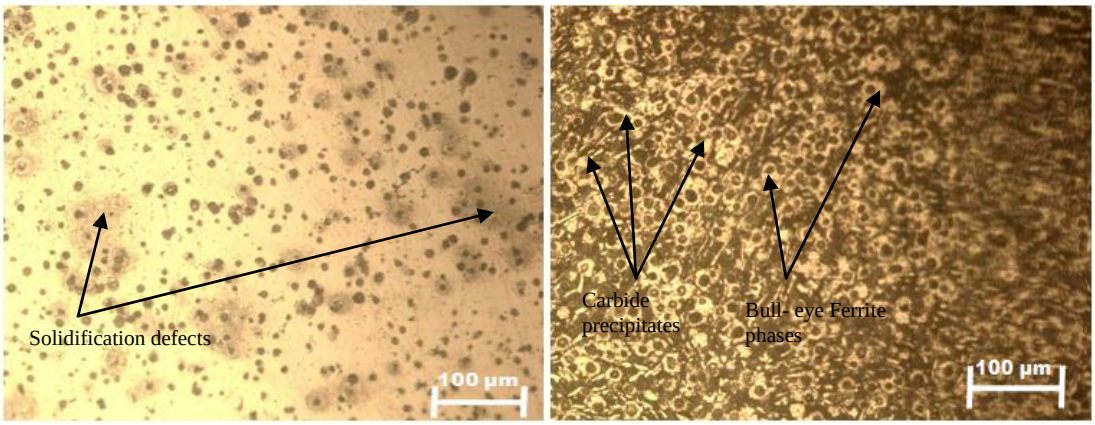


a b

Plate 10: Optical micrograph of 2mm thick section (a) unetched (b) etched of A4

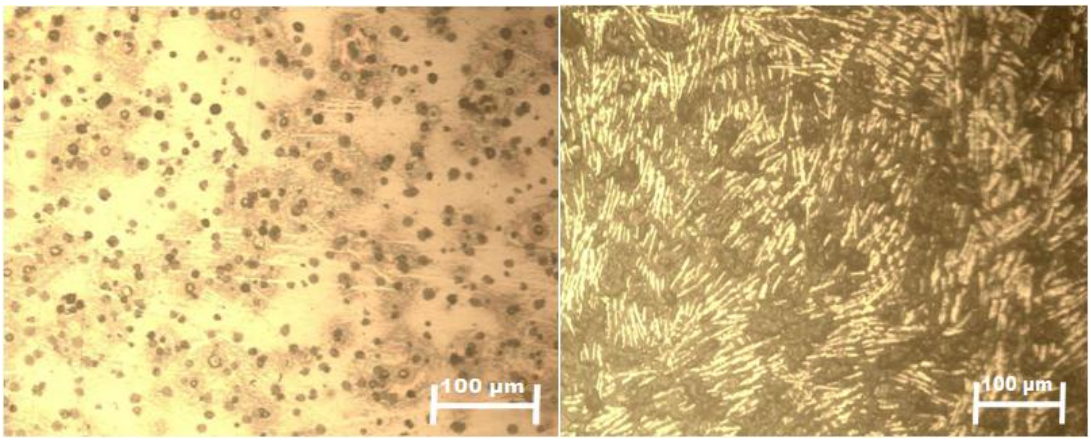


a b

Plate 11: Optical micrograph of 3mm thick section (a) unetched (b) etched of A4

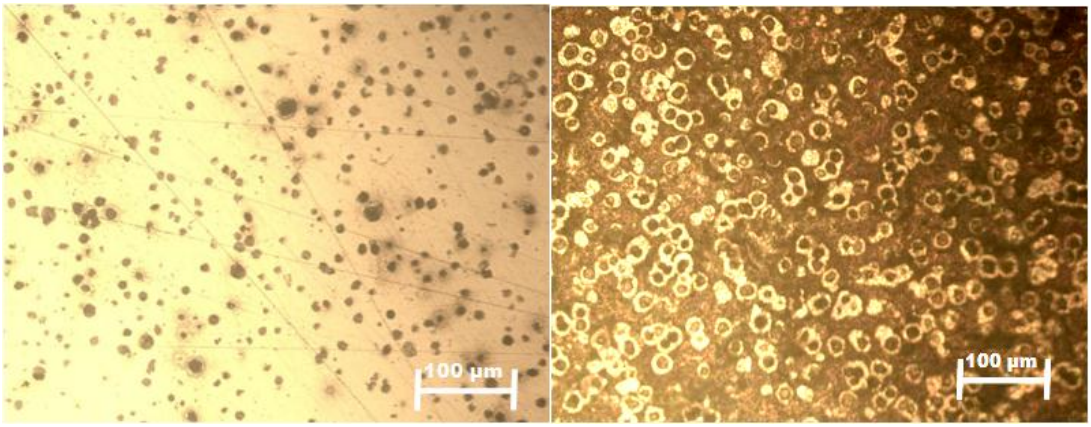


a b

Plate 12: Optical micrograph of 4mm thick section (a) unetched (b) etched of A4

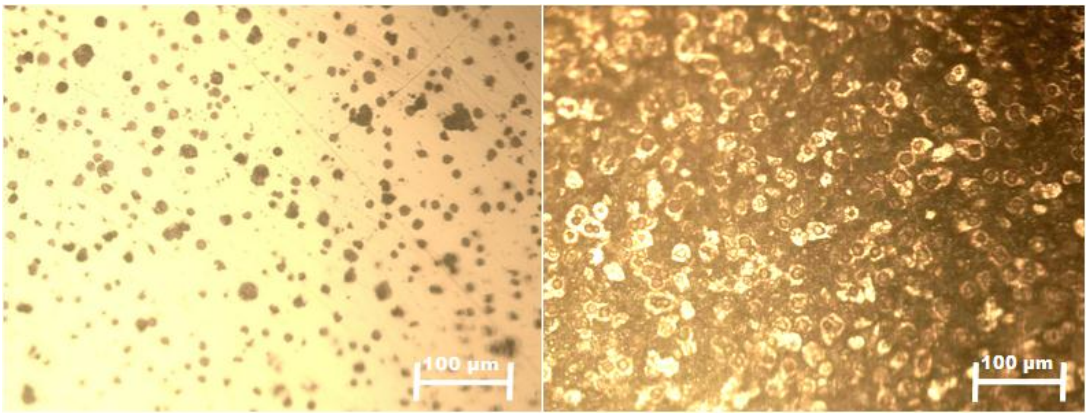


a b

Plate 13: Optical micrograph of 2mm thick section (a) unetched (b) etched of A5

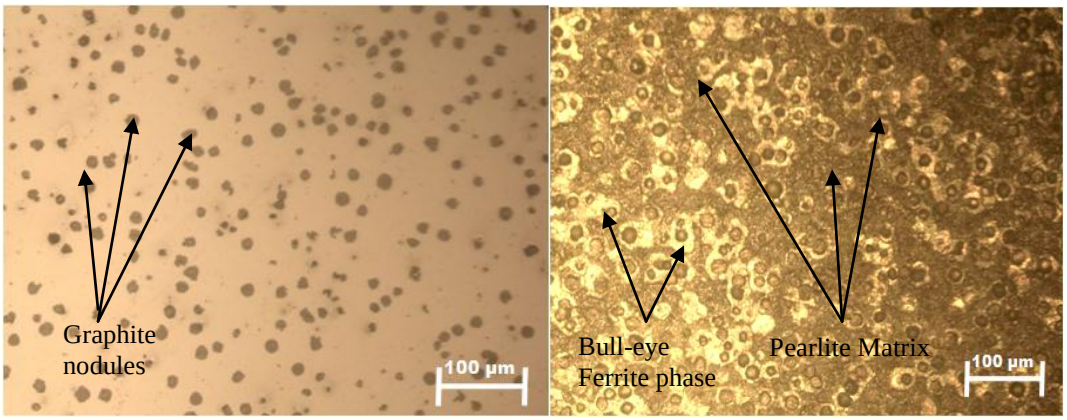


a b

Plate 14: Optical micrograph of 3mm thick section (a) unetched (b) etched of A5

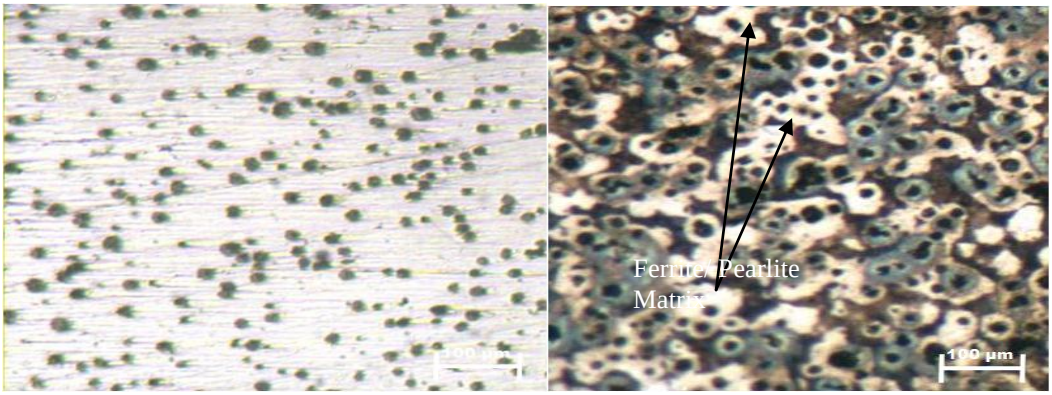


a b

Plate 15: Optical micrograph of 4mm thick section (a) unetched (b) etched of A5

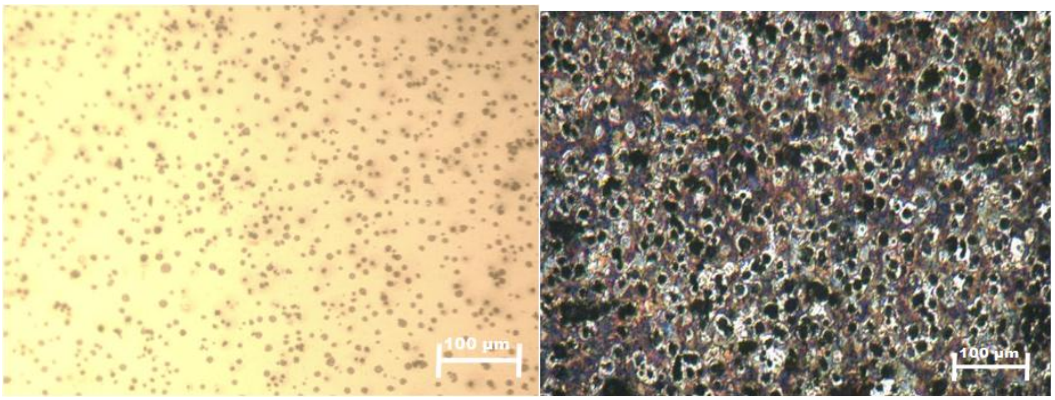


a b

Plate 16: Optical micrograph of 2mm thick section (a) unetched (b) etched of A6

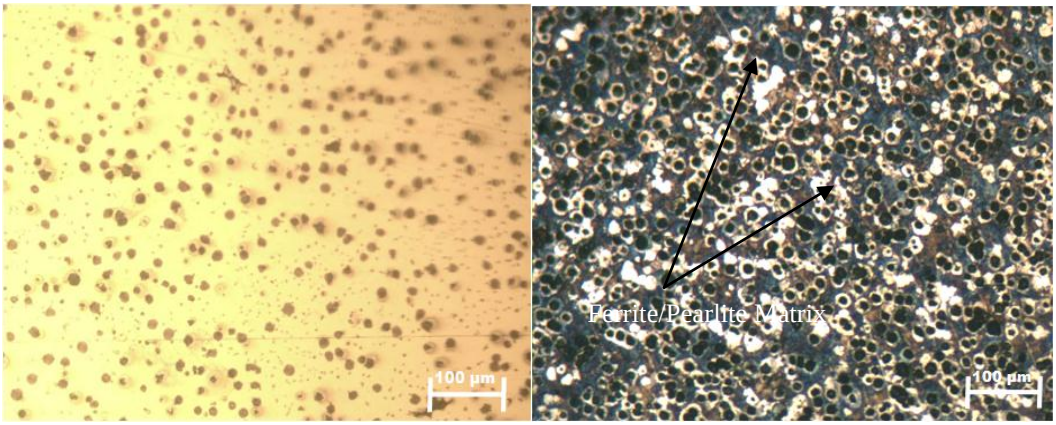


a b

Plate 17: Optical micrograph of 3mm thick section (a) unetched (b) etched of A6

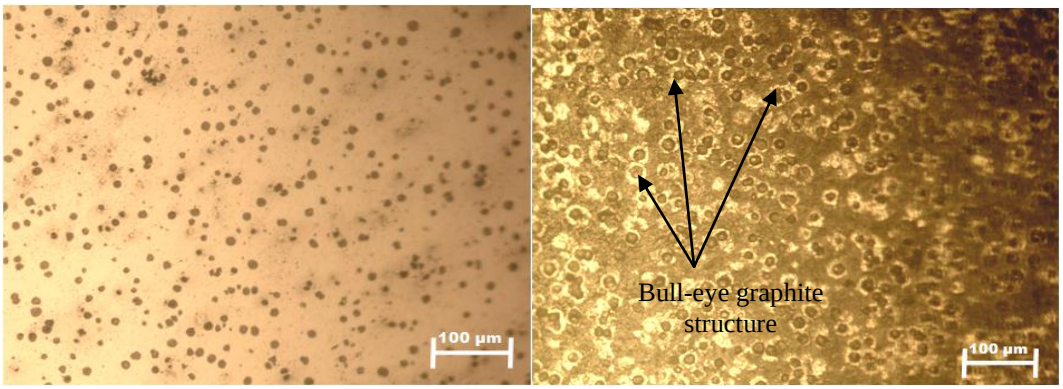


a b

Plate 18: Optical micrograph of 4mm thick section (a) unetched (b) etched of A6

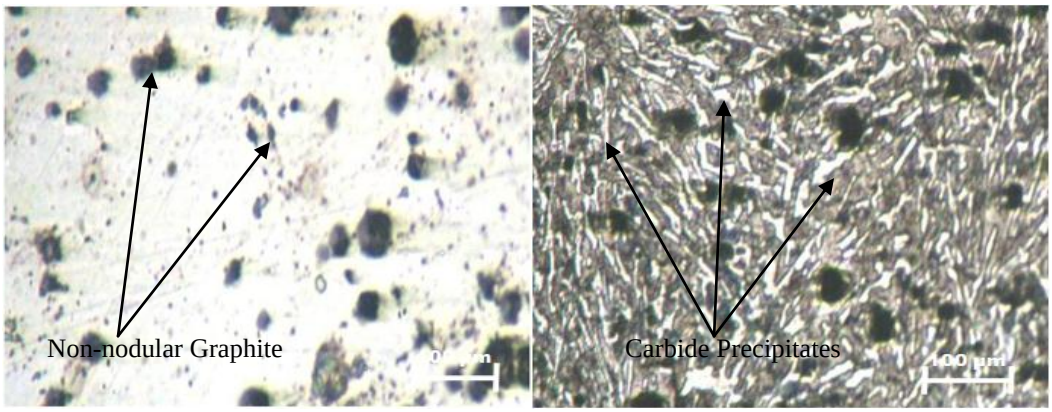


a b

Plate 19: Optical micrograph of 2mm thick section (a) unetched (b) etched of A7

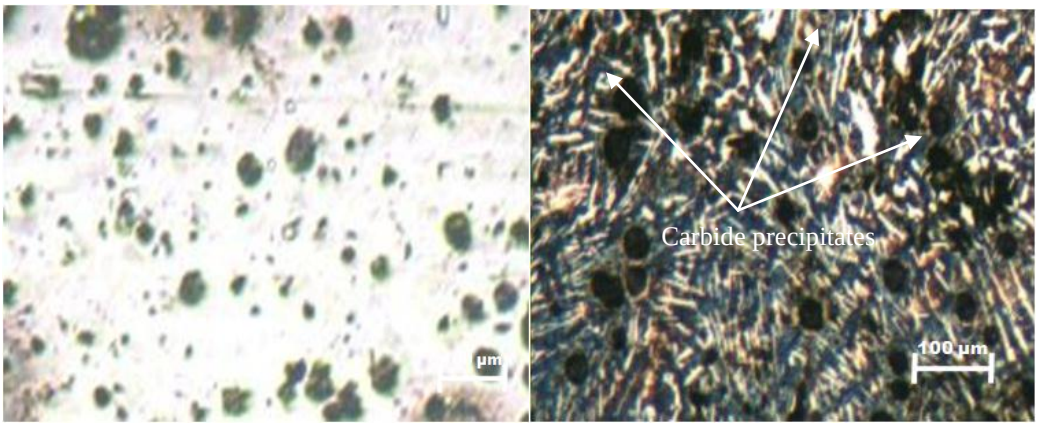


a b

Plate 20: Optical micrograph of 3mm thick section (a) unetched (b) etched of A7

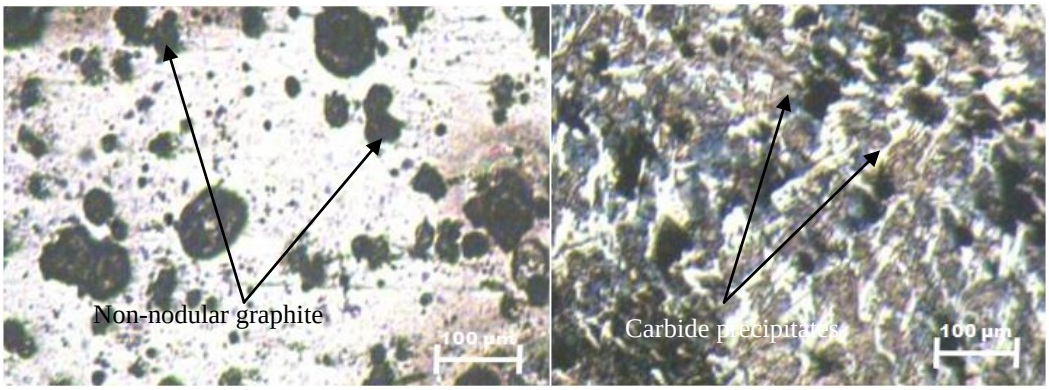


a b

Plate 21: Optical micrograph of 4mm thick section (a) unetched (b) etched of A7

### 4.3.2 Nodularity and Nodule Count

Gating sprue heights investigated influenced the solidification mechanism, mould filling, carbide and graphite morphological characteristics. Table 9 shows nodularity and nodule counts for the sprue heights investigated.

Table 9: Nodularity and nodule count results for sprue height samples

| No | Sample | Nodularity (%) | Nodule Count (nodules/mm$^2$) |
|---|---|---|---|
| 1 | A1-2 | 78.5 | 55 |
| 2 | A1-3 | 91.1 | 105 |
| 3 | A1-4 | 91.3 | 190 |
| 4 | A2-2 | 77.7 | 140 |
| 5 | A2-3 | 69.4 | 125 |
| 6 | A2-4 | 76.7 | 152 |
| 7 | A3-2 | 86.9 | 200 |
| 8 | A3-3 | 91.87 | 260 |
| 9 | A3-4 | 76.4 | 149 |
| 10 | A4-2 | 90.4 | 520 |
| 11 | A4-3 | 96.7 | 480 |
| 12 | A4-4 | 95.2 | 420 |
| 13 | A5-2 | 93.9 | 401 |
| 14 | A5-3 | 97.7 | 347 |
| 15 | A5-4 | 98.7 | 396 |
| 16 | A6-2 | 98.8 | 1364 |
| 17 | A6-3 | 96.2 | 463 |
| 18 | A6-4 | 98.9 | 546 |
| 19 | A7-2 | 41.5 | 22 |
| 20 | A7-3 | 46.0 | 64 |
| 21 | A7-4 | 33.3 | 17 |

### 4.3.3 Hardness Test

Castings made with a sprue height of 50 mm are found defective owing to incomplete filling or poor run. The hardness of the samples shows a slight upward trend as the sprue height reduces (Figure 8), except at 50 mm. The lowest values of 141, 124 and 129 BHN for 2, 3 and 4 mm thick samples respectively are obtained for 100 mm sprue height cast samples. The maximum hardness of 198, 193 and 215 BHN are obtained at 350 mm sprue height, with respect to 2, 3 and 4 mm thicknesses respectively. This corresponds to the largest volume of carbide phase as shown in Plates 1-3. Table B4 in the appendix shows the trend of BHN samples with sprue height. The low hardness of 153, 142 and 151 BHN samples cast at 50 mm sprue height is attributed to the problem of incomplete filling, which is a melt flow defect.

Regression analysis for correlation of BHN with gating sprue height shows a quadratic relationship as in Equations 8, 9 and 10 for 2, 3 and 4 mm thick samples.

$$BHN_{(2mm)} = 0.0012(S_h)^2 - 0.3252(S_h) + 165.14 \qquad R^2 = 0.9778 \qquad (8)$$

$$BHN_{(3mm)} = 0.0012(S_h)^2 - 0.311(S_h) + 151.71 \qquad R^2 = 0.95 \qquad (9)$$

$$BHN_{(4mm)} = 0.0016(S_h)^2 - 0.3757(S_h) + 157.86 \qquad R^2 = 0.9264 \qquad (10)$$

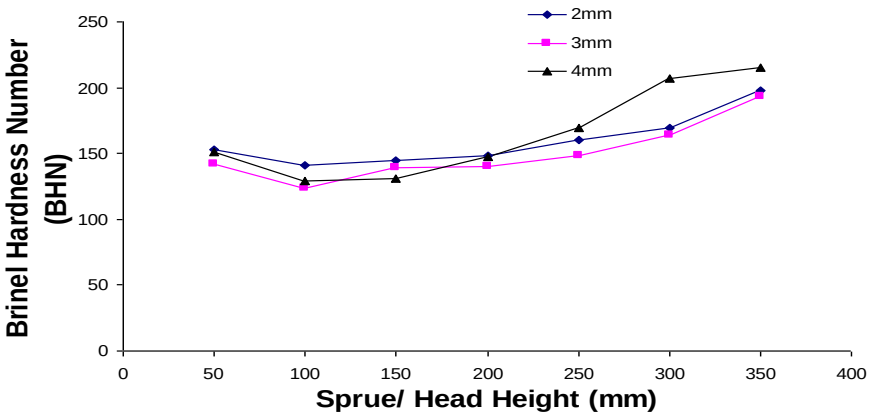


Figure 8: Variation of BHN of cast TWDI with sprue height

### 4.3.4 Tensile Test

Figures 9 and 10 are the ultimate tensile strength (UTS) and percent elongation responses of cast TWDI. Except for 50 mm cast samples both UTS and elongation decrease as the sprue height increases. This suggests that the higher metallo-static pressure imposed on the molten metal from the longer sprue height is important as the castings from the 50 mm sprue height are not properly filled. This is attributed to insufficient head pressure leading to reduction in fluidity and velocity of the melt front (Voigt, 2002). As sprue height decreases from 350-100 mm the UTS increases progressively from 101- 596 MPa, 123-578 MPa and 134-651 MPa for 2, 3, 4 mm cast thickness. The percent elongation similarly increases from 0.3-2.2, 0.2-2.3 and 0.3-4.4 for the 2, 3 and 4 mm cast thickness respectively. This suggests two problems; the first is the existence of turbulent flow and air entrapment associated with higher head pressure and secondly, solidification defects caused by heat transfer phenomena during its flow through the longer distance (larger sprue height) in the gating channel (Masoumi *et al.*, 2005; Pavlak, 2008). These cause defects, which are responsible for reduction in the mechanical properties of the TWDI castings as observed. Thus, it is recommended that sprue height should be kept as short as possible, but not too short to allow for proper mould filling in the production of TWDI castings. Tables B5 and B6, in the appendix, show these trends.

The regression curve used to correlate UTS and percent elongation with gating sprue height follows Equations 11-13 and Equations 14-16 respectively for 2, 3 and 4 mm thick samples.

$$UTS\ (_{2mm}) = 0.0015(S_h)^2 - 2.7469(S_h) + 867.69 \qquad R^2 = 0.9823 \qquad (11)$$

$$UTS\ (_{3mm}) = -0.0005(S_h)^2 - 1.7229(S_h) + 761.29 \qquad R^2 = 0.9800 \qquad (12)$$

$$UTS\ (_{4mm}) = 0.0011(S_h)^2 - 2.7939(S_h) + 955.5 \qquad R^2 = 0.968 \qquad (13)$$

$$\%\ _{Elong.}\ (_{2mm}) = 3 \times 10^{-5}(S_h)^2 - 0.021\ (S_h) + 4.2229 \qquad R^2 = 0.9385 \qquad (14)$$

$$\%\ _{Elong.}\ (_{3mm}) = 4 \times 10^{-6}(S_h)^2 - 0.0114\ (S_h) + 3.5571 \qquad R^2 = 0.9508 \qquad (15)$$

$$\%\ _{Elong.}\ (_{4mm}) = 9 \times 10^{-5}(S_h)^2 - 0.0534\ (S_h) + 8.5943 \qquad R^2 = 0.9530 \qquad (16)$$

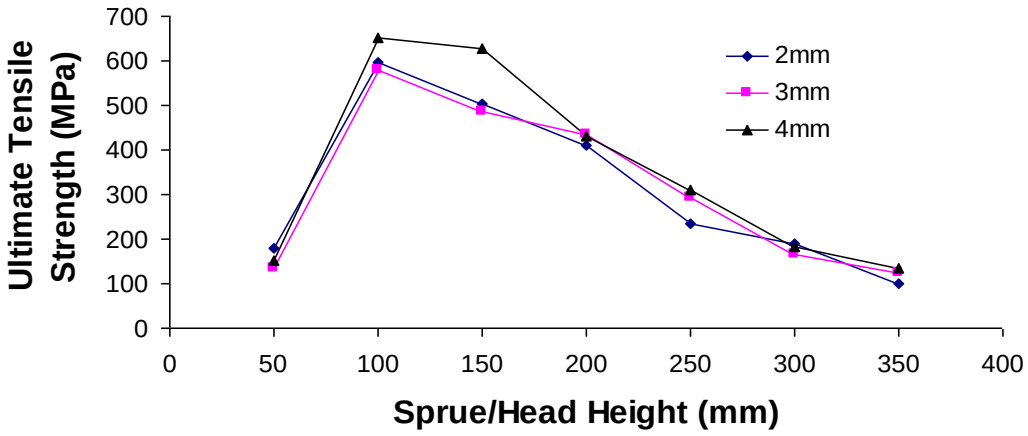


Figure 9: Variation of ultimate tensile strengths of cast TWDI with sprue height.

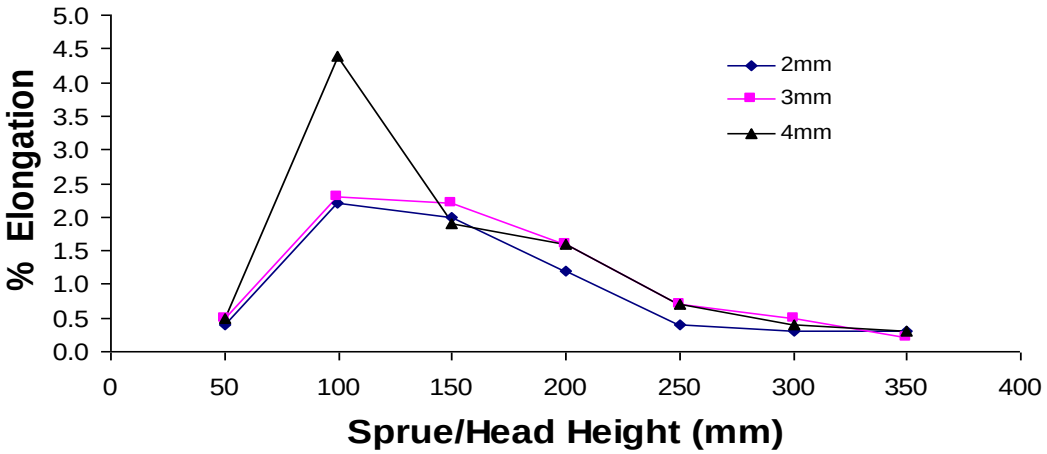


Figure 10: Variation of percent elongation of cast TWDI with sprue height

### 4.4 Effect of nodularisation treatment temperature

Nodularisation treatment is carried out in a preheated treatment ladle immediately after tapping from furnace. Industry standard treatment temperatures of 1430-1550$^0$C are investigated. The sandwich method is employed for the treatment using ferro-silicon magnesium ferro-alloy. Proper treatment reduces under-cooling and prevents chill (carbide) formation (Skaland, 2005). The treatment occurs spontaneously with so

much agitation in molten metal. This agitation can reduce residual magnesium available in melt for formation of potent nuclei for graphite nodule segregation. This study showed that the treatment temperature significantly influenced percent elongation.

### 4.4.1 Microstructural Analysis (Nodularisation treatment temperature)

The microstructures of samples TI (2, 3, 4 mm) is shown in Plates 22-24. The 2 mm thick sample treated at $1550^0$C show good nodularity (93%) but poor nodule count (184 nodules/$mm^2$). Carbide precipitation is observed in etched sample. Existence of irregularly-shaped (non-nodular) graphite structures and massive carbide precipitation is observed in the 3 and 4 mm thick samples resulting in poor nodularity of 71% and 67% respectively. Nodule count values are also low in these samples. This shows that treating at $1550^0$C is not favourable for attaining desired nodularity and nodule count in the samples. The T2 range ($1530^0$C) also showed the same structure. T2 (2mm section sample) in Plate 25 revealed poor nodule count and nodularity of 57% and 192 nodules/$mm^2$ respectively (Table 10) and also existence of shrinkage porosity in its structure. This is due to insufficient nuclei for the precipitation of graphite nodule. The carbide phase in the T3 range (Plates 28-30) reduced compared to the T1 and T2 samples. In T3 (2 mm) the presence of non-nodular graphite and carbide precipitates are observed. The T3 (3 mm) shows large proportion of irregular shaped graphite structures. Improved nodularity and nodule count with reduction of the carbide phase are observed for T4-T6 samples (Plates 31-39 and Table 10). The best morphologies are achieved for the T5 ($1470^0$C) and T6 ($1450^0$C) samples, where good nodularity of Type I and Size 5, 6 and 7 (ASTM A247) with high nodule count and absence of carbide precipitates are observed in their pearlite-ferrite matrix. The best nodularity and nodule count values of 98%, 95%, 97% and 610, 512, 458 nodules/ $mm^2$ for 2, 3 and 4 mm thick samples respectively correspond to treatment temperature of $1450^0$C. At $1430^0$C, the treatment temperature < $1450^0$C, the shape of graphite structure greatly deteriorated to irregular/non-nodular graphite structures (Plates 40-42). Structures of this type are not desirable as these lower both UTS and percent elongation and affect performance (Hassan *et al.*, 2010; Sangame and Shinde, 2013).

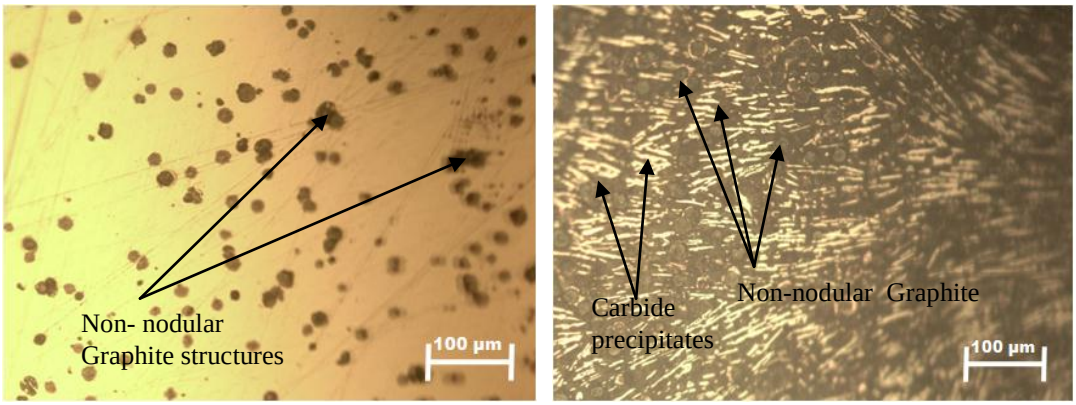


a b

Plate 22: Optical micrograph of 2mm thick section (a) unetched (b) etched of T1

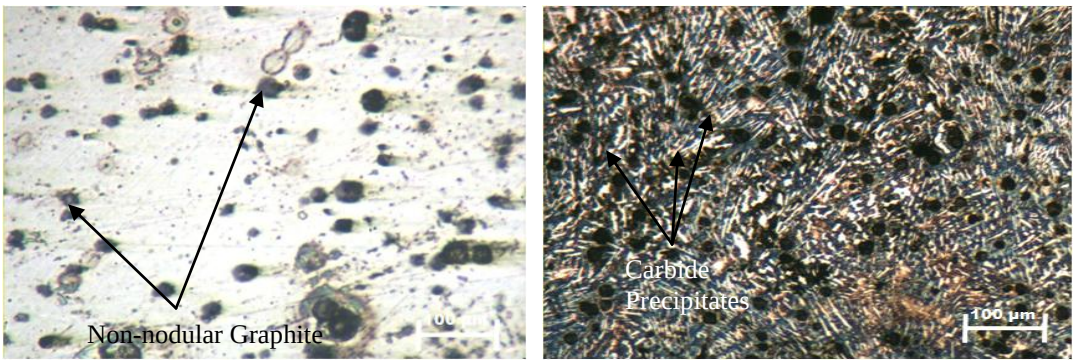


a b

Plate 23: Optical micrograph of 3mm thick section (a) unetched (b) etched of T1

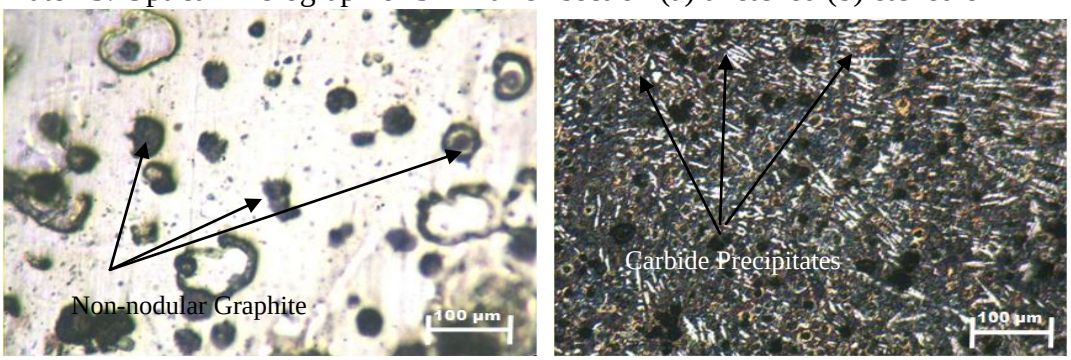


a b

Plate 24: Optical micrograph of 4mm thick section (a) unetched (b) etched of T1

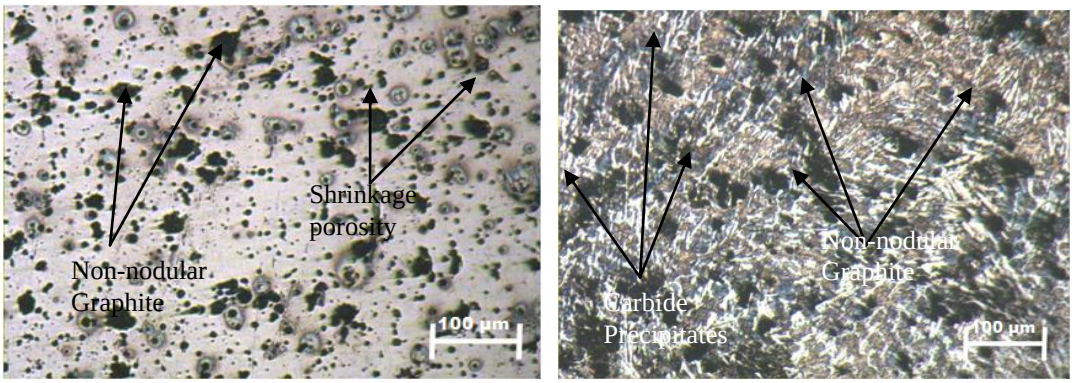


a b

Plate 25: Optical micrograph of 2mm thick section (a) unetched (b) etched of T2

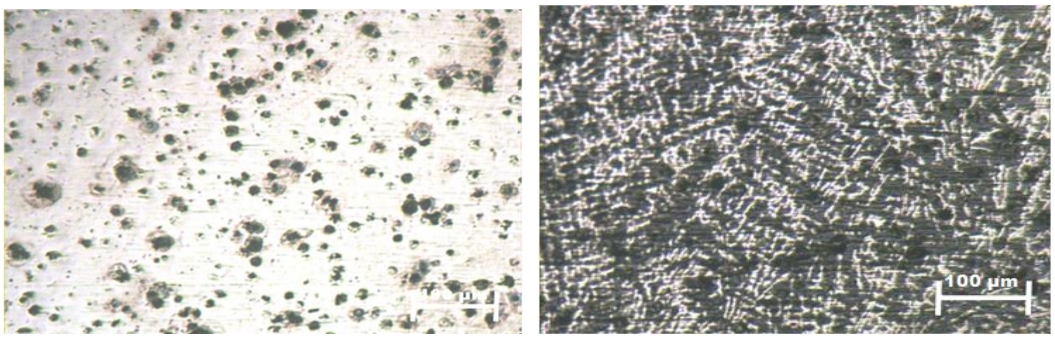


a b

Plate 26: Optical micrograph of 3mm thick section (a) unetched (b) etched of T2

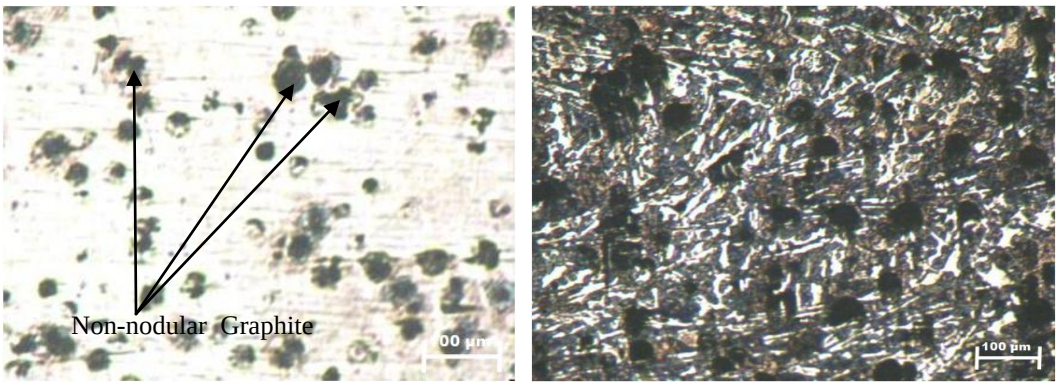


a b

Plate 27: Optical micrograph of 4mm thick section (a) unetched (b) etched of T2

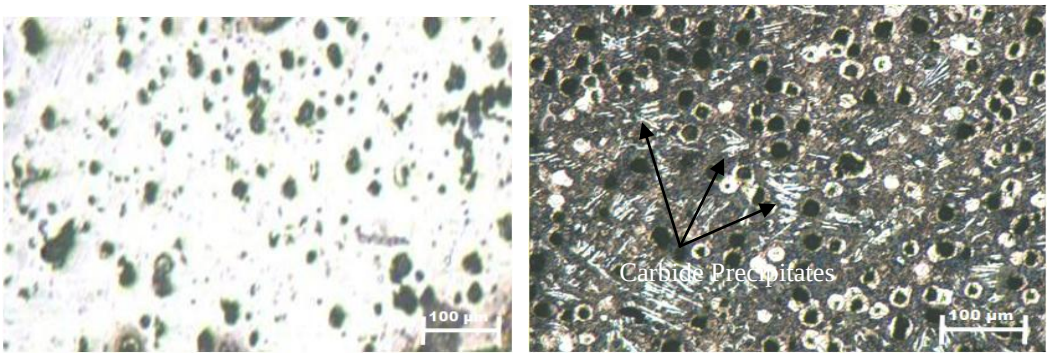


a b

Plate 28: Optical micrograph of 2mm thick section (a) unetched (b) etched of T3

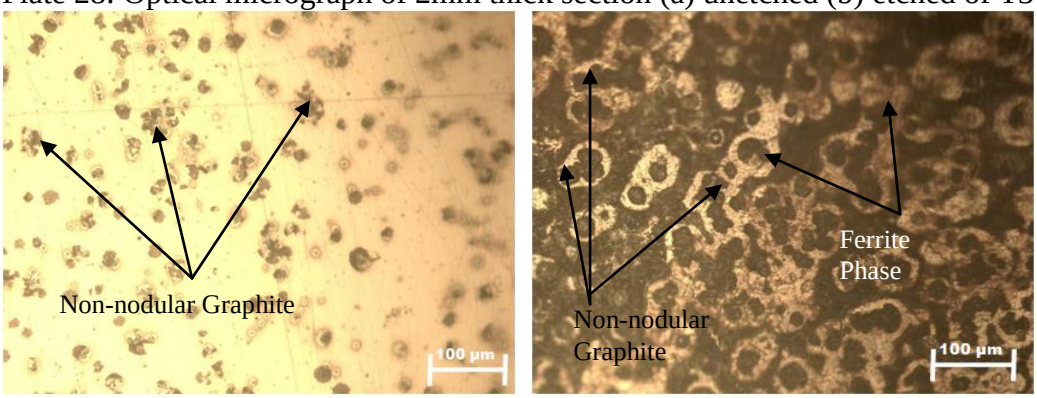


a b

Plate 29: Optical micrograph of 3mm thick section (a) unetched (b) etched of T3

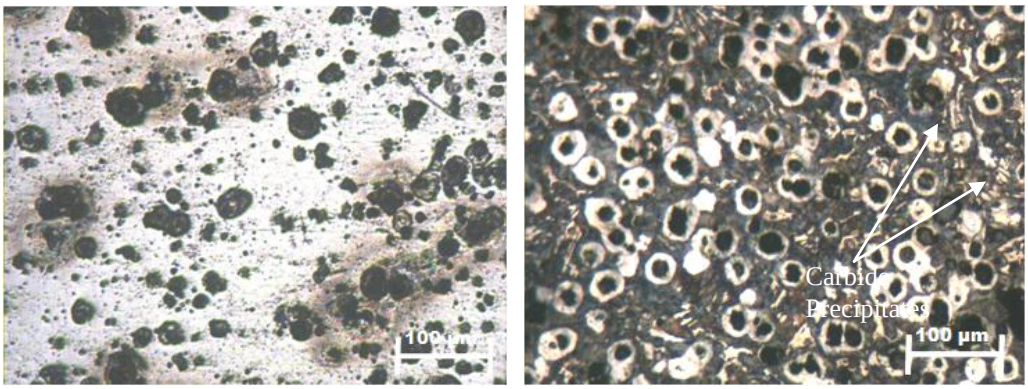


a b

Plate 30: Optical micrograph of 4mm thick section (a) unetched (b) etched of T3

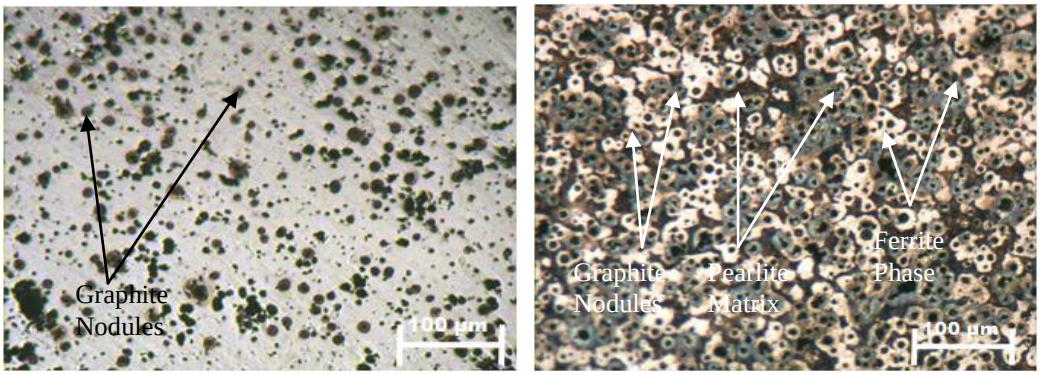


a b

Plate 31: Optical micrograph of 2mm thick section (a) unetched (b) etched of T4

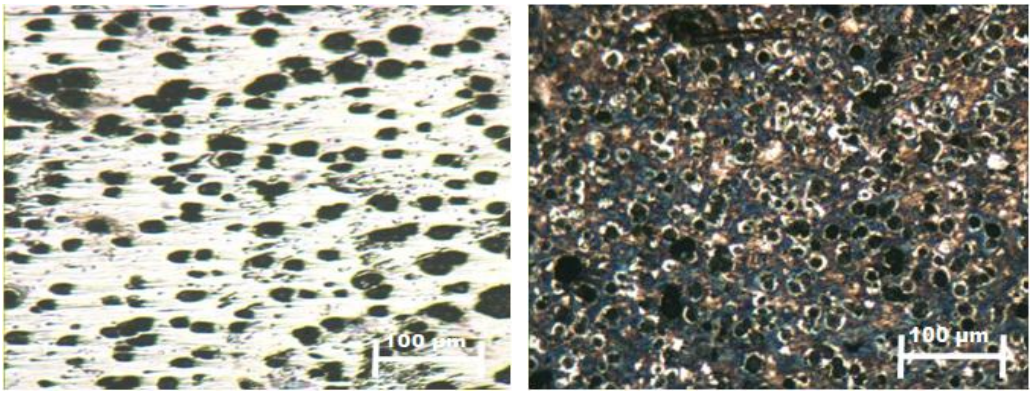


a b

Plate 32: Optical micrograph of 3mm thick section (a) unetched (b) etched of T4

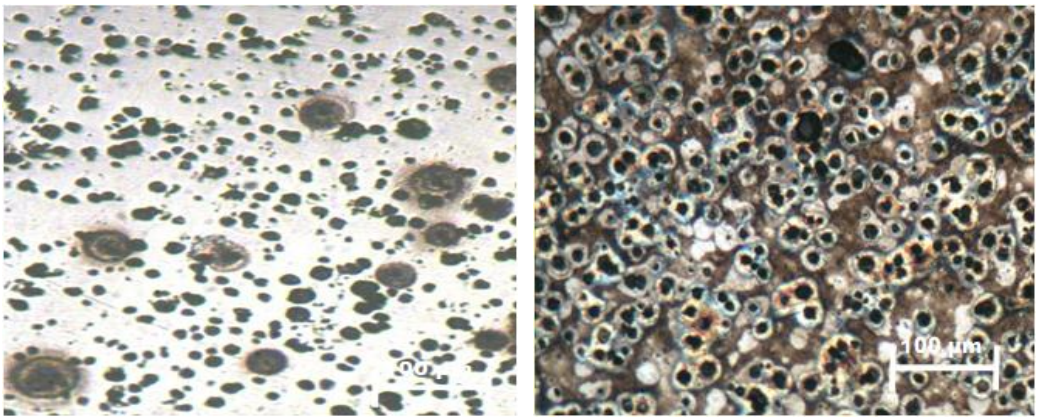


a b

Plate 33: Optical micrograph of 4mm thick section (a) unetched (b) etched of T4

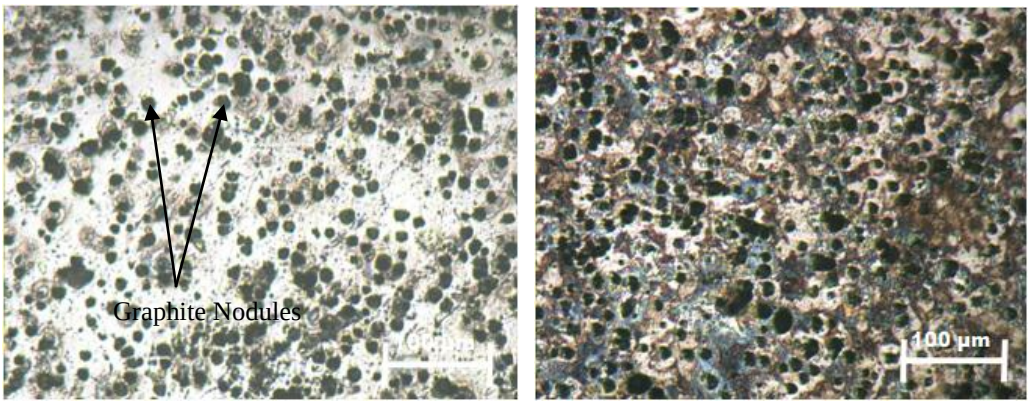


a b

Plate 34: Optical micrograph of 2mm thick section (a) unetched (b) etched of T5

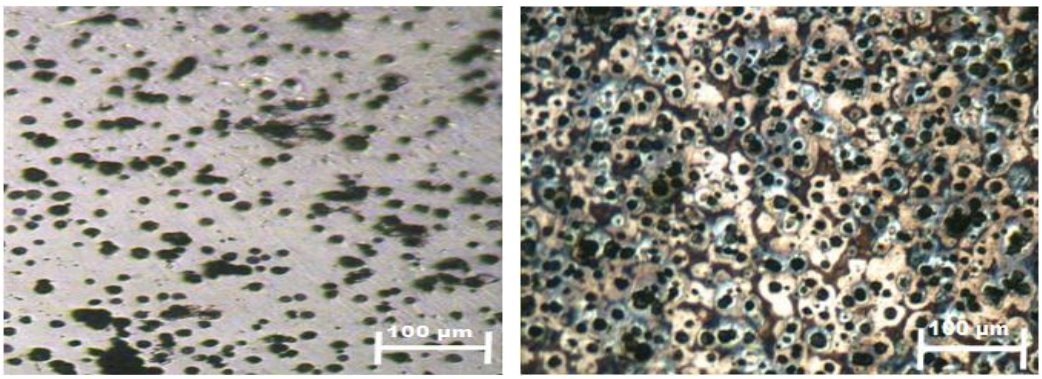


a b

Plate 35: Optical micrograph of 3mm thick section (a) unetched (b) etched of T5

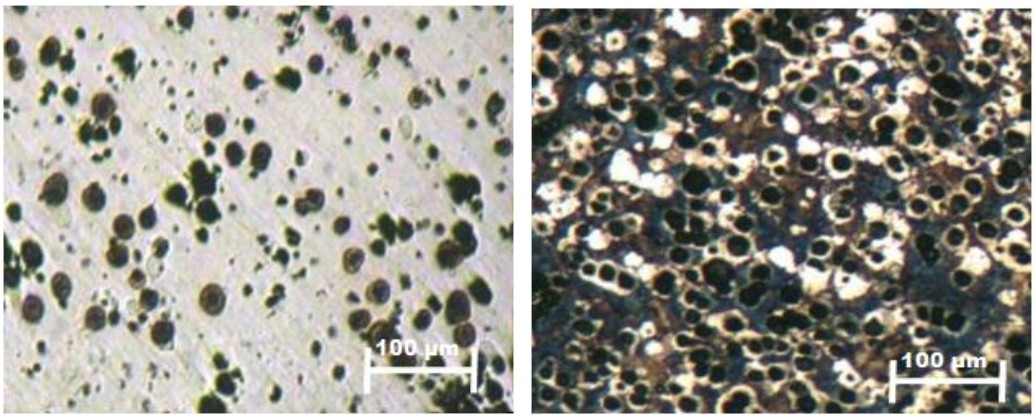


a b

Plate 36: Optical micrograph of 4mm thick section (a) unetched (b) etched of T5

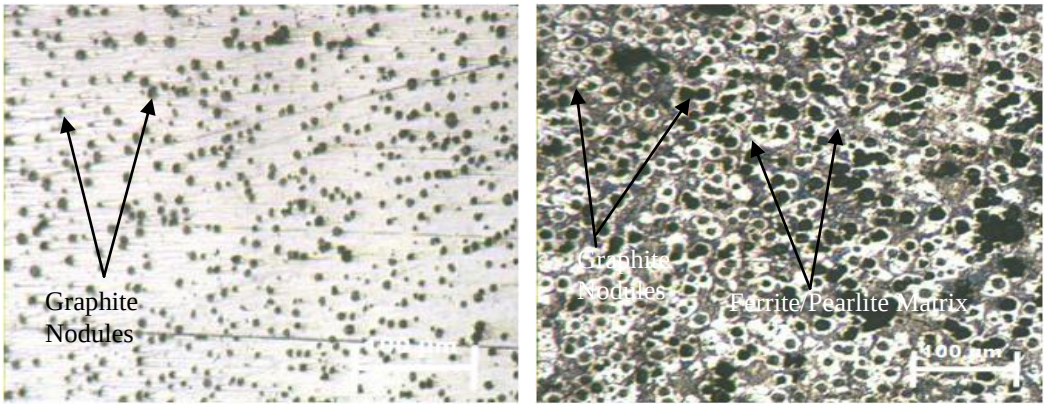


a b

Plate 37: Optical micrograph of 2mm thick section (a) unetched (b) etched of T6

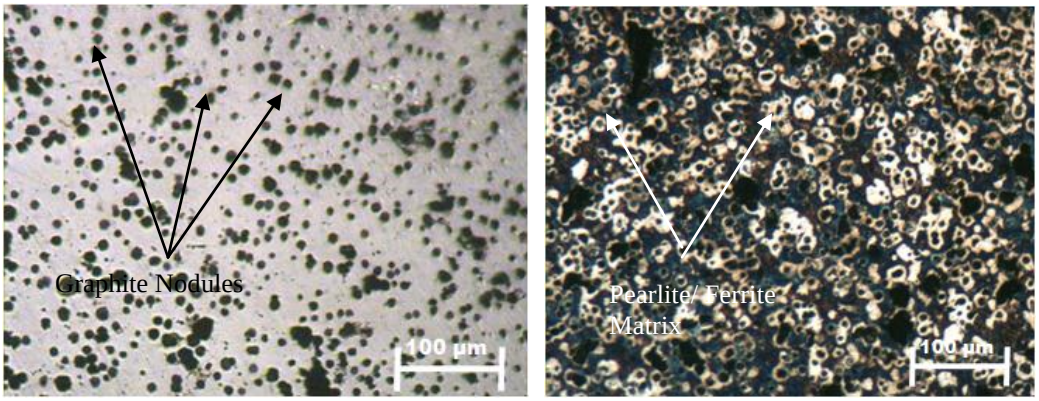


a b

Plate 38: Optical micrograph of 3mm thick section (a) unetched (b) etched of T6

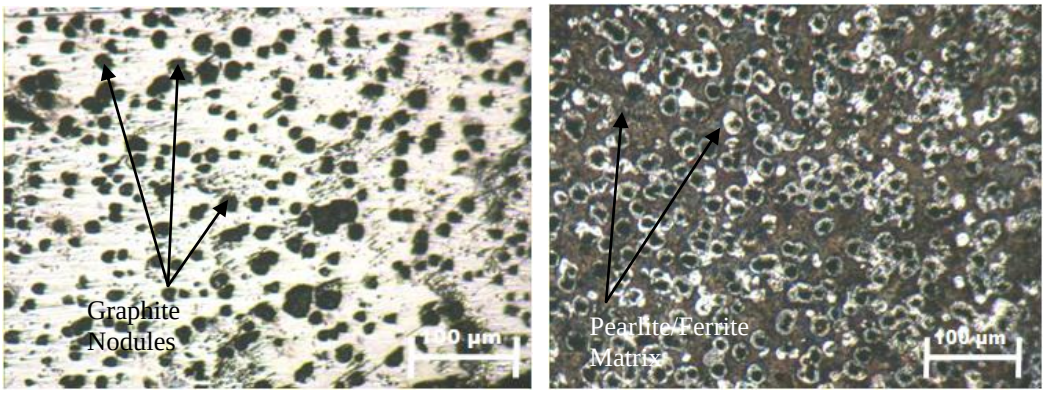


a b

Plate 39: Optical micrograph of 4mm thick section (a) unetched (b) etched of T6

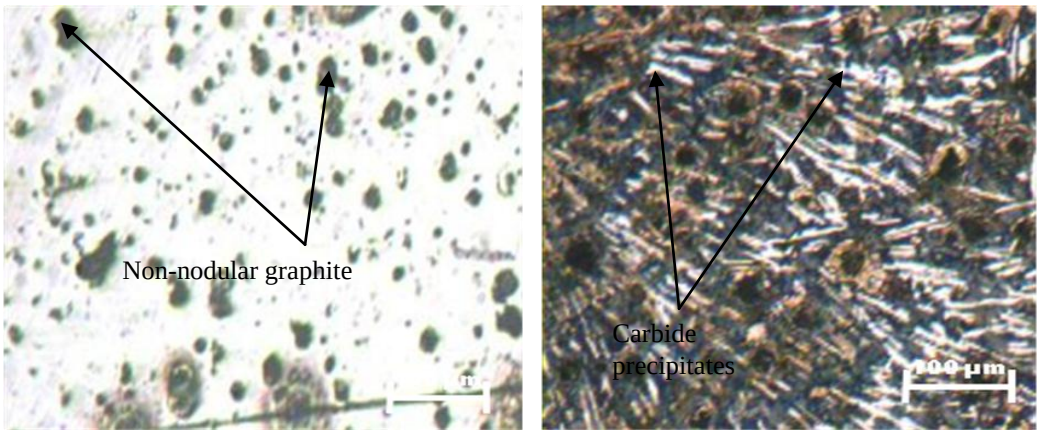


a b

Plate 40: Optical micrograph of 2mm thick section (a) unetched (b) etched of T7

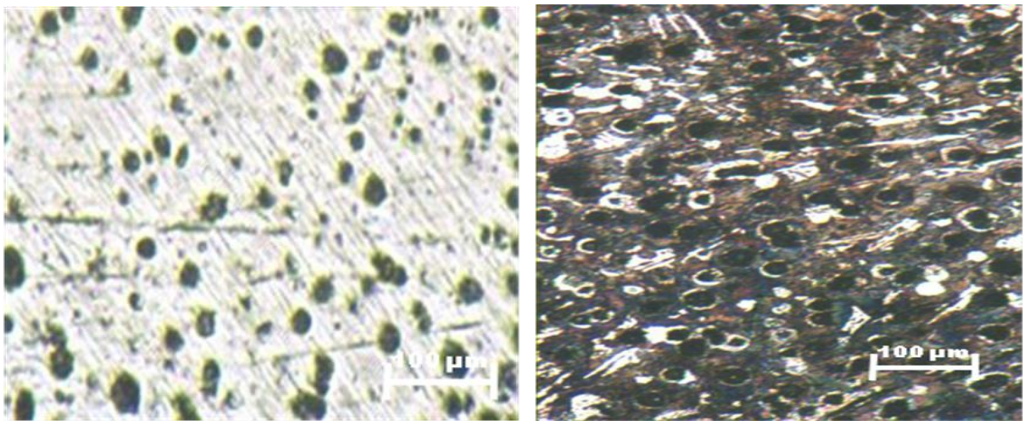


a b

Plate 41: Optical micrograph of 3mm thick section (a) unetched (b) etched of T7

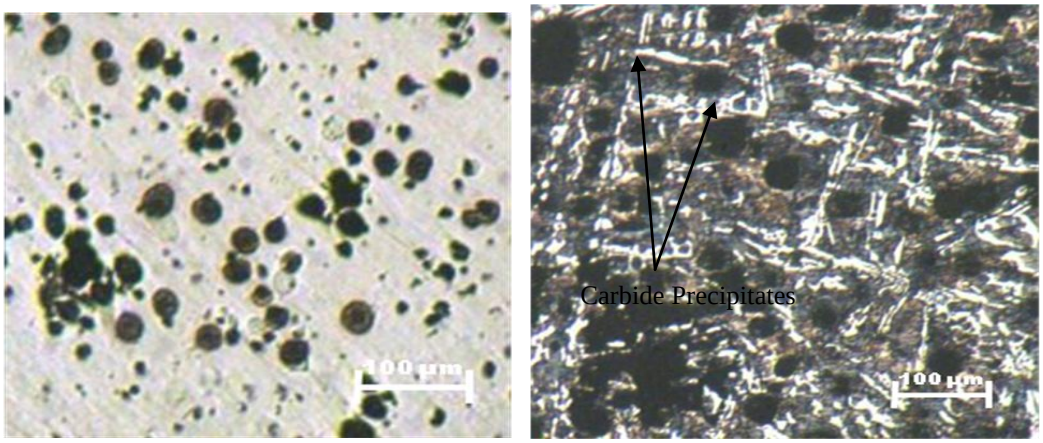


a b

Plate 42: Optical micrograph of 4mm thick section (a) unetched (b) etched of T7

### 4.4.2 Nodularity and Nodule Count

Treatment temperatures investigated in the study influenced magnesium recovery and the yields of reaction. Table 10 shows nodularity and nodule counts for temperatures investigated.

Table 10: Nodularity and nodule count results for treatment temperature samples

| No | Sample | Nodularity (%) | Nodule Count (nodules/mm$^2$) |
|---|---|---|---|
| 1 | T1-2 | 93 | 184 |
| 2 | T1-3 | 71 | 121 |
| 3 | T1-4 | 67 | 65 |
| 4 | T2-2 | 57 | 192 |
| 5 | T2-3 | 72 | 387 |
| 6 | T2-4 | 53 | 57 |
| 7 | T3-2 | 72 | 180 |
| 8 | T3-3 | 67 | 113 |
| 9 | T3-4 | 80 | 276 |
| 10 | T4-2 | 94 | 416 |
| 11 | T4-3 | 85 | 311 |
| 12 | T4-4 | 92 | 484 |
| 13 | T5-2 | 93 | 543 |
| 14 | T5-3 | 92 | 521 |
| 15 | T5-4 | 96 | 271 |
| 16 | T6-2 | 98 | 610 |
| 17 | T6-3 | 95 | 512 |
| 18 | T6-4 | 97 | 458 |
| 19 | T7-2 | 68 | 97 |
| 20 | T7-3 | 83 | 77 |
| 21 | T7-4 | 80 | 59 |

### 4.4.3 Hardness Test

The variation of BHN with treatment temperatures TWDI samples is shown in Figure 11. The Figure initially shows a sinusoidal relationship, which tends almost constant. The peak value of 172 BHN occurred at 1450$^0$C for 4 mm thick sample. The pattern observed in hardness curve for 2, 3 and 4 mm thick samples are similar and this suggests that sample thickness had little or no influence on hardness value. The curves show that treatment temperature has no significant effect on BHN values for these three thicknesses.

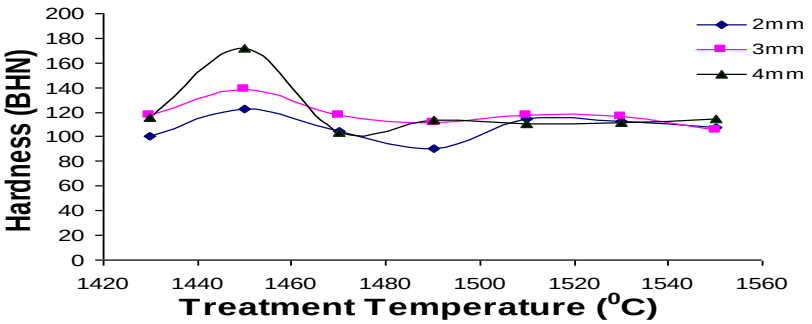


Figure 11: Variation of BHN of TWDI with Treatment Temperature.

### 4.4.4 Tensile Test

The ultimate tensile stress (UTS) and percent elongation responses with treatment temperature are shown in Figures 12 and 13 respectively. In Figure 12, the sinusoidal UTS pattern with peak UTS of 389, 409 and 514 MPa for 2, 3 and 4mm thicknesses respectively at 1450$^0$C are achieved. This sinusoidal relationship for the three thicknesses does not established any relationship between UTS and treatment temperature i.e., treatment temperature has negligible effect on UTS. However, at 1450$^0$C, high nodule count and nodularity ratings observed for all thicknesses investigated (Table 10) are attributed to good graphite shape characteristics as this parameter impact positively on ductility (Hassan *et al.*, 2010; Sangame and Shinde, 2013; Mullins, 2006). This indicates that lower treatment temperature of 1450$^0$C is important to achieve the desired UTS for the nodularization treatment reaction, while temperature of 1430$^0$C lowers the UTS. The result indicates that treatment temperature of 1430$^0$C is inadequate in providing sufficient nuclei for graphite precipitation (Skaland, 2005).

Regression analysis revealed that percent elongation (Figure 13) has a downward exponential relationship with treatment temperature as in Equations 17, 18 and 19 for 2, 3 and 4 mm respectively.

$$\%\ \text{Elong.}\ (_{2mm}) = 10^{8} e^{-0.0123 T_t} \qquad (R^2 = 0.9845) \qquad (17)$$

$$\%\ \text{Elong.}\ (_{3mm}) = 8 \times 10^{7} e^{-0.0119 T_t} \qquad (R^2 = 0.9669) \qquad (18)$$

$$\%\ \text{Elong.}\ (_{4mm}) = 2 \times 10^{8} e^{-0.0124 T_t} \qquad (R^2 = 0.9855) \qquad (19)$$

At treatment temperature of $1550^0$C the percent elongations of 0.7, 0.8 and 0.8 for 2, 3 and 4 mm thicknesses respectively are realized. Treatment temperature of $1450^0$C improved percent elongation significantly to 2.6, 2.9 and 3.0 for 2, 3 and 4 mm plates respectively. These decreased again at $1430^0$C with cast samples showing poorly formed nodules (low nodularity and nodule count). This indicates that from $1450^0$C - $1550^0$C, lower treatment temperature favours better nucleation of graphite structures, better nodule count and nodularity. At treatment temperature of $1430^0$C lower than $1450^0$C the percent elongation is greatly impaired. These three parameters (nodularity, nodule count and percent elongation) have direct bearing on ductility. The best ductility of 2.6, 2.9 and 3.0 is achieved at $1450^0$C for all the three thicknesses investigated. However, these elongations are lower than that prescribed for ASTM Spec. No A536-80 (80-50-06) for automotive application (6%).

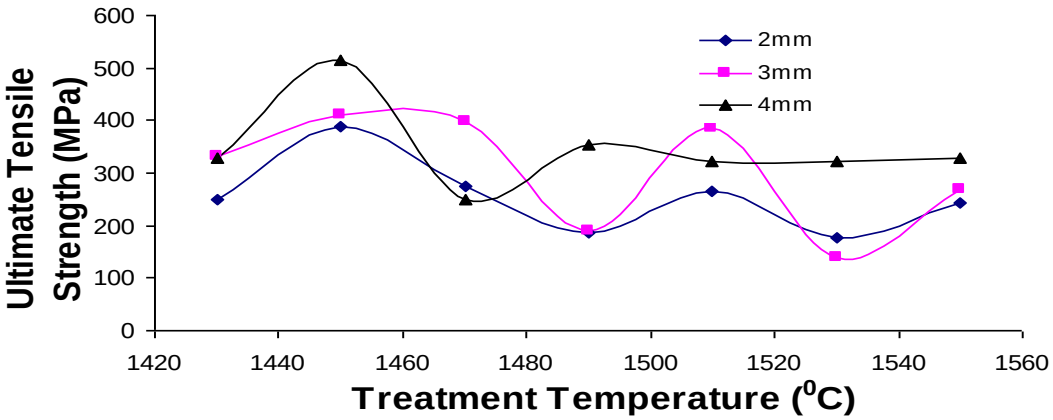


Figure 12: Variation of UTS of TWDI castings with Treatment temperature

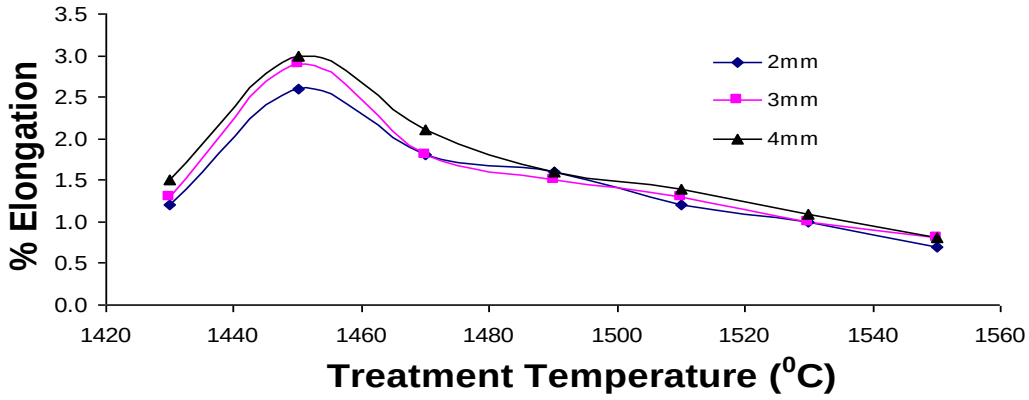


Figure 13: Variation of % elongation of TWDI castings with Treatment temperature

## 4.5 THERMAL PROPERTIES OF MOULDING SAND MIXES

### 4.6 Effect of Aluminium Dross (AlDr) Moulding Sand Additive

The effects of AlDr addition on moulding sand properties for all the sand mixes are shown in Figures 14-18. These display the variation of green shear strength, permeability, percent compactibility, moisture content and shatter index with wt. % AlDr respectively. The addition of the AlDr slightly reduced the green sand strength but not to the extent as to impair its ability to produce adequate strength in the moulds. Permeability increased slightly but later remained almost constant as wt. % AlDr is increased. Percent compactibilty reduced as additive content increases, while moisture content increased from 4.0-4.2 % as AlDr increased from 6- 8 wt.%. The shatter index property was adversely impaired at 12 wt. % AlDr.

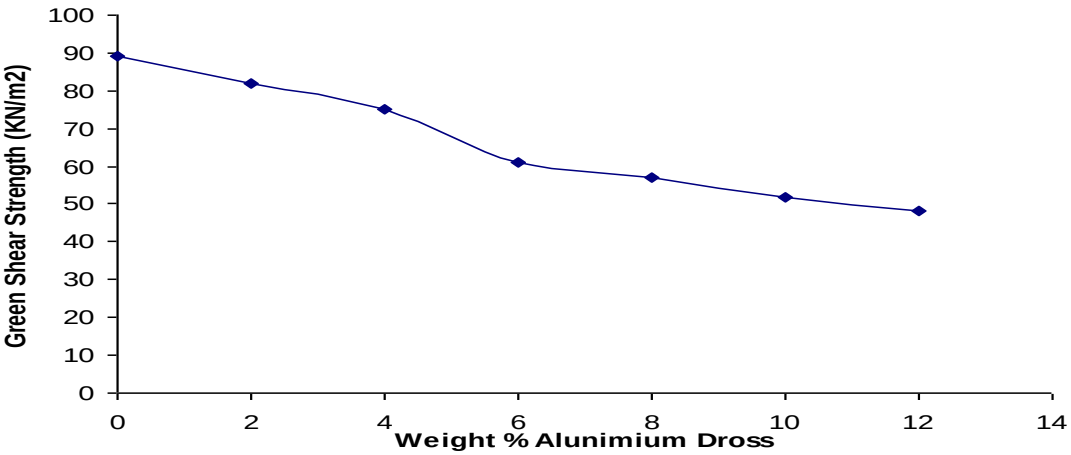


Figure 14: Variation of green shear strength with weight % AlDr in sand-AlDr mix.

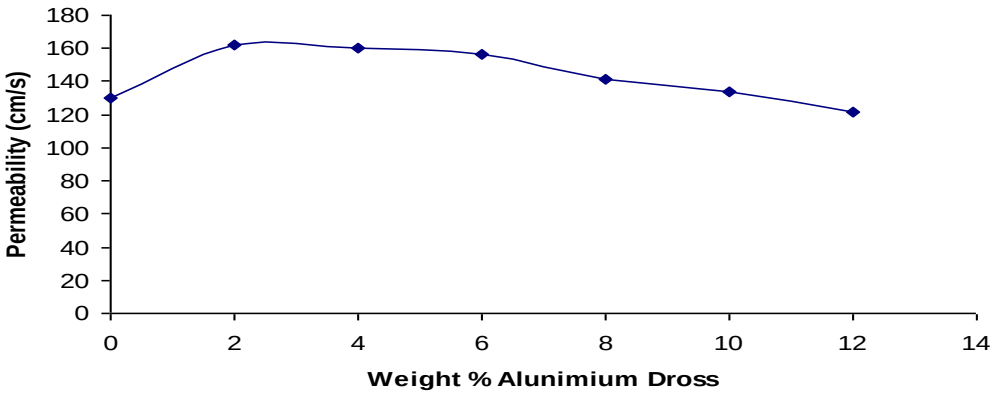


Figure 15: Variation of permeability with weight % AlDr in sand-AlDr mix

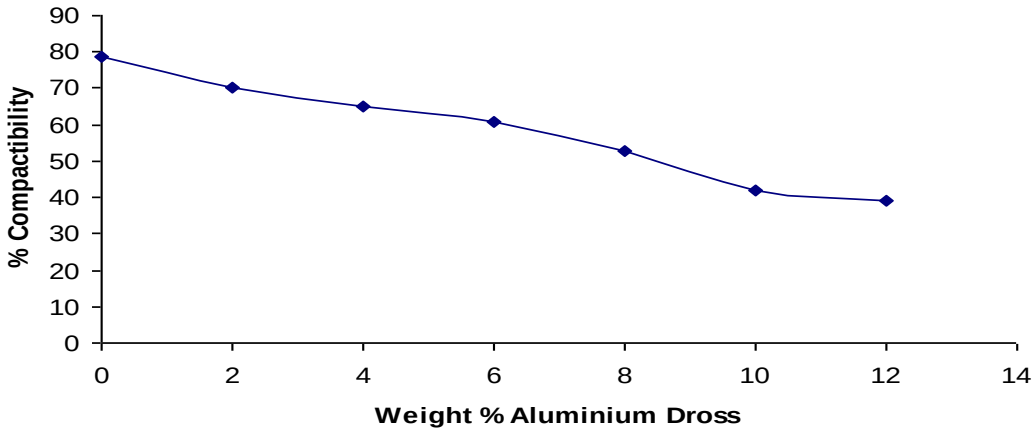


Figure 16: Variation of Percent compactibility with weight % AlDr in sand-AlDr mix

.

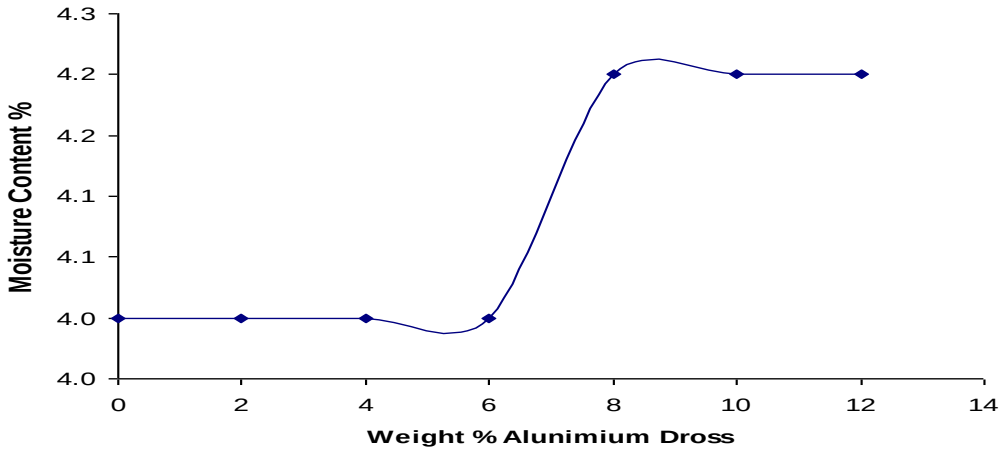


Figure 17: Variation of moisture content with weight % AlDr in sand-AlDr mix

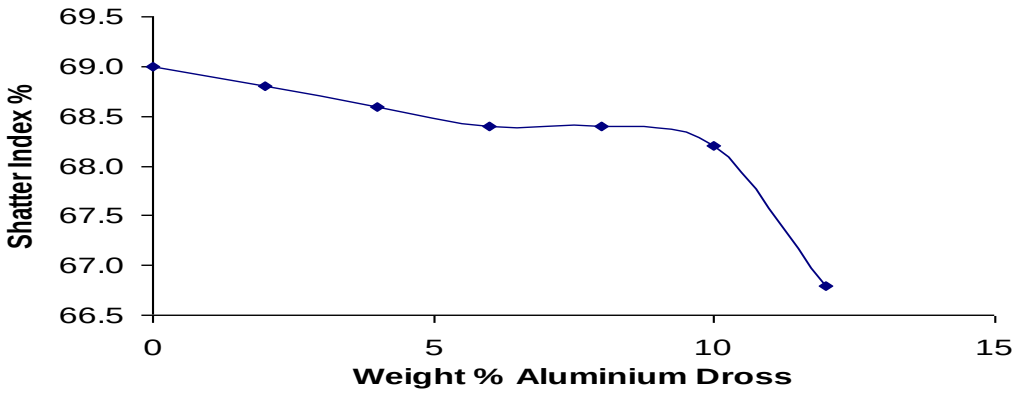


Figure 18: Variation of percent shatter index with weight % AlDr in sand-AlDr mix

The effects of AlDr addition on thermal properties of sand mixes are displayed in Figures 19 for thermal conductivity. The thermal conductivity of the sand mix shown in Figure 19 increased significantly from that of the control mix up to 6 wt. % AlDr, after which it dropped progressively with further increase in weight percent of AlDr from 8-12wt. %. This indicates faster cooling/heat transfer rate for the TWDI samples up to 6 wt. % AlDr. This faster cooling rate implies insufficient time for graphite segregation i.e., formation of graphite nodules. It then reduced on further AlDr addition to sand mix, thereby aiding thermal insulation, which is desired here. The reduction in thermal conductivity at 6 wt. % AlDr implies that some level of thermal insulation was achieved. This can be attributed to the larger proportion of alumina and silica in the sand mix at 6-12 wt. % AlDr addition. This allowed more time for graphite segregation. But it should be noted that these values of 1.787, 1.753 and 1.718 W/m.K for 6, 8 and 10 wt. % respectively (except that of 12 wt. % AlDr of 1.540 W/m.K) are still lower than that of the control sand mix of 1.631 W/m.K. This implies that solidification of samples is delayed when cast in these moulding sand/ AlDr sand mix. This is expected to aid proper graphite segregation in melt, thereby enhancing better nodularity and nodule count.

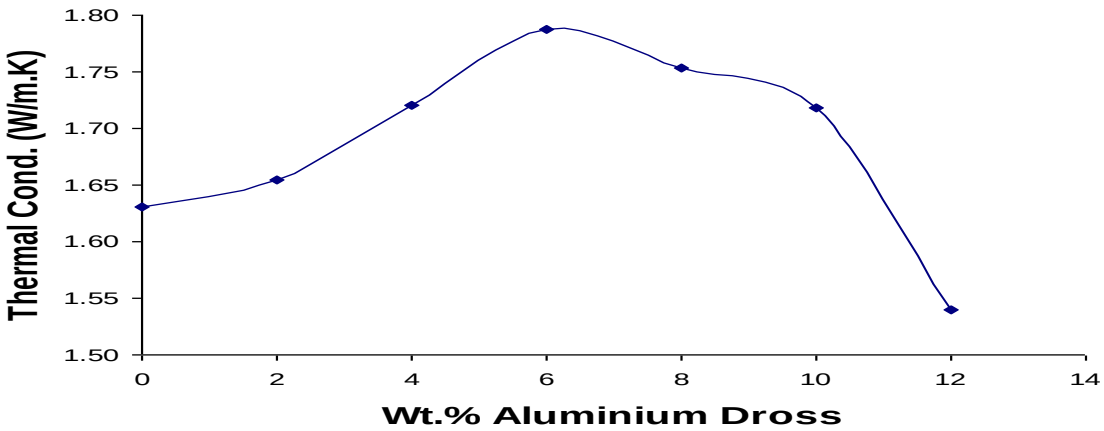


Figure 19: Thermal conductivity with weight % AlDr in sand-AlDr mix

### 4.6.1 Microstructural Analysis of Sand – Aluminium Dross Cast Samples

The micrographs of the samples cast using AlDr additive show that this additive did not favour the formation of desired microstructure in TWDI (Plates 46-63). The control samples show good nodularity, good nodule count and control of carbide precipitates. Non-nodular graphite and poor matrix structure are observed in the samples cast using AlDr /moulding sand mix. Plates 43-45 show micrographs of control samples cast without AlDr blend. The samples show good nodularity and nodule count in contrast to those cast in AlDr/ sand mix. Matrix constituents are mainly ferrite and pearlite exhibiting the bull-eyed structure.

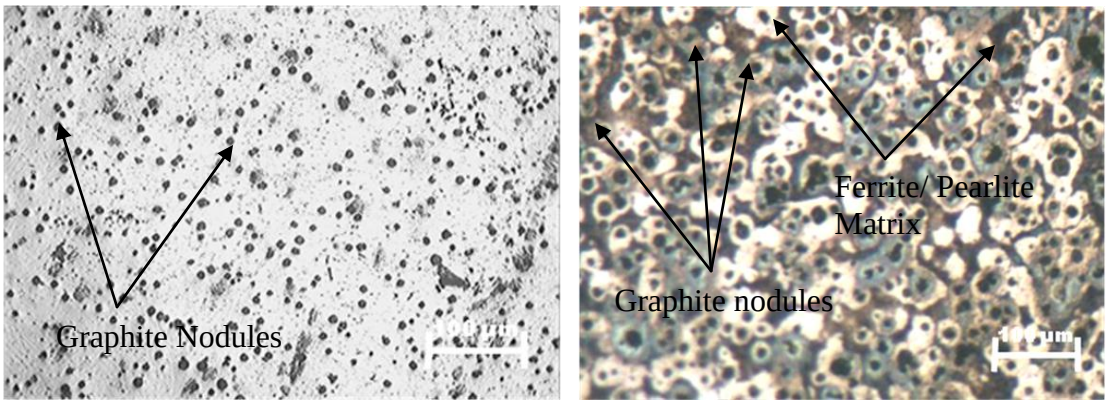


a b

Plate 43: Optical micrograph of 2mm thick section (a) unetched (b) etched of D

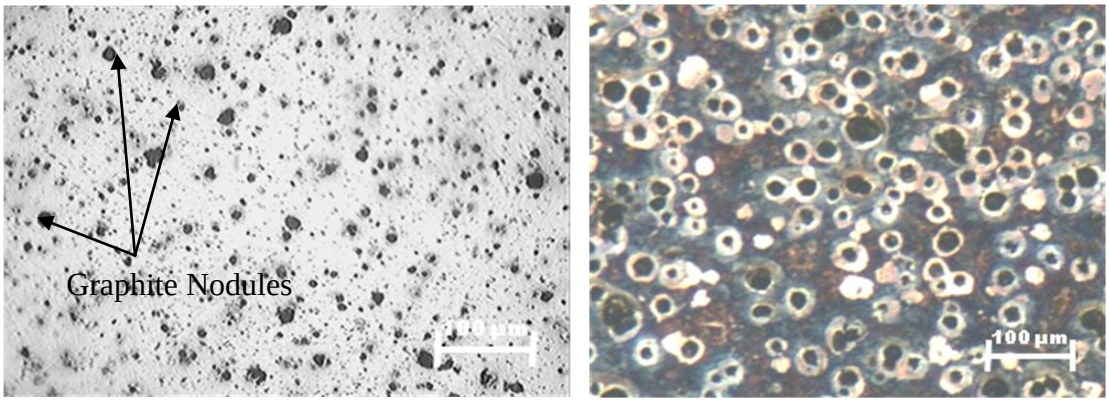


a b

Plate 44: Optical micrograph of 3mm thick section (a) unetched (b) etched of D

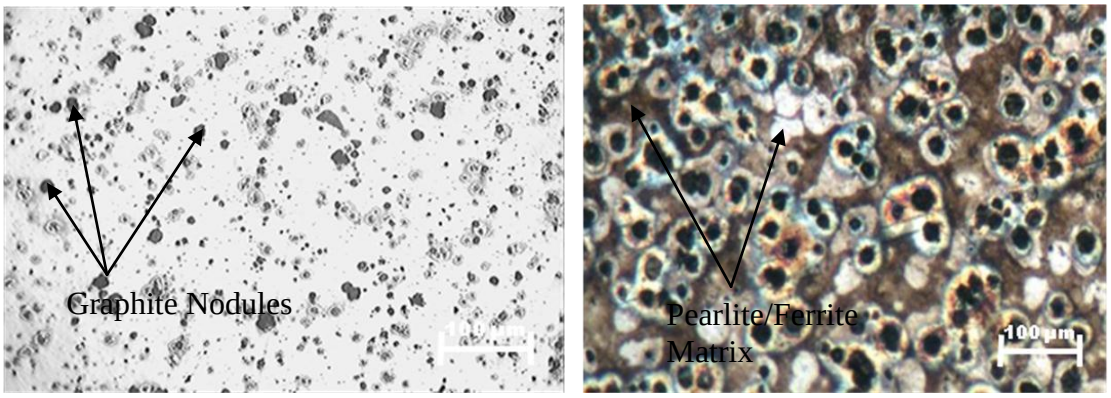


a b

Plate 45: Optical micrograph of 4mm thick section (a) unetched (b) etched of D

Microstructures of samples cast using 2wt. % AlDr show poorly formed graphite nodules for all thicknesses. In addition to non- nodular graphite, there is the presence of a dark phase which is suspected to be a reaction product formed from reactions between elements in the melt with aluminium, alumina or sulphur (from sulphate) in the moulding sand mix (Table A2). Thermal conductivity increased slightly from 1.631 to 1.654 W/m K with reduction in the time for nucleation of graphite nodules (Plates 46-48). Due to the reduction in solidification time, insufficient time is available for graphite nucleation leading to carbide precipitation in TWDI matrix.

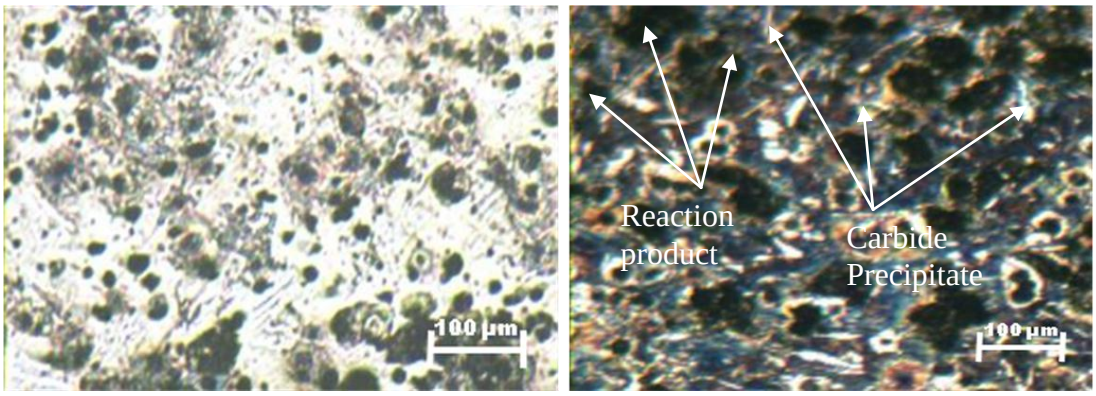


a b

Plates 46: Optical micrograph of 2mm thick section (a) unetched (b) etched of D1

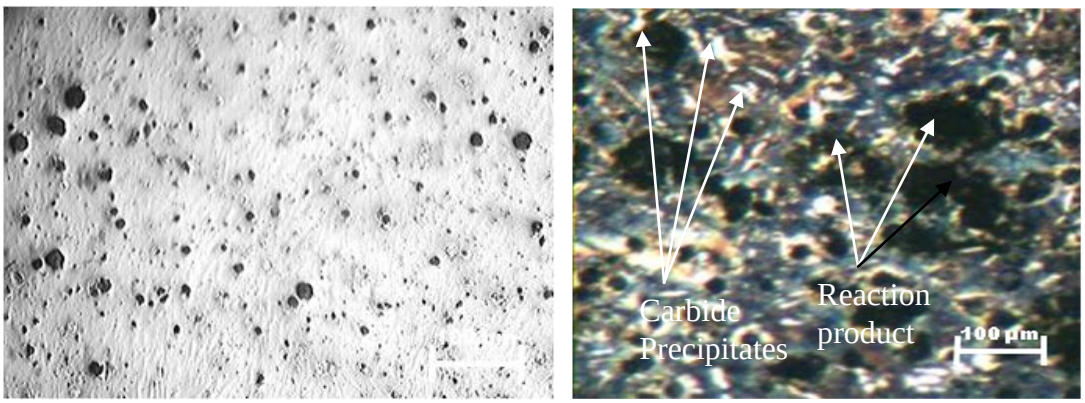


a b

Plate 47: Optical micrograph of 3mm thick section (a) unetched (b) etched of D1

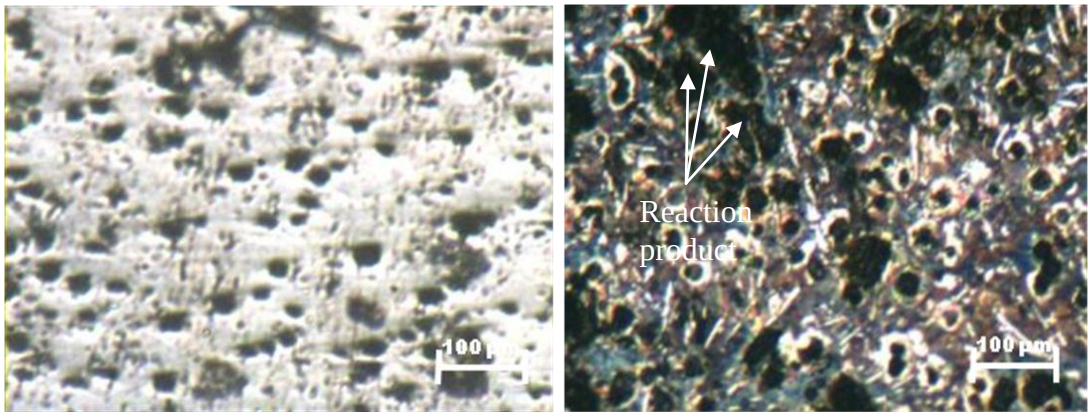


a b

Plates 48: Optical micrograph of 4mm thick section (a) unetched (b) etched of D1

Figures 49-51 for 4 wt. % AlDr show these dark reaction product phases, poor nodularity and nodule count with carbide precipitates in structure.

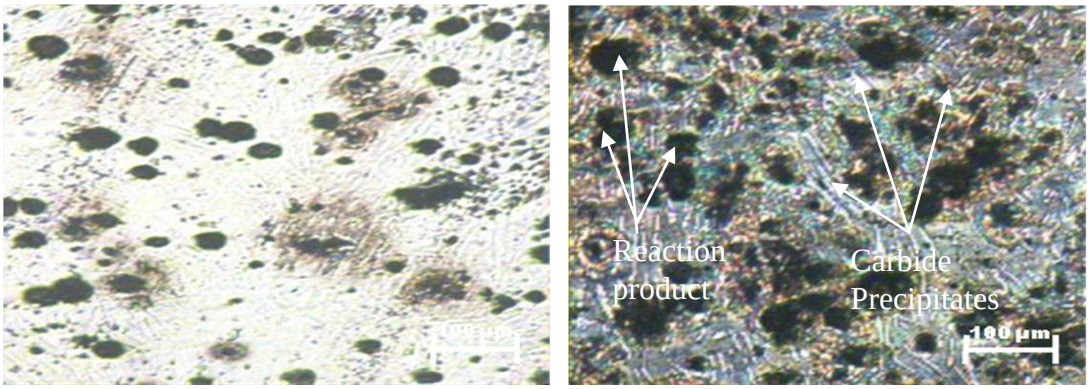


a b

Plate 49: Optical micrograph of 2mm thick section (a) unetched (b) etched of D2

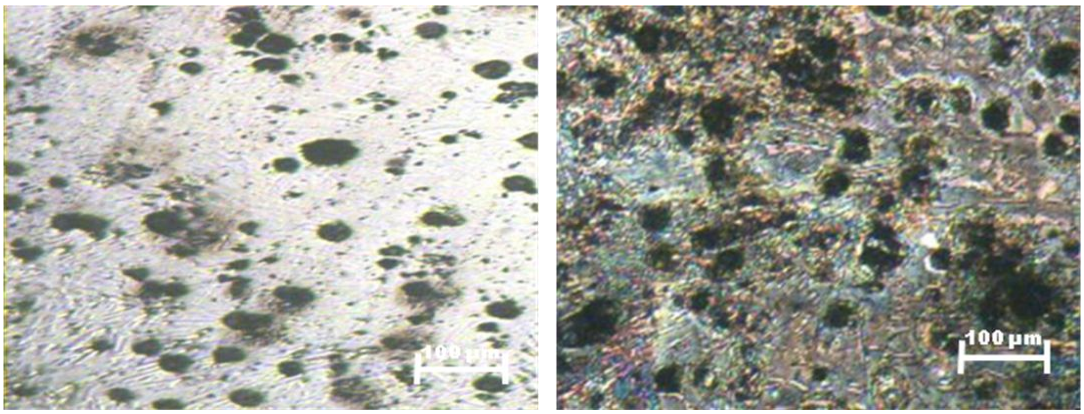


a b

Plate 50: Optical micrograph of 3mm thick section (a) unetched (b) etched of D2

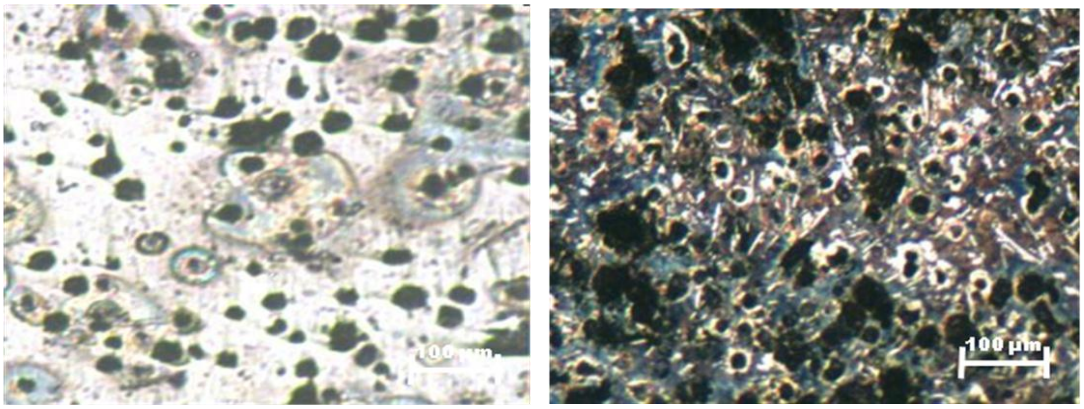


a b

Plate 51: Optical micrograph of 4mm thick section (a) unetched (b) etched of D2

Figures 52-54 show samples cast at 6 wt% AlDr. This corresponds to the highest thermal conductivity value of 1.787 W/m K indicating high heat transfer rate. The samples exhibit poor nodularity and nodule count as previously observed, reaction product patches are evident and matrix structure is not clearly defined.

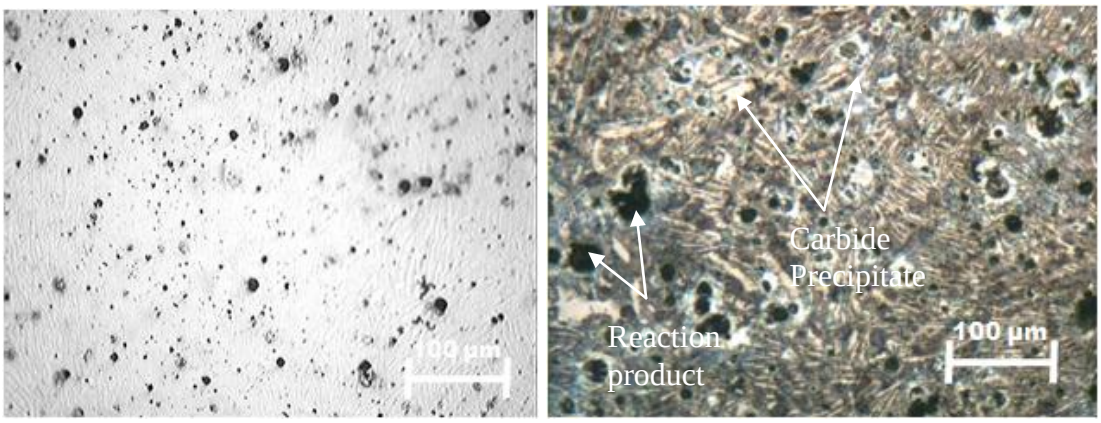


a b

Plate 52: Optical micrograph of 2mm thick section (a) unetched (b) etched of D3

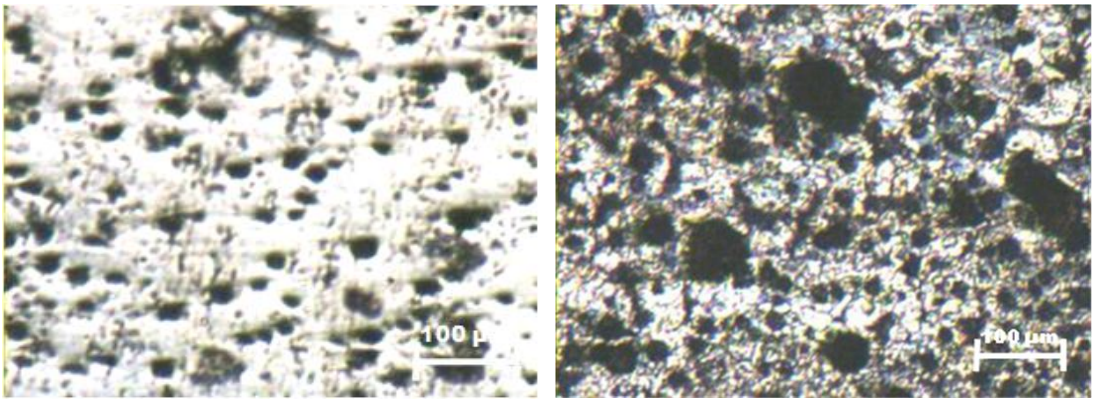

a b

Plate 53: Optical micrograph of 3mm thick section (a) unetched (b) etched of D3

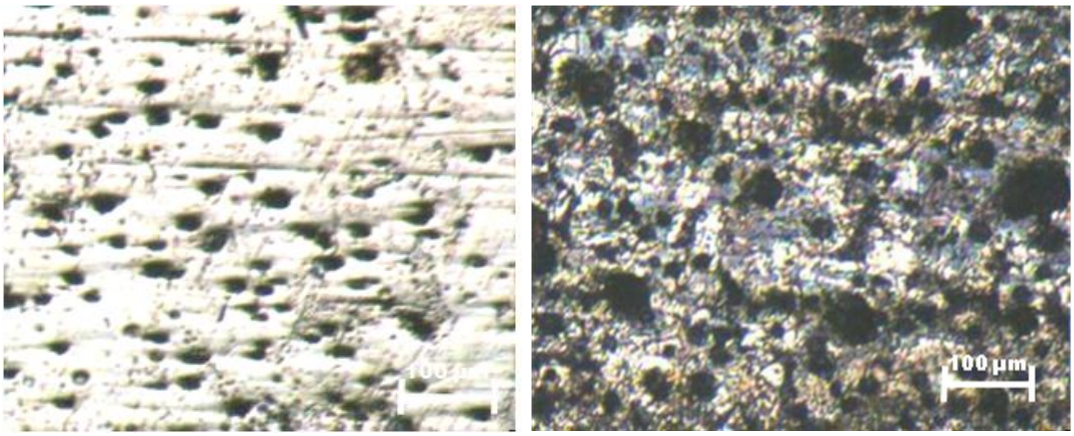


a b

Plate 54: Optical micrograph of 4mm thick section (a) unetched (b) etched of D3

In Figures 55-57 at 8 wt. % AlDr, the samples structures show the presence of ferrite phase. Thermal conductivity dropped to 1.753 W/m K, though it is still higher than that of the control sand mix.

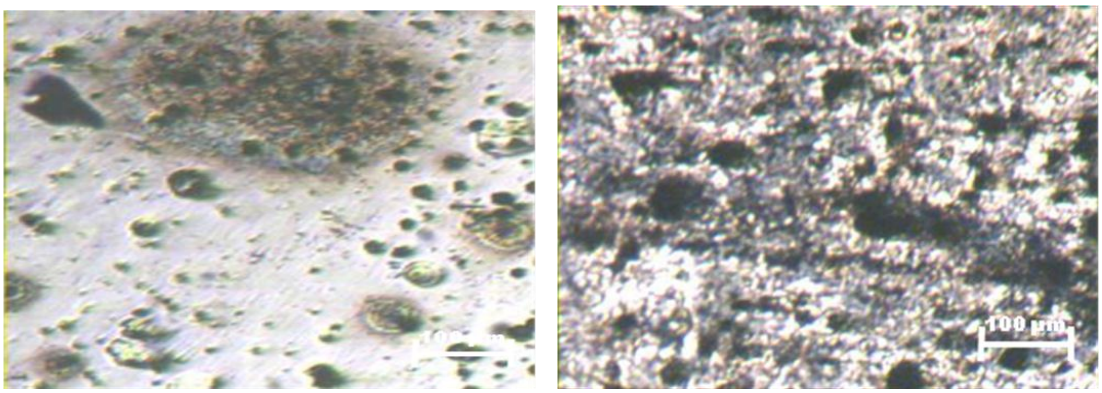


a b

Plate 55: Optical micrograph of 2mm thick section (a) unetched (b) etched of D4

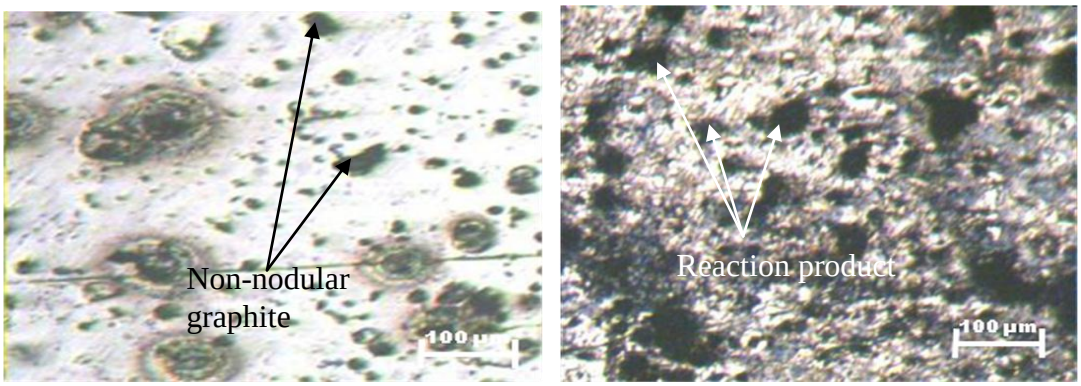


a b

Plate 56: Optical micrograph of 3mm thick section (a) unetched (b) etched of D4

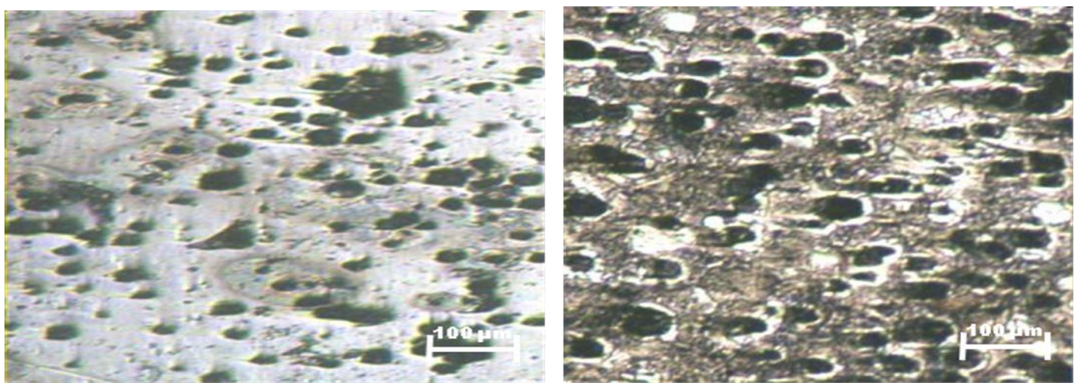


a b

Plate 57: Optical micrograph of 4mm thick section (a) unetched (b) etched of D4

Thermal conductivity dropped further but with slightly improved nodularity and nodule count. Matrix type is ferrite-pearlite for the three thicknesses (Figures 58-60).

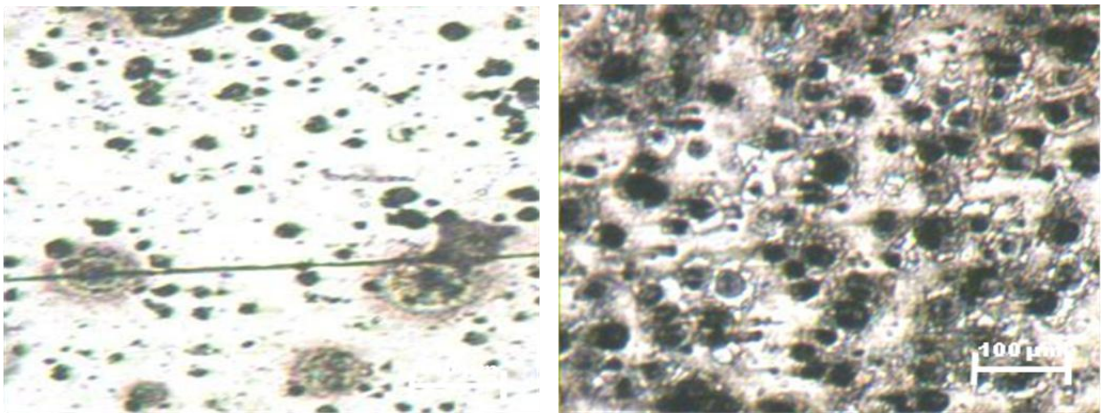

a b

Plate 58: Optical micrograph of 2mm thick section (a) unetched (b) etched of D5

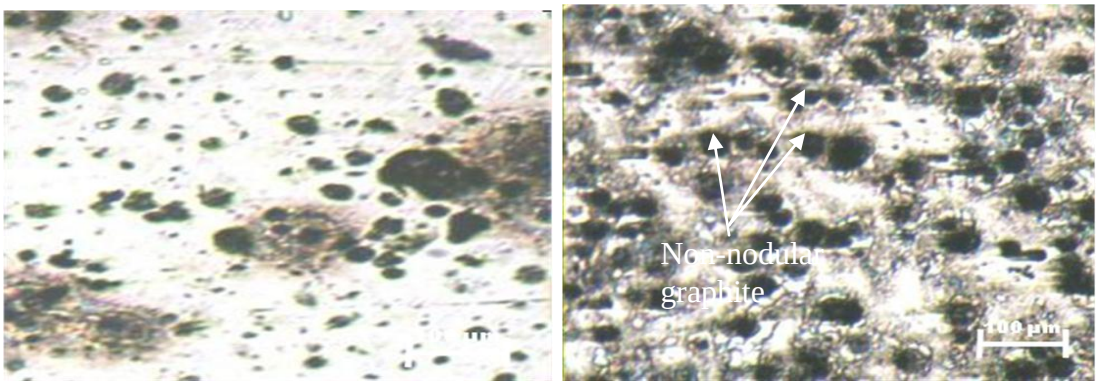


a b

Plate 59: Optical micrograph of 3mm thick section (a) unetched (b) etched of D5

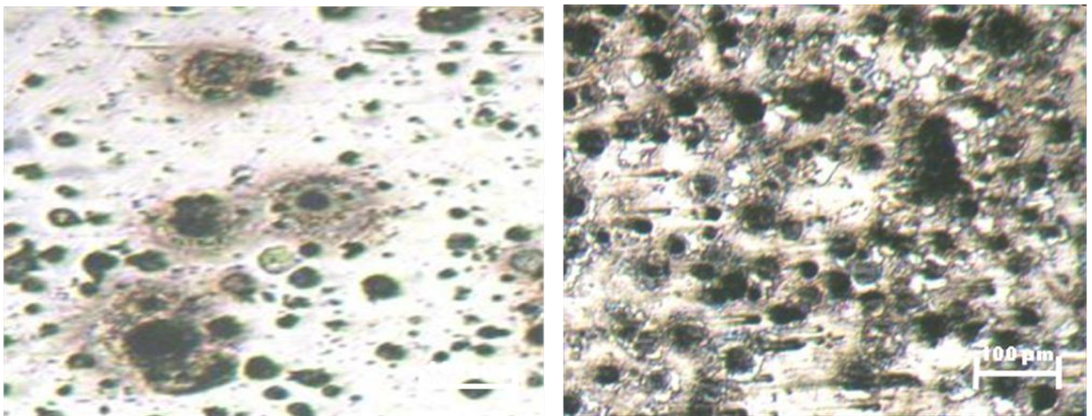

a b

Plate 60: Optical micrograph of 4mm thick section (a) unetched (b) etched of D5

Shape characteristics of formed nodules improved for 12 wt. % AlDr sand mix (Figures 61-63). Thermal conductivity dropped to 1.540 W/m K, which is lower than control sand mix (1.631 W/m K). This can be responsible for better microstructure observed in the ferrite-pearlite matrix.

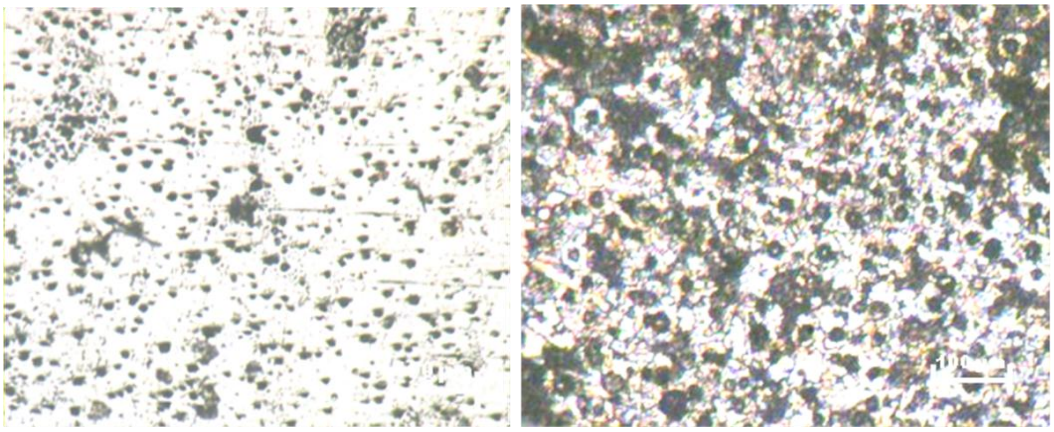

a b

Plate 61: Optical micrograph of 2mm thick section (a) unetched (b) etched of D6

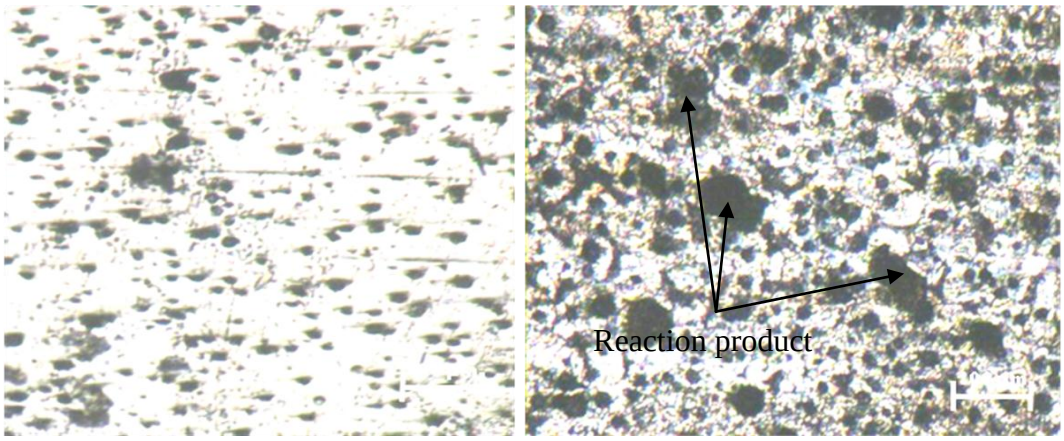


a b

Plate 62: Optical micrograph of 3mm thick section (a) unetched (b) etched of D6

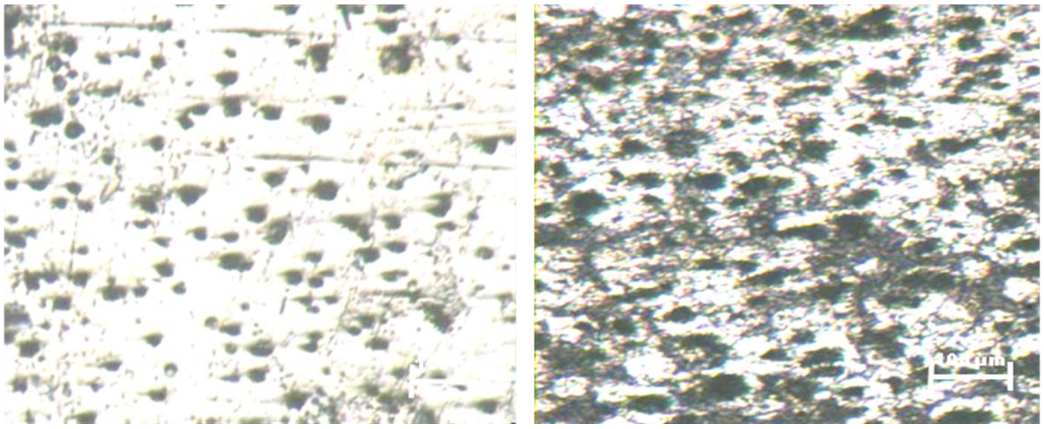

a b

Plate 63: Optical micrograph of 4mm thick section (a) unetched (b) etched of D6

### 4.6.2 Hardness Characteristics of TWDI castings produced in Moulding Sand-Al Dross Mix

The variation of brinell hardness number (BHN) with weight percent AlDr is shown in Figure 20. The values are highest for the control samples and these are: 179, 195

and 123 for 2, 3 and 4 mm thick samples, indicating that casting using the AlDr as moulding constituent lower the BHN. However, BHN values increased at 2-12 wt. % AlDr dropping slightly again at 10wt. % AlDr. These lower BHN values observed in samples cast from moulding sand- AlDr mix can be attributed to the suspected reaction product. This product must have had a softening effect on the matrix of samples.

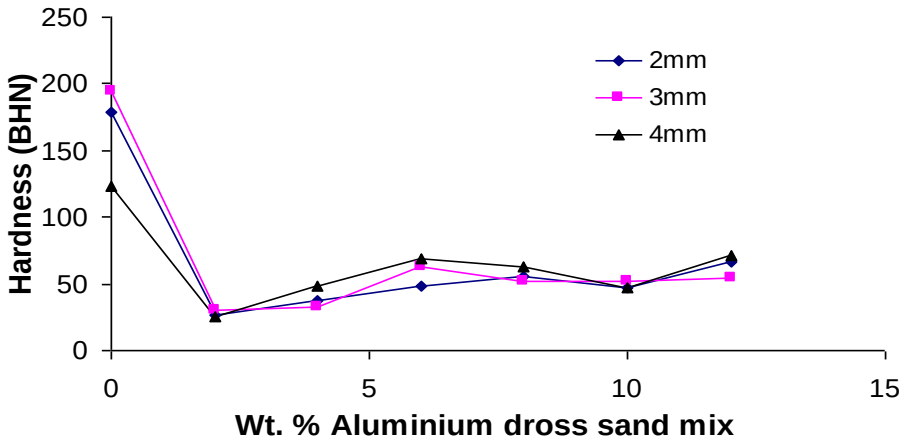


Figure 20: Variation of BHN with weight % Al Dross in sand-mix

### 4.6.3 Tensile Characteristics of TWDI castings produced in Moulding Sand-Al Dross Mix

The variation of ultimate tensile strength (UTS) with weight percent AlDr is shown in Figure 21. The UTS responses show that AlDr addition to sand mould negatively affected the UTS of the casts. The control samples that are cast in sand mould without AlDr addition gave the best UTS of 248, 300 and 389 MPa. The lowest UTS occurred at 2wt. % AlDr corresponding to the second lowest thermal conductivity value. This pattern is similar to that obtained for hardness responses. The percent elongation at fracture is higher from 8-12wt. % AlDr. Highest values of 4.5, 7.3 and 4.7 % at 12wt. % AlDr for 2, 3 and 4 mm thicknesses respectively are observed (Figure 22). Thus, the percent elongations of cast samples are high indicating that the dross-sand addition caused improved ductility, while sacrificing tensile strength. As mentioned previously the suspected aluminium-sulphur reaction product nucleated in the melt during solidification had a softening affect on the matrix of TWDI samples. The thermal conductivity dropped from 6-12 wt. %; cooling rate is reduced and further softening of matrix is suspected as percent elongations are highest for all thicknesses investigated at 12 wt. % AlDr (Figure 22).

Regression analysis used to correlate this effect shows that the percent elongation follows a quadratic relationship according to Equations 20, 21and 22 for 2, 3 and 4 mm thick samples respectively.

$$\%\ \text{Elong.}\ (2\text{mm}) = 0.0301(\text{AlDr}_{\text{Wt}\%})^2 - 0.1304(\text{AlDr}_{\text{Wt}\%}) + 1.7905 \qquad R^2 = 0.8328 \quad (20)$$

$$\%\ \text{Elong.}\ (3\text{mm}) = 0.0711(\text{AlDr}_{\text{Wt}\%})^2 - 0.4804\ (\text{AlDr}_{\text{Wt}\%}) + 2.8548 \qquad R^2 = 0.8849 \quad (21)$$

$$\%\ \text{Elong.}\ (4\text{mm}) = 0.0446(\text{AlDr}_{\text{Wt}\%})^2 - 0.5107(\text{AlDr}_{\text{Wt}\%}) + 4.2829 \qquad R^2 = 0.8940 \quad (22)$$

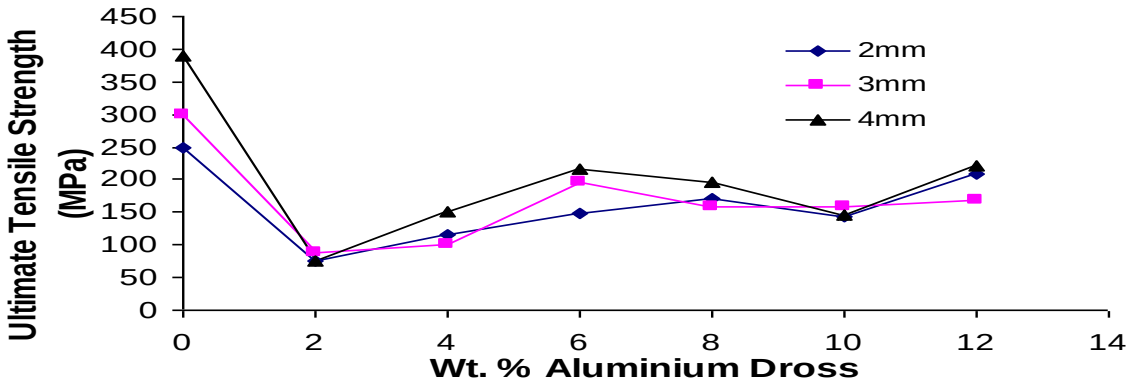


Figure 21: Variation of UTS with weight % Al dross in sand mix

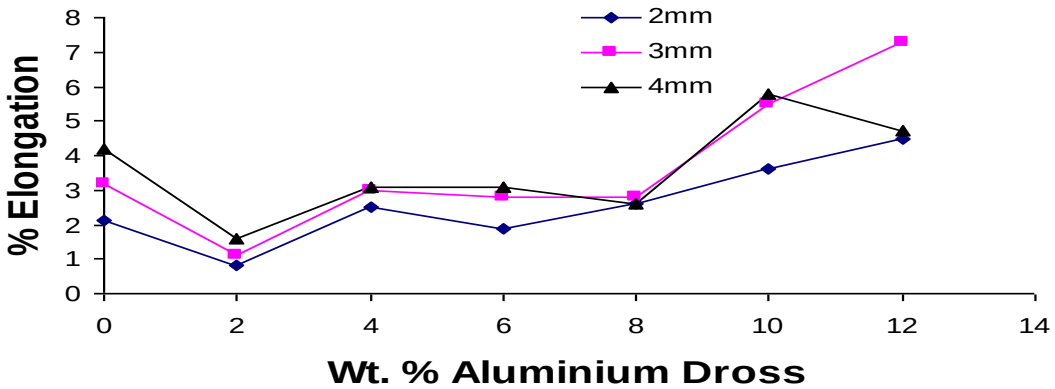


Figure 22: Variation of percent elongation with weight % Al dross in sand mix.

### 4.7 Effect of rice husk ash (RHA) moulding sand additive

Figures 23-27 show the graphs of green shear strength, permeability, % compactibility, moisture content and shatter index with weight % RHA respectively. The addition of the RHA additive increased green sand strength initially to 97 KN/m$^2$ but reduced slightly as it increased. Permeability decreased as the wt. % of RHA increased. Percent compactibilty, moisture content and shatter index reduced as the additive was increased.

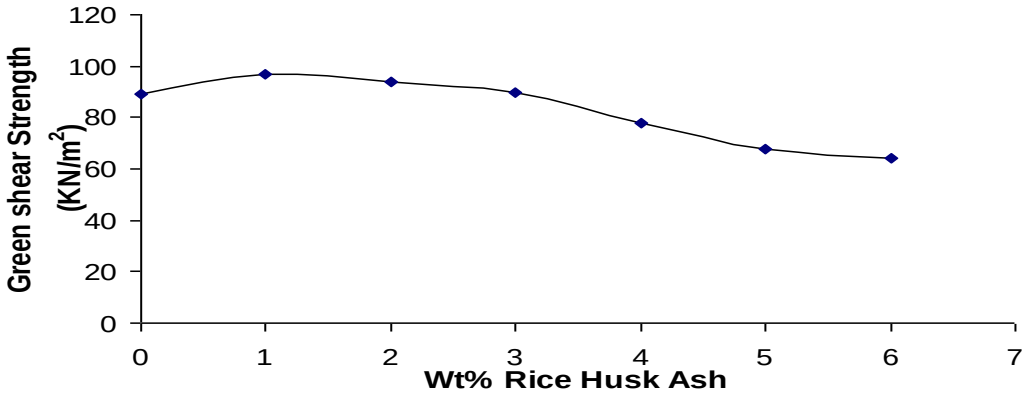


Figure 23: Variation of Green Shear Strength with Weight % RHA in sand mix

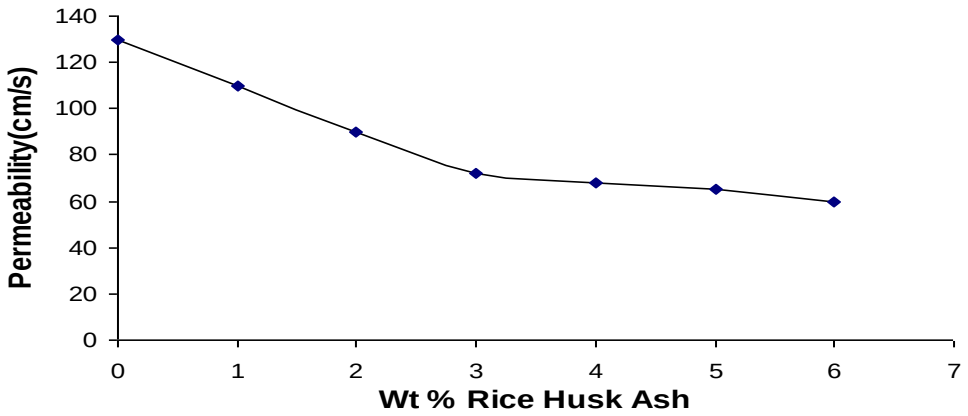


Figure 24: Variation of Permeability with Weight % RHA in sand mix

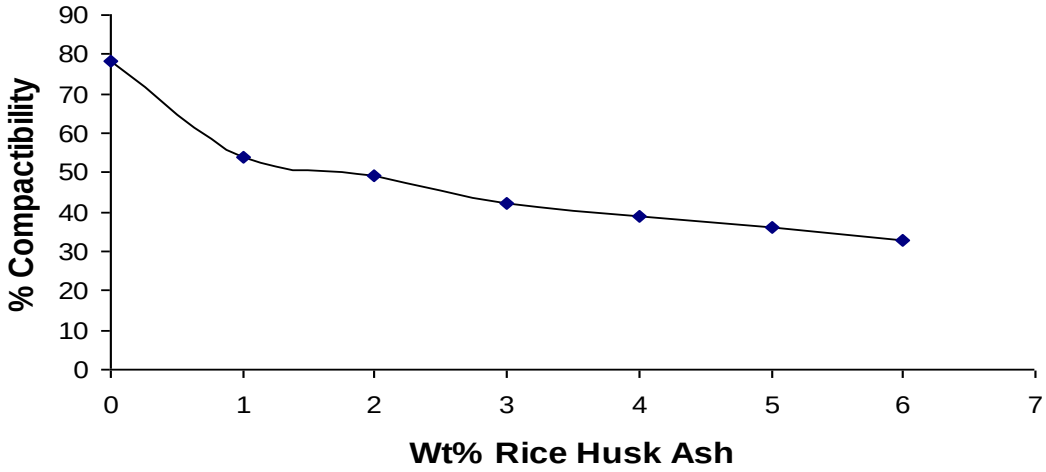


Figure 25: Variation of % Compactibility with Weight % RHA in sand mix

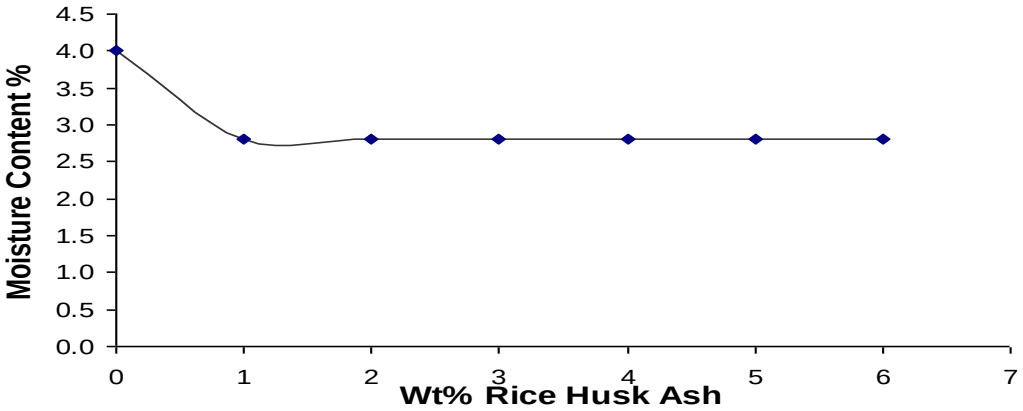


Figure 26: Variation of % Moisture Content with Weight % RHA in sand mix

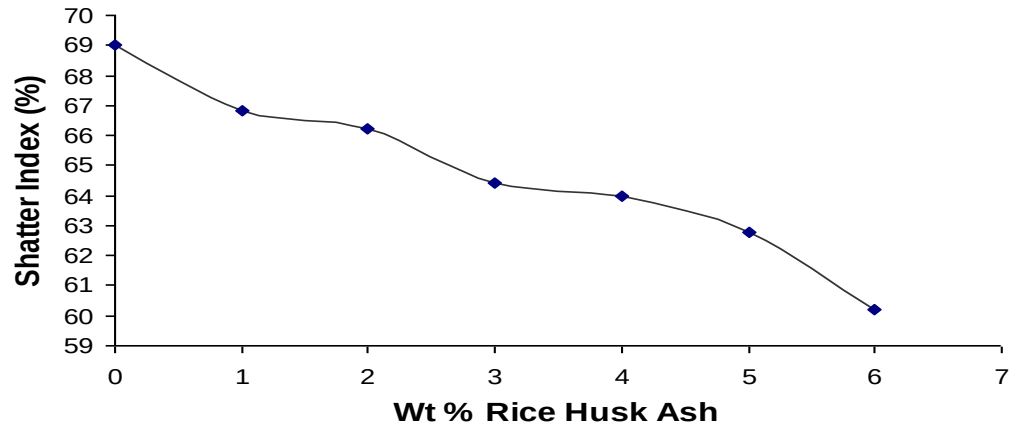


Figure 27: Variation of Shatter Index with Weight % of RHA in sand mix

Figure 28 shows variation of thermal conductivity of the sand mixes with weight % RHA additive. The thermal conductivity reduced as the wt. % of RHA is increased showing that some measure of thermal insulation of the sand mix was achieved. Using RHA as additive, thermal conductivity reduces by 30% as thermal conductivity of control sample without RHA is 1.631 W/m.K and that with 6 wt% RHA is 1.141 W/m.K. Showmann and Aufderheide, (2003) noticed similar results using low density alumino-silicate sand (LDASC) as sand additive/replacement in the study on thin wall casting technology.

Regression analysis shows that the relationship follows a downward exponential trend as in Equation 23.

$$\textit{Thermal Conductivity} = 1.6866e^{-0.0626\,(Wt\,\%\,RHA)} \qquad R^2 = 0.9711 \qquad (23)$$

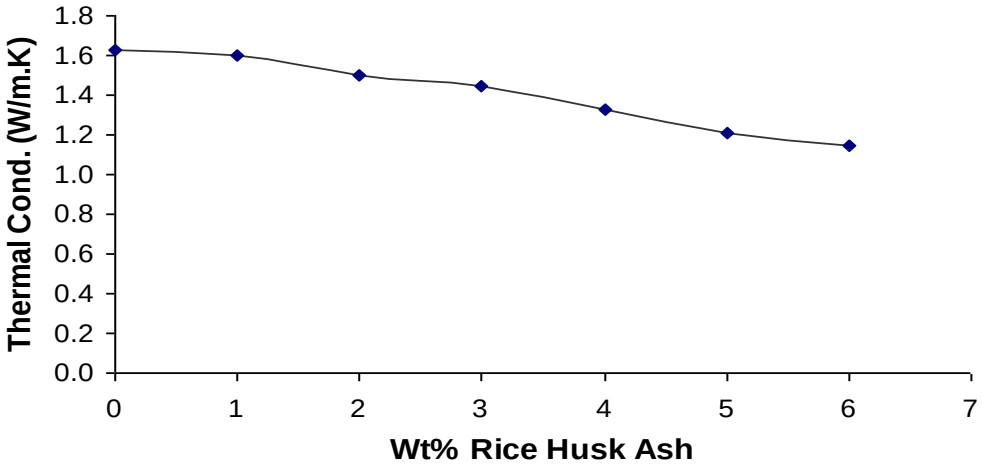


Figure 28: Thermal Conductivity of sand- RHA mix

### 4.7.1 Microstructural Analysis of Sand – RHA TWDI Cast Samples

Microstructure of TWDI cast samples is greatly enhanced by addition of RHA to silica moulding sand. Desired nodule characteristics i.e., shape, size and number are observed leading to good nodularity rating and high nodule count (Plates 67-84). The number of nodules continues to increase as the rice husk ash additive wt.% increases, regardless of the sectional thickness. Higher nodule count results to better TWDI properties.

Nodularity rating reached ninety percent (90%) for all samples while the nodule count for RH5 and RH6 samples are very high exceeding 1000 nodules/mm$^2$ (Table 11) leading to structure homogeneity (Labrecque *et al.*, 2005). The matrix consists of varying proportions of ferrite and pearlite mostly of the bull-eye structure. Pearlite structure is highest in RH4 samples, but reduces in RH5 and RH6 samples due to further carbon diffusion giving way to larger ferrite matrix proportion.

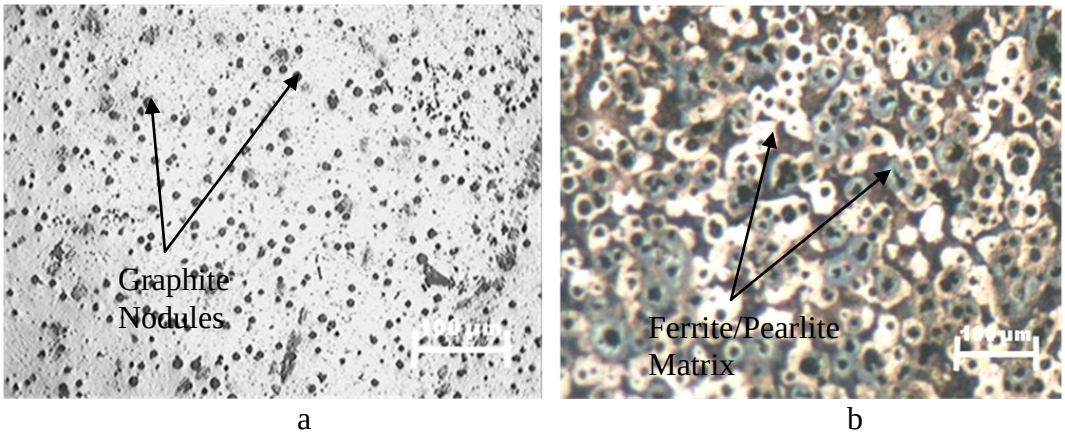


a b

Plate 64: Optical micrograph of 2mm thick section (a) unetched (b) etched of RH

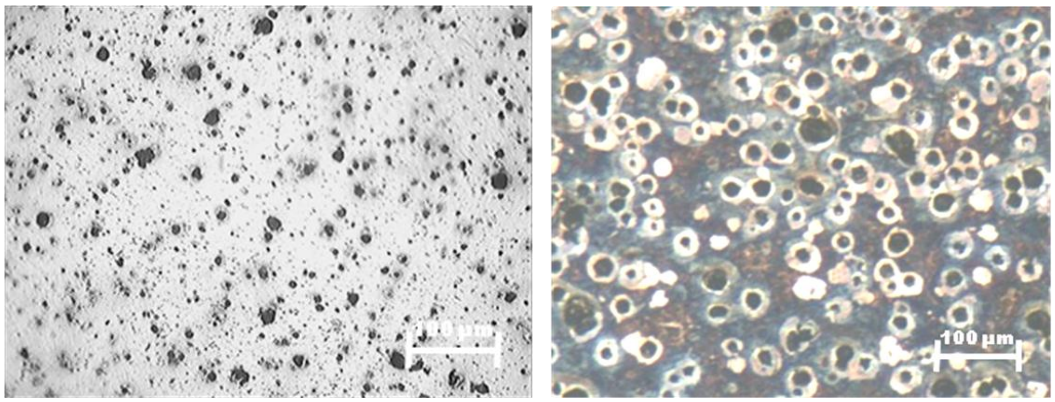


a b

Plate 65: Optical micrograph of 3mm thick section (a) unetched (b) etched of RH

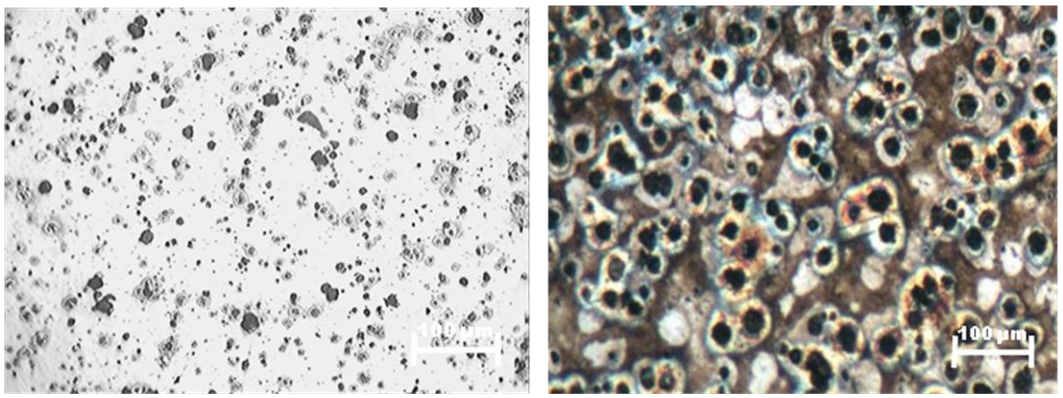


a b

Plate 66: Optical micrograph of 4mm thick section (a) unetched (b) etched of RH

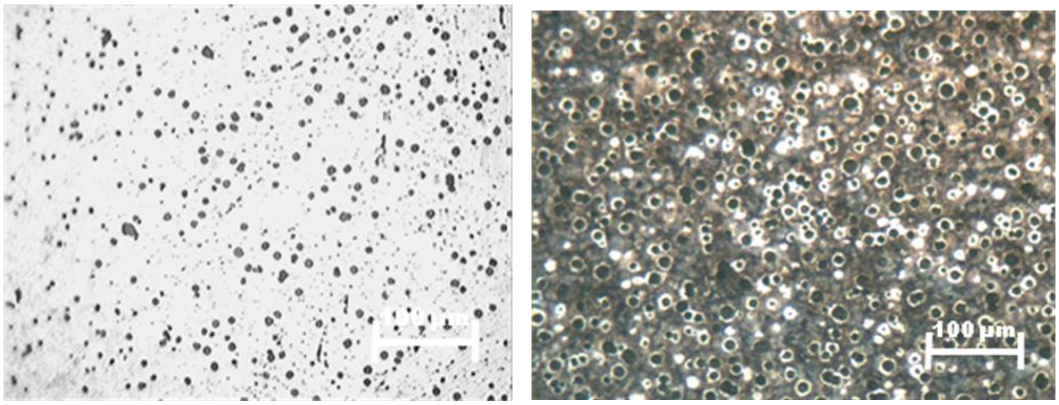


a b

Plate 67: Optical micrograph of 2mm thick section (a) unetched (b) etched of RH1

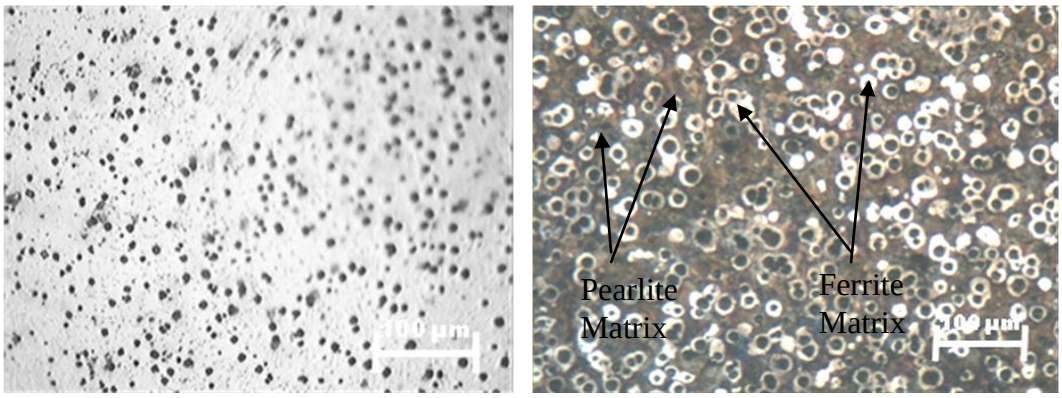


a b

Plate 68: Optical micrograph of 3mm thick section (a) unetched (b) etched of RH1

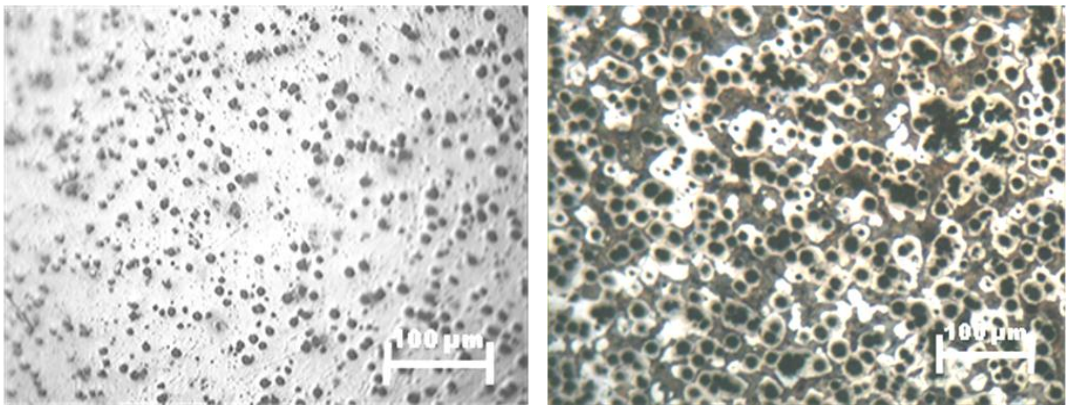

a b

Plate 69: Optical micrograph of 4mm thick section (a) unetched (b) etched of RH1

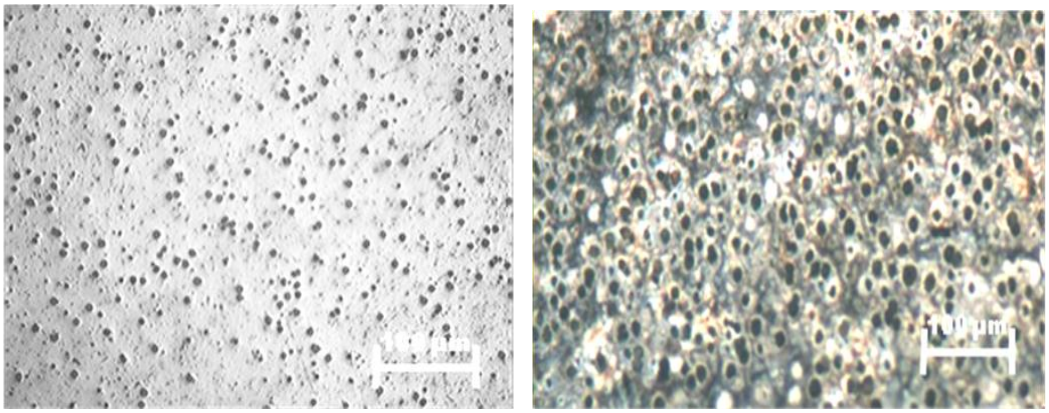

a b

Plate 70: Optical micrograph of 2mm thick section (a) unetched (b) etched of RH2

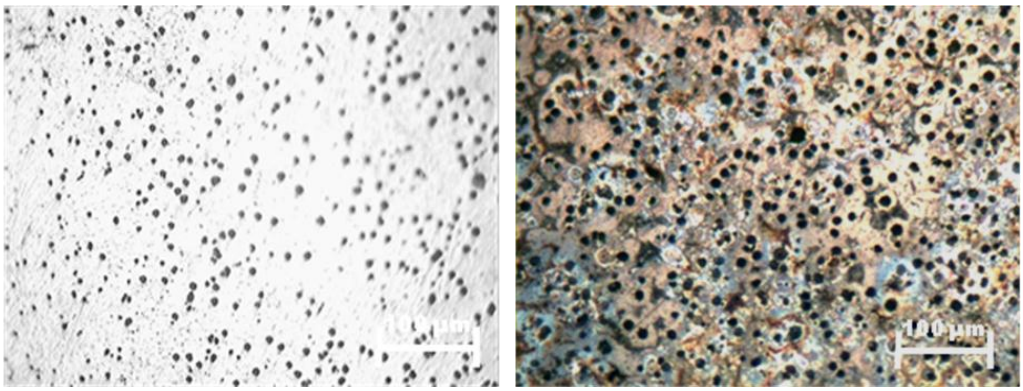

a b

Plate 71: Optical micrograph of 3mm thick section (a) unetched (b) etched of RH2

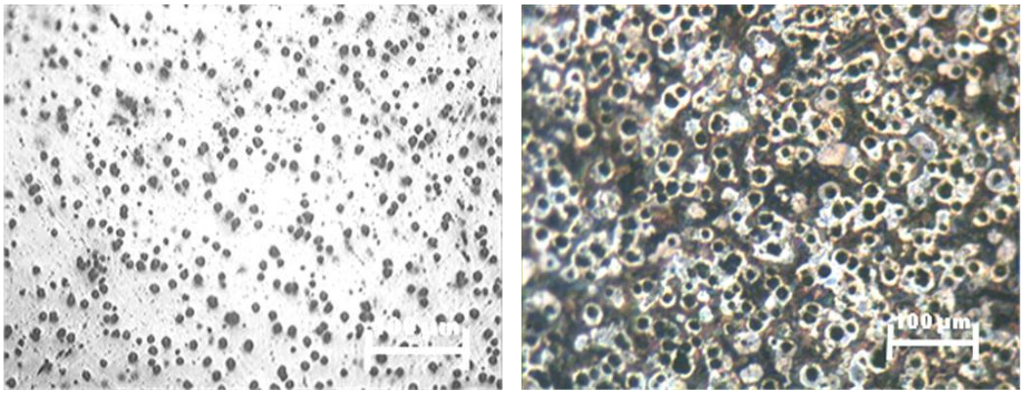

a b

Plate 72: Optical micrograph of 4mm thick section (a) unetched (b) etched of RH2

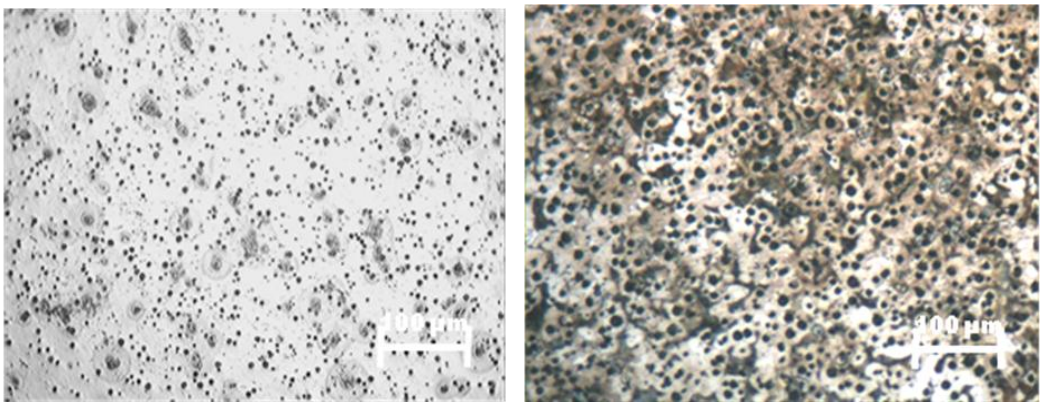

a b

Plate 73: Optical micrograph of 2mm thick section (a) unetched (b) etched of RH3

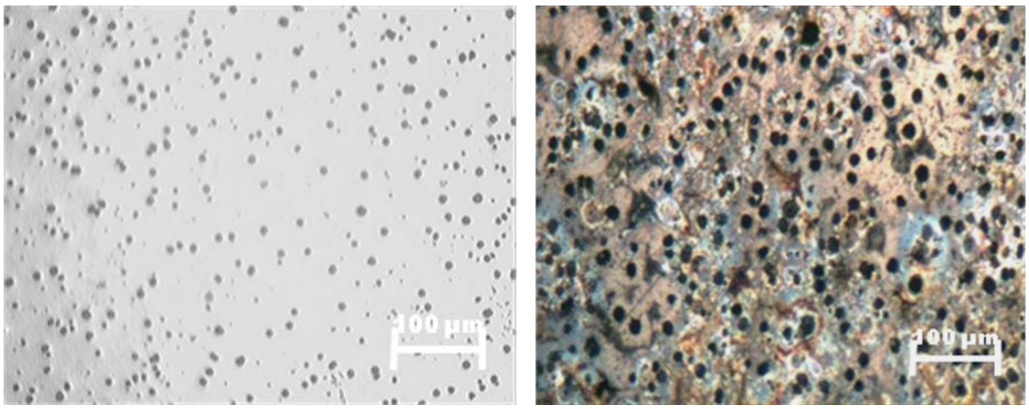


a b

Plate 74: Optical micrograph of 3mm thick section (a) unetched (b) etched of RH3

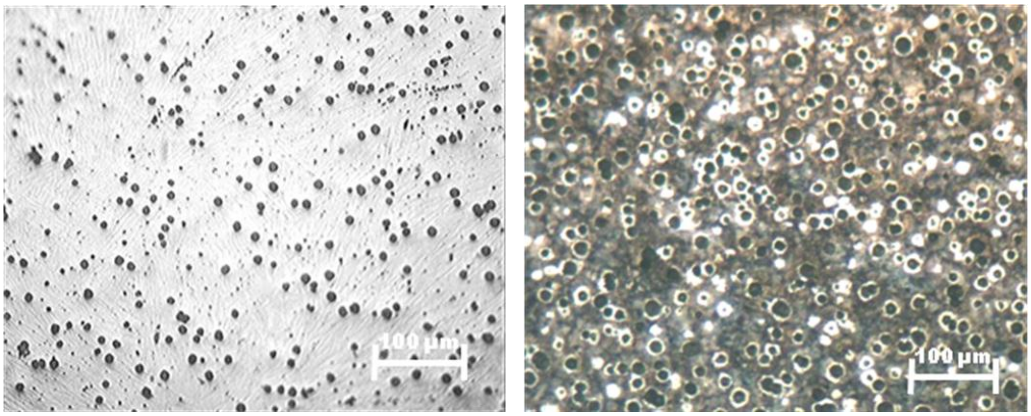


a b

Plate 75: Optical micrograph of 4mm thick section (a) unetched (b) etched of RH3

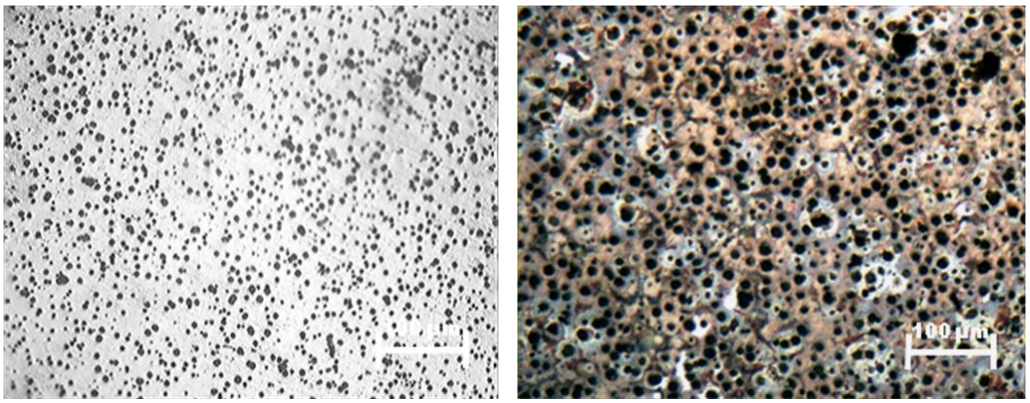


a b

Plate 76: Optical micrograph of 2mm thick section (a) unetched (b) etched of RH4

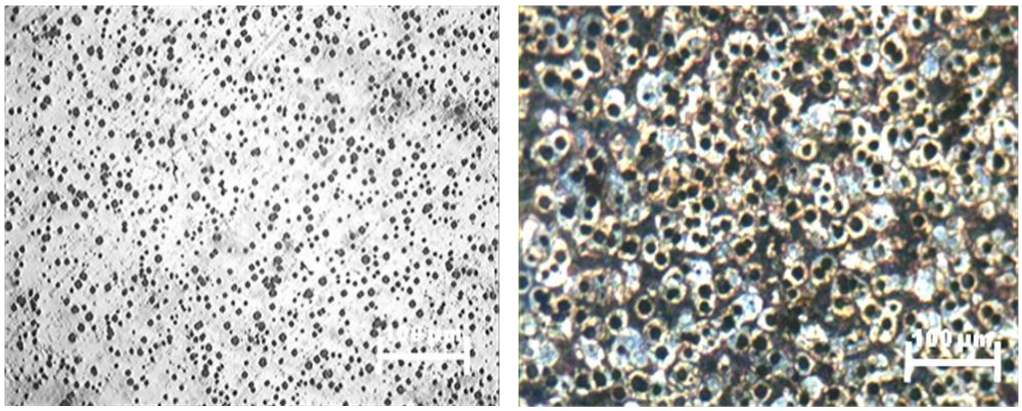

a b

Plate 77: Optical micrograph of 3mm thick section (a) unetched (b) etched of RH4

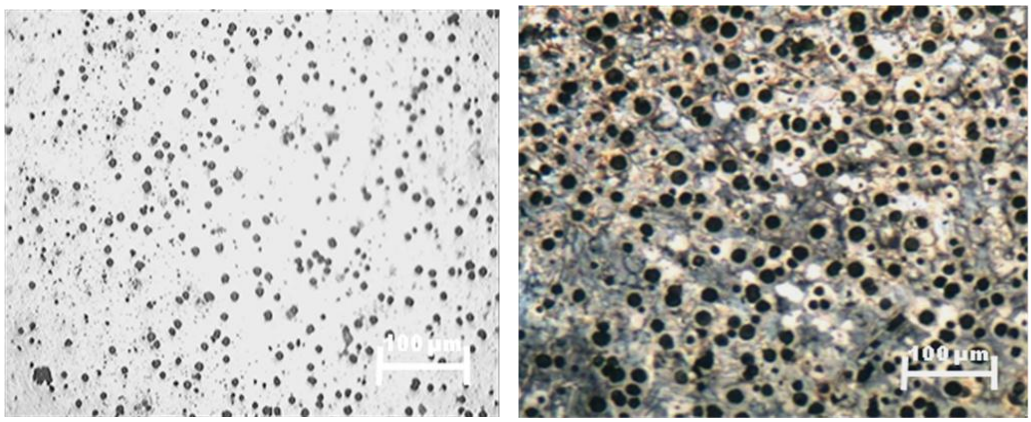

a b

Plate 78: Optical micrograph of 4mm thick section (a) unetched (b) etched of RH4

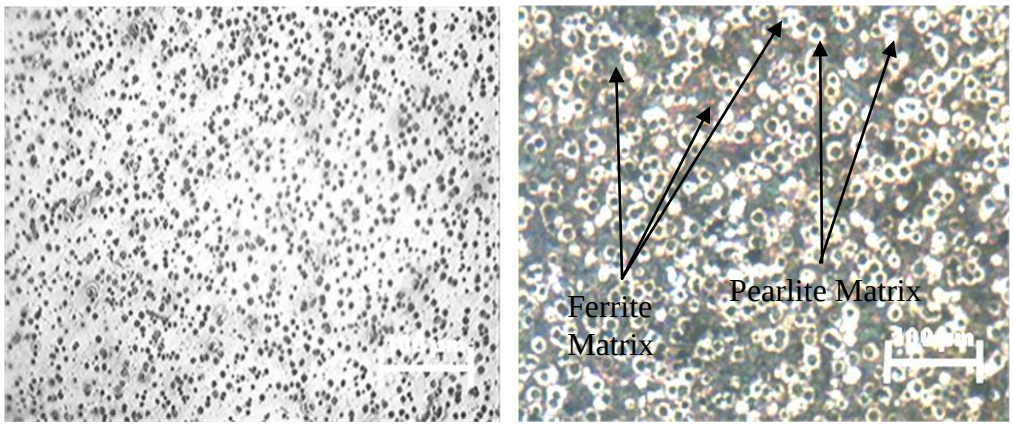


a b

Plate 79: Optical micrograph of 2mm thick section (a) unetched (b) etched of RH5

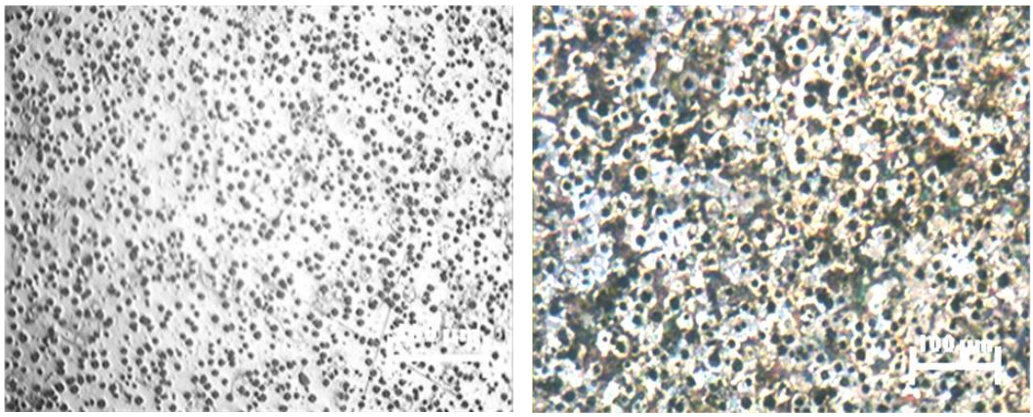

a b

Plate 80: Optical micrograph of 3mm thick section (a) unetched (b) etched of RH5

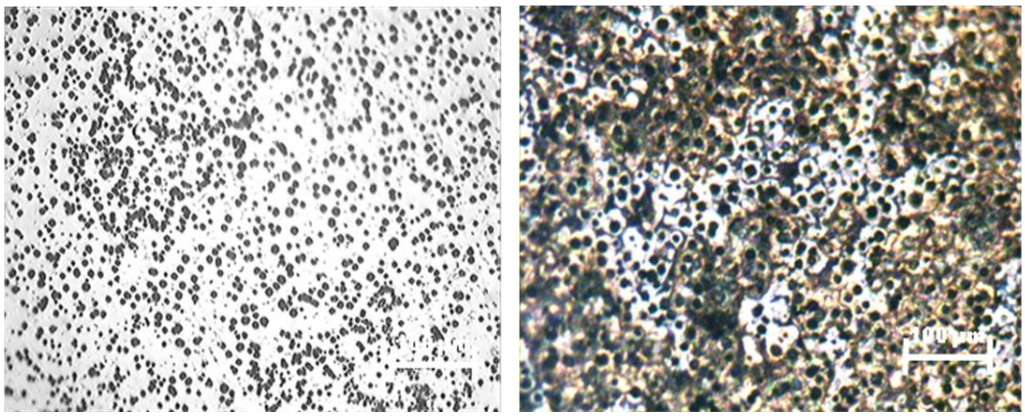

a b

Plate 81: Optical micrograph of 4mm thick section (a) unetched (b) etched of RH5

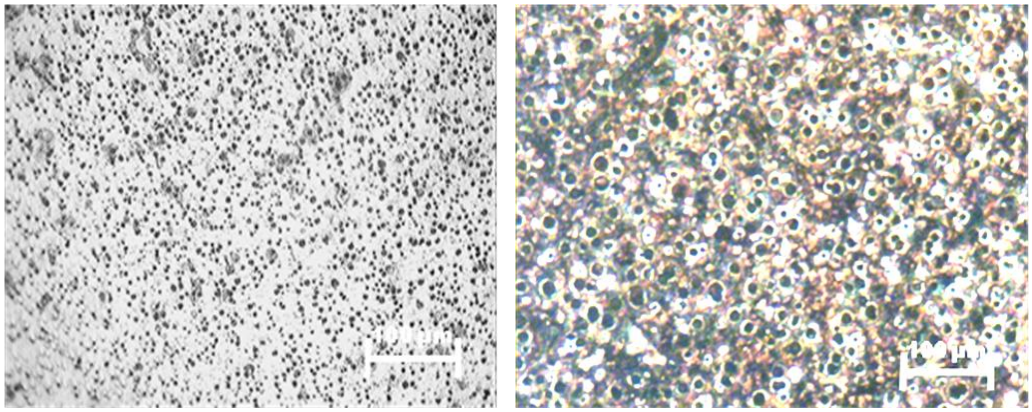

a b

Plate 82: Optical micrograph of 2mm thick section (a) unetched (b) etched of RH6

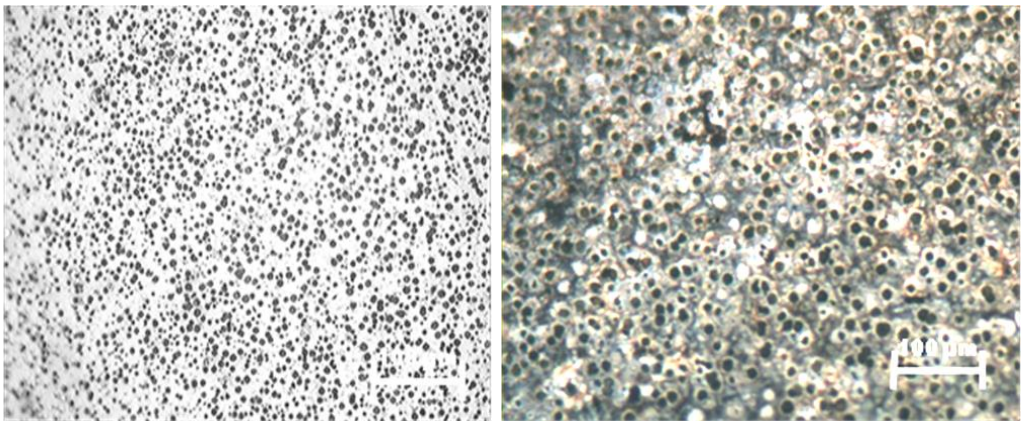

a b

Plate 83: Optical micrograph of 3mm thick section (a) unetched (b) etched of RH6

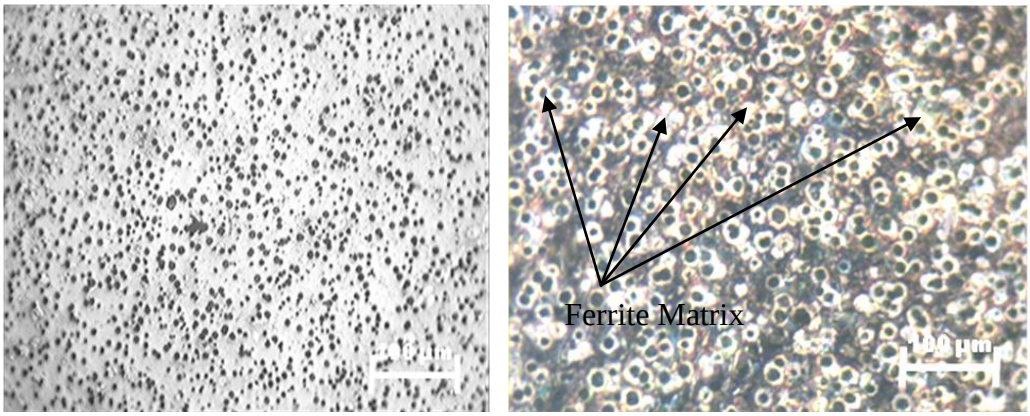


a b

Plate 84: Optical micrograph of 4mm thick section (a) unetched (b) etched of RH6

### 4.7.2 Nodularity and Nodule Count

The reduction in thermal conductivity resulting from RHA addition to moulding sand had a positive impact on nodule count and nodularity due to reduction in cooling rate. Table 11 shows nodularity and nodule counts for these TWDI samples.

Table 11: Nodularity and nodule count results for RHA samples

| **No** | **Sample** | **Nodularity (%)** | **Nodule Count (nodules/mm$^2$)** |
|---|---|---|---|
| 1 | RH-2 | 84 | 341 |
| 2 | RH-3 | 83 | 361 |
| 3 | RH-4 | 75 | 347 |
| 4 | RH1-2 | 98 | 678 |
| 5 | RH1-3 | 95 | 497 |

| | | | |
|---|---|---|---|
| 6 | RH1-4 | 94 | 364 |
| 7 | RH2-2 | 98 | 547 |
| 8 | RH2-3 | 97 | 533 |
| 9 | RH2-4 | 98 | 627 |
| 10 | RH3-2 | 90 | 721 |
| 11 | RH3-3 | 97 | 544 |
| 12 | RH3-4 | 96 | 496 |
| 13 | RH4-2 | 97 | 1376 |
| 14 | RH4-3 | 97 | 1458 |
| 15 | RH4-4 | 96 | 521 |
| 16 | RH5-2 | 97 | 1693 |
| 17 | RH5-3 | 98 | 1431 |
| 18 | RH5-4 | 98 | 1373 |
| 19 | RH6-2 | 98 | 1974 |
| 20 | RH6-3 | 97 | 1521 |
| 21 | RH6-4 | 95 | 1344 |

### 4.7.3 Hardness Analysis of sand – RHA TWDI cast samples

The variation of hardness with weight % RHA in TWDI cast with moulding sand-RHA mix is shown in Figure 29. Hardness increases up to 4 wt. % RHA, but drops at 5 and 6 wt. % RHA. This pattern agrees with investigation by Gorny and Tyrala, (2013) that cooling rate affects the maximum degree of under-cooling at the beginning of graphite eutectic solidification and, consequently on structure of iron (the number of graphite nodules, metal matrix). These high BHN at 4 wt. % RHA addition was the consequence of larger volume of pearlite phase in the matrix (Labrecque *et al.*, 2005; Sangame and Shinde, 2013), which dropped for 5 and 6 wt. % RHA. Increase in volume of ferrite phase is observed as a result of more graphite segregation from the reduction in cooling rate (Cebanne and Gagne, 2010; Gorny and Tyrala, 2013), leading to higher nodule count (>1000 nodules/$mm^2$). The 4 wt. % RHA corresponds to the highest BHN of 189, 207 and 219 for 2, 3 and 4 mm samples respectively.

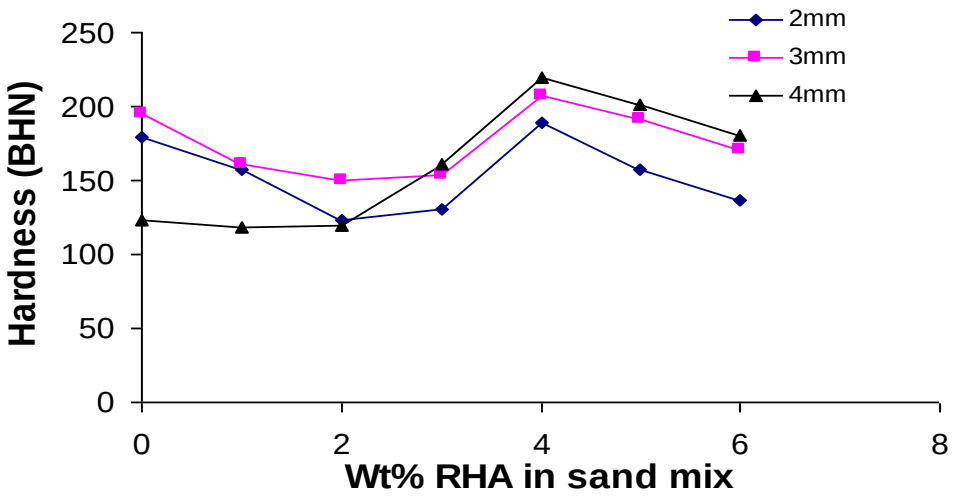


Figure 29: Variation of BHN of TWDI samples with Weight % RHA in sand mix

### 4.7.4 Tensile Test of sand – RHA TWDI cast samples

The UTS responses as in Figure 30 show that RHA addition improves this property in the cast samples. The control samples cast without the addition of RHA to moulding sand have UTS of 248, 300 and 389 MPa, which are the lowest tensile strengths. The highest UTS occurred at 4, 5 and 6 wt. % RHA. The highest UTS values of 564, 575 and 596 MPa for 2, 3 and 4 mm samples respectively are observed for samples cast using 4 wt. % RHA. This corresponds to the highest BHN, which is as a result of higher volume fraction of pearlite phase in matrix of Plates 76-78 (Labrecque *et al.*, 2005; Sangame and Shinde, 2013). The percent elongation at fracture is highest at 4-6 wt. % RHA in moulding sand. The highest values of 4.7, 5.8 and 6.1 is observed for 2,3 and 4 mm thick samples respectively at 6 wt. % RHA as shown in Figure 31. This is attributable to increased ferrite volume as cooling rate is further reduced at 4 to 6 wt. % RHA (Cebanne and Gagne, 2010). The study of Sangame and Shinde, (2013) also agrees with this finding as the study concluded that nodule count influences pearlitic content of as-cast DI. Increasing the nodule count decreases the pearlite content and tensile strength but increases % elongation.

Regression analysis shows that UTS of TWDI samples follows a quadratic relationship with wt. % RHA in Equations 24-26 for 2, 3 and 4 mm thick samples respectively.

$$UTS_{(2mm)} = -3.9155(RHA_{Wt.\%})^2 + 53.432(RHA_{Wt.\%}) + 229.22 \quad R^2 = 0.8601 \quad (24)$$

$$UTS_{(3mm)} = -2.7214(RHA_{Wt.\%})^2 + 64.479(RHA_{Wt.\%}) + 281.83 \quad R^2 = 0.9467 \quad (25)$$

$$UTS_{(4mm)} = -3.1679(RHA_{Wt.\%})^2 + 52.389(RHA_{Wt.\%}) + 375.83 \quad R^2 = 0.9477 \quad (26)$$

Regression analysis of percent elongation of TWDI samples with wt. % RHA follows a linear relationship as in Equations 27-29 for 2, 3 and 4mm thick samples respectively.

$$\%_{\text{Elong.}}(_{2mm}) = 0.4107(\text{RHA}_{\text{Wt. \%}}) + 2.025 \qquad (R^2 = 0.9684) \qquad (27)$$

$$\%_{\text{Elong.}}(_{3mm}) = 0.3893(\text{RHA}_{\text{Wt. \%}}) + 3.0607 \qquad (R^2 = 0.9196) \qquad (28)$$

$$\%_{\text{Elong.}}(_{4mm}) = 0.1886(\text{RHA}_{\text{Wt. \%}}) + 4.2619 \qquad (R^2 = 0.9826) \qquad (29$$

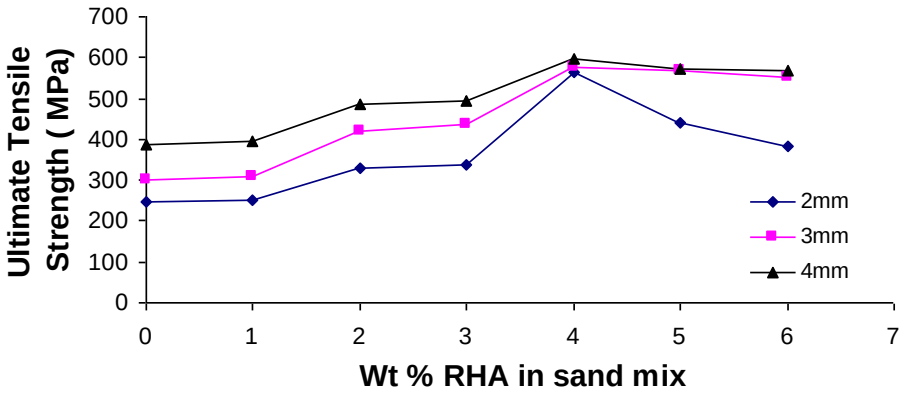


Figure 30: Variation of UTS of TWDI samples with weight % RHA

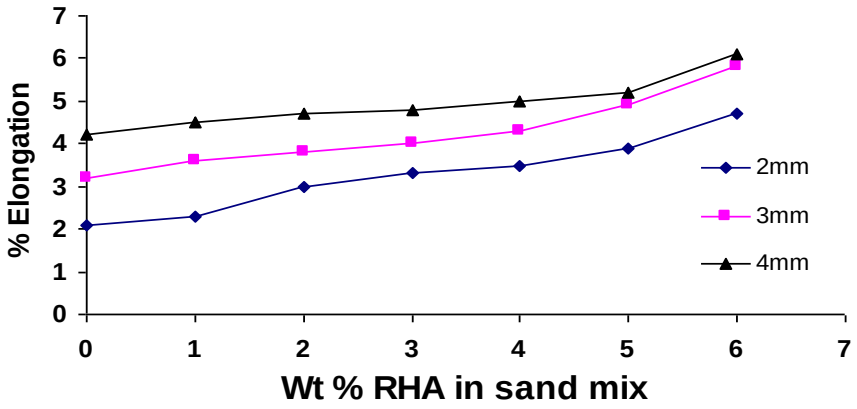


Figure 31: Variation of Percent elongation of TWDI samples with weight % RHA

### 4.8 Discussion

This study has shown that proper mould filling can be achieved by using the 'side gating casting design' as it enhanced the production of defect free TWDI. It should be noted as well that sprue/ metal height is found to be an important gating system parameter to be considered during casting of TWDI. This parameter directly influences pressure and velocity of advancing metal front as it helps in mould filling

and thus, contributes to the properties of the cast TWDI part. The 50 mm sprue height is not sufficient to push melt through the gating channels effectively leading to poor run and incomplete filling of mould cavity. However, sprue heights of 100 to 350 mm gave properly filled moulds. The 350 mm sprue height, however, yielded castings with inferior UTS of 101, 123 and 134 MPa and 0.3, 0.2 and 0.3 % elongation for 2, 3 and 4 mm respectively (Figures 9 and 10). The 100 mm sprue height yields good hardness of 198, 193 and 215 BHN (Figure 8); UTS of 596, 578 and 651MPa and 2.2, 2.3 and 4.4 % elongation for 2, 3 and 4 mm respectively (Figures 9 and 10) . The UTS and BHN values are within the ASTM Spec. No. A536-80 (80-50-06) with ferrite/pearlite matrix used for automotive components. However, elongation values are still very low as the specification recommends 6 % elongation for automotive application. Thus, the import of the above results is that metal head/sprue height is a vital gating system component to be considered in order to achieve proper mould filling and desired BHN and UTS properties of TWDI castings.

Proper inoculation and nodularisation treatments are vital in TWDI production; treatment technique and temperature are crucial factors to be considered. Magnesium, the vital element of the nodularizing ferro-alloy is a powerful carbide promoter (Davis, 1996). This study shows that higher treatment temperatures of 1550, 1530 and $1510^0$C favours the formation of carbide precipitates (Plates 22-30). This can be attributed to the kinetics of the reaction at this elevated temperature in treatment ladle. This high temperature initiates more spontaneity/ agitation in the reaction. This consequently destroys nuclei and impacts negatively on magnesium recovery, resulting to reduction in sites that would have been available for heterogeneous nucleation of graphite nodules. These caused low yields of the treatment process; this low yield process is undesirable as it impedes nucleation and growth of graphite nodules during solidification. However, it favours the formation of non-nodular graphite structures and carbide precipitates, which ultimately reduces ductility by lowering nodule count and nodularity (Sangame and Shinde, 2013). This indicates that nodularisation and inoculation are not the only cause of carbide precipitation. Therefore, all potential avenues need to be explored to determine the mechanism behind carbide formation. As the treatment temperature is reduced to 1490, 1470 and $1450^0$C (Plates 31-39), improved nodularity above 85% with improved nodule count (300-610 nodules/$mm^2$) are observed with inverse exponential relationship. Percent elongation improves at these temperatures (Figure 13) with the highest ductility of

2.6, 2.9 and 3.0 achieved at $1450^0$C for 2, 3 and 4 mm plates respectively. Further lowering of treatment temperature to $1430^0$C resulted to poor nodularity and nodule count as both microstructure and mechanical properties are impaired.

Thermal conductivity of moulding sand-AlDr mix is not favourable for casting TWDI as it causes high heat transfer/cooling rate and this hinders equilibrium eutectic transformation during solidification. Thermal conductivity increased for all sand mixes except for 12wt. % AlDr. Samples cast from the moulding sand- AlDr mix are structurally defective both in graphite shape characteristics and matrix type formed. It is difficult to determine the nodularity and nodules count as the graphite structures formed are mostly non- nodular in shape. The matrix shows the presence of a reaction product suspected to have resulted from reactions between constituents in AlDr and the molten metal. However, percent elongation increased at the expense of tensile strength and hardness properties of these samples. Highest elongation values of 4.5, 7.3 and 4.7 are observed for 2, 3 and 4 mm samples respectively at 12 wt. % AlDr (Figure 22). This can be attributed to the matrix softening effect caused by the suspected reaction product and lowest thermal conductivity obtained at 12 wt. % AlDr.

Samples cast using RHA-sand mix shows good microstructures and mechanical properties. This is mainly attributed to ability of mix to lower thermal conductivity (Figure 28). The heat transfer during the sample solidification process favours formation of equilibrium transformation products i.e., graphite structures instead of metastable carbide precipitates.

The matrix microstructure in DI is the result of austenite decomposition. The as-cast microstructure consists of ferritic and pearlitic bull-eyed structure, which is directly influenced by alloy content and cooling rate (Sangame and Shinde, 2013). The cooling rate is affected by the section thickness and rate of heat removal. This in turn depends on mould geometry (casting design), material, treatment and pouring temperature. Thus, the mechanical properties of TWDI are influenced by graphite shape characteristics and matrix type.

Tensile strength and BHN show similar trend for all the sand mix i.e., increasing up to 4 wt. % RHA (Figures 29 and 30). However, these drop slightly at 5 and 6 wt. % RHA, due to increased graphite segregation. Increased graphite segregation results from increased solidification time, which favours more active nuclei for graphite nodule formation as in the case of reduced solidification time for moulds of higher

thermal conductivity. This leads to increased nodule count, better structure homogeneity (Labrecque *et al.*, 2005), increased volume of ferrite phase and desired elongations (ie better ductility) of 4.7, 5.8 and 6.1. These properties meet the mechanical properties as specified in ASTM Spec. No. A536-80 (80-50-06) used for automotive application.

# CHAPTER FIVE

# 5.0 SUMMARY OF FINDINGS AND CONCLUSION

## 5.1 Summary of Findings

| S/N | OBJECTIVES | FINDINGS |
|---|---|---|
| **1** | To eliminate melt flow and solidification defects in 2-4 mm TWDI through gating and sprue designs and determine sample mechanical properties | Side feeding design gave defect free castings i.e., no incomplete filling, cold-shuts and mis-run. UTS and ductility improved from 101-596, 123-578 and 134-651MPa (above 300% increase) and 0.3-2.2, 0.2-2.3 and 0.3-4.4 % elongation (above 600% increase) for 2, 3 and 4 mm thick samples respectively from 350-100 mm sprue height. |
| **2** | To proffer melt treatment temperatures for the control or elimination of primary carbide precipitates and non-nodular graphite structures in TWDI castings. | Industry treatment temp. of 1450 $^{0}$C yielded enhanced nodularity > 95% and nodule count 450-610 nodules/mm$^{2}$ Improved ductility, about 200 % increase (0.7 - 2.6), (0.8 - 2.9) and (0.8 - 3.0%) for 2, 3 and 4mm, with control of carbide precipitates. |

| | | |
|---|---|---|
| **3** | To develop a mouldable insulating sand mix for control of cooling rate and solidification during casting for production of TWDIs exhibiting as-cast microstructure and mechanical properties meeting ASTM Spec. No. A536-80 for automotive application | 30% reduction in thermal conductivity is achieved at 6 wt. % RHA addition;<br>This corresponded to highest ductility of 4.7, 5.8 and 6.1% for 2, 3 and 4 mm thick samples respectively as cooling rate is reduced. Enhanced UTS of 564, 575 and 596 MPa is achieved. These mechanical properties are within ASTM Spec. No. A536-80 (80-50-06) having pearlite/ferrite matrix for automotive applications |
| **4** | To quantitatively determine nodule count and nodularity in relation to carbide precipitate control and mechanical properties of TWDI castings using ASTM A247 and E407 standard procedures. | High nodularity > 90% and high nodule counts > 1000 nodules/$mm^2$ occurred with significant control of carbide precipitates in RHA- sand mix cast samples.<br>Highest UTS of 564, 575 and 596 MPa occurred at 4 wt. % addition.<br>Desired UTS and ductility is achieved at 6 wt. % RHA additions (ASTM Spec. No. A536-80) |

## 5.2 Conclusion

This study has shown that defect free TWDI castings are achievable with proper gating design and dimensions. TWDI has viable potential in automotive application as a result of its high strength with good ductility, wear resistance, machinability and good fatigue properties. Sprue/ metal height is an important gating system parameter to be considered during casting of TWDIs. This parameter directly influences pressure, velocity of advancing metal front, efficiency of mould filling and heat transfer in gating channel, which in turn affect the properties of the finished component. It is recommended that the sprue height should be high enough to exert sufficient pressure and velocity on the advancing melt front but be kept as short as possible to prevent rapid heat transfer (under-cooling) and turbulent melt flow which lead to defective TWDI castings.

This work has also shown that $1430^0$C and $1550^0$C treatment temperatures are not adequate for desirable microstructure and ductility of TWDI castings.

The incorporation of RHA to silica moulding sand has significantly reduced thermal conductivity thereby reducing cooling rate. It allows sufficient time for formation of potent nuclei for graphite nodule formation thereby impeding precipitation of carbide phase. On the other hand, the introduction of aluminum dross in moulding sand aggravated the formation of non-nodular/deformed graphite structures and poorly formed matrix in the microstructure of TWDI castings.

This study has shown that it is possible to obtain carbide free, good nodules and adequate nodule count in castings through in-ladle sandwich nodularization treatment method accompanied by two step inoculation treatment. Lower treatment temperatures of $1450^0$C and $1470^0$C promote adequate magnesium recovery, better microstructure and mechanical properties. But treatment temperature below $1450^0$C is not desirable as mechanical properties are significantly impaired.

## 5.3 Contributions to Knowledge

The contributions of this research in the field of automobile foundry technology are:

1. A casting process assembly for production of sound TWDI casting (2-4 mm) has been proffered through proper gating and sprue design.
2. Industry nodularisation/inoculation treatment temperature of 1450 $^0$C for enhanced nodularity, nodule count with superior mechanical properties has been achieved for TWDI castings (2-4 mm).

3. An effective sand-RHA mouldable insulating mix for the control of cooling rate, deleterious carbides and superior graphite characteristics in TWDI castings has been developed.

### 5.4 Recommendation

Further characterization is recommended for the TWDI samples cast using sand-AlDr mix in order to determine precisely the reaction product and its reaction kinetics on UTS reduction and percent elongation improvement. The multiple regression analysis can be explored by other researchers to correlate the relationship of these independent variables on hardness, UTS and percent elongation of as-cast TWDIs**.**

**References**


Abed E. J., 2011. The Influence of Different Casting Method on Solidification Time and Mechanical Properties of Al-Sn Castings, *International Journal of Engineering and Technology. IJET-IJENS* .11(6): 26-33

Ahmad R and Hashim M. Y. 2011 Effect of Vortex Runner Gating System on the Mechanical Strength of Al-12Si Alloy Castings, *Archives of Metallurgy and Materials*. 56(4): 991-997

Ahmadabadi M., Niyama E., Abe T., Ohide T. 1994 Chemical Composition and Structural Identification of Eutectic Carbide in I PCT MN Ductile Iron. *Metallurgical and Materials Transactions A – Physical Metallurgical and Materials Science,* 25(5): 911 – 918.

Algarasamy A. 1992 Ductile Iron Handbook, (Ed. M. Burditt), *American Foundrymen Society (AFS)*, 197.

Berdin C., Dong M. J., Prioul C. 2001 Local Approach of Damage and Fracture Toughness for Nodular Cast Iron. *Engineering Fracture Mechanics* 68:1107-1117

Bockus S., Zalgarys G. 2009 Influence of the Section Size and Holding Time on the Graphite Parameters of Ductile Iron Production, *Metallurgija* 48:19-22.

Bockus S., Venckunas A., Zaldarys G. 2008, Relation Between Section Thickness, Mictostructure and Mechanical Properties of Ductile Iron Castings [J]. Materials Science (MEDZIAGOTYRA), 14(2): 115.

Bockus S., Dobrovolskis, A. 2004, Peculiarity of Producing Ferritic Ductile Iron Castings, *Materials Science ISSN* 10 (1):1392-1320

Borrajo J M., Martinez R A., Boeri R E and Sikora J A. 2002 Shape and Count of Free Graphite Particles in Thin Wall Ductile Iron Castings, *ISIJ International*, 42(3):257-263.

Cabanne P. M and Gagné M 2010 Inoculation of Ductile Iron: Why and When? *Sorelmetal Technical Services.* Rio Tinto Iron & Titanium 115

Campbell J. 2000 Castings, Butterworth Heinemann, Boston

Caldera, M., Rivera, G. L., Boeri, R. E., Sikora, J. A**.** 2005 Precipitation and Dissolution of Carbides in Low Alloy Ductile Iron Plates of Varied Thickness *Materials Science and Technology* 21(10):1187 – 1191.

Choi J.H., Oh J.K., Choi C.O, Kim J. K and Rohatgi P. K., 2004 Effect of Rare Earth Elements on Microstructure Formation and Mechanical Properties of Thin Wall Ductile Iron Castings, *Journal of Material Science and Engineering.* A (383): 323-333.

David P, Massone J, Boeri R, Sikora J 2004 Mechanical properties of Thin Wall Ductile Iron-Influence of Carbon Equivalent and Graphite Distribution, *ISIJ International* 44: 1180-1187

Davidson J. H, 2003 Microstructure of Steel and Cast rons, New York, Springer-verlag, *ISBN 3-540-20963-8*, 21:356-363

Davis J. R, 1996 ASM Specialty Handbook Cast Irons. *ASM International. The Materials Information Society:* 65-68

Davis K. G., Sahoo M and Javaid A. 2000 *AFS Transaction*, 108: 191.

Dogan O, N, Schrems K. K, Hawk J, A 2003: *AFS Transactions* 111:949–959.

El Rayes M., 2007 Prediction of Solidification Time: Chvorinov's Rule

Flemings, M. C. 1974 Solidification Processing. McGraw-Hill Book Company, New York: 423.

Forrest R. D., 2006 Manual of Sorelmetal, Technical services, Rio Tinto Iron and Titanium

Fras E., Lopez H. F., 1998 A Theoretical and Experimental Study of the Dependence between Undecooling and Nodular Eutectic Grains Density, *Archives of Metallurgy*, 227-240.

Fraś E., Górny M., Kapturkiewicz W. 2013 Thin Wall Ductile Iron Castings: Technological Aspects, *Achives of Foundry Engineering, ISSN* (1897-3310) 13(1):23-28

Fraś E., Górny M., Lopez H. 2009 Thin Wall Ductile and Austempered Iron Castings as Substitutes for Aluminum Alloy Castings. *International Foundry Research*, 61 (3):2-10.

Gagne M., 2006 Thin wall Ductile Iron Castings: A Reality For Light Weight Automotive Parts. *Sorelmetal Technical Services.*

Goodrich G. M., 1990 Ductile Iron Nodule Count Affected by Molten Metal Processing, *Modern Castings*

Gorny M 2009. Temperature Drop in Liquid Iron In Thin Wall Channels during Mould Filling, *Archieves of Foundry Engineering*. 9 (1):137-142

Gorny M and Tyrała E., 2013 Effect of Cooling Rate on Microstructure and Mechanical Properties of Thin-Walled Ductile Iron Castings, *Journal of Materials Engineering and Performance*. 22(1):300–305

Halvaee A and Ardestani K., 2014 Effect of Casting Variables on Microstructure and Mechanical Properties of Thin wall Ductile Iron Castings. http://www.researchgate.net/publication/262413065

Hassan J., Idris M. H.,Qurdjini A., Karimian M., and Pyganeh G. 2010. Influence of Gating System, Sand Grain Size, and Mould Coating on Microstructure and Mechanical Property of Thin Wall Ductile Iron, *Journal of Iron and Steel Research, International*, . 17(12): 38-45

Iacoviello F and Di Cocco V. 2003 Fatigue Crack Paths in Ferritic-Pearlitic Ductile Cast Irons, *Proceedings of International Conference on Fatigue Crack Paths*. 116:18-20

Jappes W., Alavudeen A., Venkateshwaran N. 2006 *A Textbook of Engineering Materials and Metallurgy.* Laxmi Publication Ltd. 123-130

Javaid A, Thomson J, Sahoo M, Davis G K 2001 Effect of Microstructure on Mechanical properties on Thin Wall Ductile Iron castings, *AFS Transactions* 01(109): 1-18.

Kalpakjian S. 2008. *Manufacturing Processes for Engineering Materials*. Fifth Edition

Katzarov I. H., 2003. Finite Element Modelling of the Porosity Formation in Casting. *International Journal of Heat and Mass Transfer*. 46: 1545-1552.

Krestyanov, V. J. Some.,1991 Conditions for producing Nodular Iron with a High Complex of As-cast Mechanical Properties. *Foundry (Liteynoje Proizvodtvo)* 7: 2-5

Labrecque C., Gagné M., Javaid A., 2005 Optimizing the Mechanical Properties of Thin-Wall Ductile Iron Castings, *AFS Transactions Schaumburg*, IL USA. 05-116(05):1-10

Lee P.D., Chirazi A and See D., 2001. Modelling Micro-Porosity in Aluminium - Silicon Alloys: A Review. *Journal of Light Metals*. 1:15-30.

Li J., Lu L., Lai M. O. 2000, Quantitative Analysis of the Irregularity of Graphite Nodules in Cast Iron. *Materials Characterization*. 45:83-88.

Manjunath S., Nataraj H. M.and Prasad J. R. 2012. Design Optimization of Gating System by Fluid Flow and Solidification Simulation for Front Axle Housing, *International Journal of Engineering Research and Development*. 4(6):83-88.

Masoumi M. 2005 Effect of Gating Design on Mould Filling, *Transactions of the American Foundry Society*, 113: 185-196

Mid- Atlantic Castings Services. A Guide Ductile Iron Alloy Castings. A Technical paper (www.Mid-AtlanticCasting.com)

Minkoff I. 1983 *The Physical Metallurgy of Cast Irons* 55-63. John Wiley and Sons Ltd

Mullins J D 2006 The Most Important Part of Ductile Iron Production – Inoculation. *Sorelmetal Technical Services*

Mullins J. D., 2003 Manual of Sorelmetal, Technical Services, Rio Tinto Iron and Titanium

Naveen H and Sunil M, 2014 Casting Simulation for Sand Casting of Flywheel, *International Journal of Research in Advent Technology*. 2(8):82-86.

Naveenkumar and Bharat. S. K. 2014 Design Optimization of Gating System by Fluid Flow and Solidification Simulation for Pump Casing by Sand Casting, *International Journal of Research in Engineering and Advanced Technology*. 2(4):1-5

Olsen S O., Skaland T., and Hartung C. 2009 Inoculation of Grey and Ductile Iron, A Comparison of Nucleation Sites and some Practical Advises. Elkem ASA, Foundry Products Division, Norway

Onsoien M. I., Grong O., Skaland T., Olsen S.O., 1997 *AFS Transactions*. 105:147-152

Pavlak L. 2008. Effect of Filling Conditions on the Quality of Cast Aluminium Cylinder Heads, *Metalurgija: Journal of Metallurgy*, 14(1): 31-39

Pedersen K.M and Tiedje N.S 2008. Graphite Nodule Count and Size Distribution in Thin Walled Ductile Iron, *Materials Characterization*. 59(8):1111-1121. Elsevier

Ratto P. J. J., Ansaldi A. F., Fierro V. E. 2001 Low Temperature Impact Tests in Austempered Ductile Iron and Other Spheroidal Graphite Cast Iron Structures, *ISIJ International*, 41(4):372-380.

Rihan Y. 2010. Numerical Study on the Effect of Solidification Parameters during the Continuous casting of Al-Si Alloys, *The Online Journal on Mathematics and Statistics (OJMS)* 1(1)

Ruxanda R E, Stefanescu D M, Piwonka T S 2002 Microstructure Characterization of Ductile Thin Wall Iron Castings, *AFS Transactions* 02(177):1131-1147.

Sangame B. B., Shinde V. D 2013 The Effect of Inoculation on Microstructure and Mechanical Properties of Ductile Iron. *IOSR Journal of Mechanical and Civil Engineering (IOSR-JMCE) e-ISSN:* 2278-1684, 5(6):17-23 www.iosrjournals.org.

Schmidt D. 2010 Solid Cast, Effective casting simulation, Solidification Time.

Shafiee M. R. M. 2009 Effect of Gating Design on the Mechanical Strength of Thin Section Casting, *Journal of Material Processing Technology*, 105: 128-133

Sheikh M. A. 2008 Production of Carbide-Free Thin Ductile Iron Castings, Journal of University of Science and Technology Beijing. 15:552-555

Sheikh M. A and Iqbal J 2007 Effect of Lanthanum on Nodule Count and Nodularity of Ductile Iron, *Journal of Rare Earths* 25:533-536

Shinde V. D., Ravi B., Narasimhan K 2012 Solidification Behaviour and Mechanical Properties of Ductile Iron Castings with Varying Thickness, *International Journal of Cast Metal Research.* 000(000):1-10

Skaland T., Grong O., Grong I. 1993 A Model for Graphite Formation in Ductile iron. Inoculation Mechanisms, *Metallurgical and Materials Transaction* A (24A):2321-2345.

Skaland T 2005. Proceedings. *AFS Cast Iron Inoculation Conference.*, Schaumburg, IL, USA.13–30.

Skaland T and Grong O., 1991 Nodule Distribution in Ductile Cast Iron, *AFS Transaction*, 99:153–157Stefanescu D. M, Dix L. P., Ruxanda R. E., Corbitt-Coburn C., Piwonka T. S., 2002 Tensile Properties of Thin Wall Ductile Iron, *AFS Transactions*, 110:1149-1162

Soedarsono J. W., Soemardi T. P., Suharno B., Dewi R., Ariobimo S. 2011 Effects of Carbon Equivalent on the Microstructures of Thin Wall Ductile Iron, *Journal of Materials Science and Engineering.* 5: 266-27

Soiński M. S., Jakubus A., Kordas P., Skurka K. 2014 The Effect of Aluminium on graphitization of Cast Iron Treated with Cerium Mixture. *Archives of Foundry Engineering. ISSN* (1897-3310). 14(2):95 – 100

Stefanescu D. M., Ruxanda R., Dix L. P. 2003 The Metallurgy and Tensile Mechanical Properties of Thin Wall Spheroidal Graphite Iron. *International Journal of Cast Metals Research* 16(1-3): 319-324.

Takeda H., Yoneda H., Asano K. 2010 Effect of Silicon and Bismuth on Solidification Structure of Thin Wall Spheroidal Graphite Cast Iron, Materials Transactions, *The Japan Institute of Metals*, 51(1):176-185.

Venugopalan D., 1990 Prediction of Matrix Microstructure in Ductile Iron, *AFS Transaction*, 98:465–469

Voigt R. C 2002. Fillability of Thin-Wall Steel Castings. Principal Investigator, The Pennsylvania State University. osti.gov/bridge www/servlets/purl/801749-V2NuWi/native/.

Voigt R. C., Kim J., Richards V. L. 1997 Opportunities for Thin-Wall Steel Castings *Proceedings of the 1997 Steel Founder's Society of America, Technical & Operating Conference*, Chicago.

## APPENDIX A

Gating System Dimensions Calculations (Tata McCraw- Hill, P. L. Jain. 2003)

Density, ρ = **7200Kg/m$^3$**

**Top Feeding for 2mm Plates (No runners and ingates)**

Step 1: Total weight of casting W

W = ρ x V. (A1)

where W is total wt of casting (0.324kg as shown in Table B1)

V is volume of casting

Step 2: Pouring Rate (R)

Pouring rate formula for ferrous gating

$$R = \frac{w^p}{1.34 + \frac{t}{13.77}} \quad (A2)$$

$$R = \frac{(0.324)^{0.5}}{1.34 + \frac{2}{13.77}}$$

$$R = \frac{\sqrt{0.324}}{1.34 + 0.145}$$

Where t is pouring time, p is 0.5 for ferrous alloys.

$R = \frac{0.569}{1.485}$ = 0.383kg/s

$$R_a = \frac{R}{K.C} \quad (A3)$$

$R_a$ is adjusted pouring rate

where K= Metal fluidity, C= effect of friction with values of 0.85-0.90 for tapered sprues. K, for cast iron is determined after calculating the composition factor given as:

Composition factor = % total carbon + $\frac{1}{4}$ (% Si) + $\frac{1}{2}$ (% Phosphorus)

= 3.15 + $\frac{1}{4}$(2.49) + $\frac{1}{2}$ (0.019)

= 3.15 + 0.6225 + 0.0095

= 3.782 (Use 0.8 for K)

$R_a = \frac{0.383Kg/s}{0.8X0.85} = \frac{0.383}{0.68}$ = 0.563Kg/s

Pouring time, t = $\frac{W}{R_a} = \frac{0.324}{0.563}$ = 0.575seconds

Step 3: Effective Sprue height $-H_P$

$H_P$ = H-0.5$\frac{h_1^2}{h_2}$ (A4)

Where H is the sprue height

$h_1$= height of casting in cope = 1mm

$h_2$ = total height of casting = 2mm

$H_P$ = 100- 0.5$\frac{1^2}{2}$ = 100-0.25 = 99.75mm

Step 4: Choke cross sectional area $A_s = A_c$

$$A_s = A_c = \frac{W}{\rho t C \sqrt{2gH_p}} \quad \text{(A5)}$$

$$= \frac{0.324}{7200kg/m^3 x 0.575 x 0.8\ x\sqrt{2x9.81x0.09975}}$$

$A_c$= $\frac{0.324}{4633.25}$ = 6.99 x $10^{-5}$m$^2$

$A_c = 69.9$mm$^2$

$69.9 = \pi r^2$ , r = $\sqrt{\frac{69.9}{3.1416}}$ = 4.72, Choke diameter= 9.44mm$^2$

Step 5: The sprue Inlet area

From Law of continuity Q=$A_1V_1$ =$A_2V_2$ Where Q is flow rate but V= 2gh (Bernoullis Equation)

$A_1$ = $A_2\frac{\sqrt{H_2}}{\sqrt{H_1}}$ (A6)

where $H_1$ is the distance between the ladle and the sprue top = 50mm and $H_2$ is the distance between the ladle and sprue exit = 150mm

$A_1$ = 69.9 x $\frac{12.24}{7.07}$ =121mm$^2$

Sprue inlet radius = $\sqrt{\frac{121}{3.1416}}$ = $\sqrt{38.52}$

= 6.2mm, Diameter is 12.4mm

**Top Feeding for 3mm Plates (No runners and ingates)**

Step 1: W = 0.486kg

Step 2: R = $\frac{\sqrt{0.486}}{1.34+0.217}$ =$\frac{0.697}{1.557}$ =0.447kg/s

$R_a$ = $\frac{R}{K.C}$ =$\frac{0.447}{0.68}$ = 0.657kg/s

t=$\frac{W}{R_a}$ =$\frac{0.486}{0.657}$ = 0.739seconds

Step 3: Hp = H – 0.5 $\frac{h_1^2}{h_2}$ where $h_1$=1mm and $h_2$ =3mm

Hp = 100- 0.5x0.33

= 100-0.165 =99.83mm

Ste 4: Ac = $\frac{0.486}{5956.25}$ =81.59mm$^2$

Radius at choke = $\sqrt{\frac{81.59}{3.1416}}$ = $\sqrt{25.97}$ = 5.09mm. Diameter = 10.1mm

Step 5: $A_1$ = A2 $\frac{\sqrt{150}}{\sqrt{50}}$ =81.59 x 1-73 = 141.1mm$^2$

Sprue inlet radius = $\sqrt{\frac{141.1}{3-1416}}$ = 6.7mm. Diameter = 13.4mm

**Top Feeding for 4mm Plates (No runners and ingates)**

Step 1: W = 0.648kg

Step 2: R = $\frac{\sqrt{0.648}}{1.34+0.290}$ = $\frac{0.8049}{1.63}$ = 0.4938kg/seconds

Ra = $\frac{R}{K.C}$ = $\frac{0.4938}{0.68}$ =0.726kg/s

t = $\frac{0.648}{0.726}$ = 0.892seconds

Step 3: Hp = 100 – 0.5$\frac{1^2}{4}$

Hp = 100-0.125 = 99.875mm

Step 4: Ac = $\frac{0.648}{7191.22}$ = 90.1 mm$^2$

Radius at choke = $\sqrt{\frac{90.1}{3.1416}}$ = 5.35mm. Diameter =10.7mm

Step 5: Area of sprue inlet = $A_2$ $\frac{\sqrt{150}}{\sqrt{50}}$ = 90.1x1.73 = 155.8 mm$^2$

Radius of sprue inlet = $\sqrt{\frac{155.8}{3.1416}}$ = $\sqrt{49.5}$ = 7.03mm. Diameter = 14.07mm

**Bottom/Side Feeding for 2mm Plates**

Step 1: W = 2x0.324 = 0.648kg

Step 2: R = $\frac{\sqrt{0.648}}{1.485}$ = $\frac{0.8049}{1.486}$ = 0.542kg/s

Ra = $\frac{0.542}{0.68}$ = 0.797kg/s

t = $\frac{W}{Ra}$ = $\frac{0.648}{0.797}$ = 0.813seconds

Step 3: Hp = H – 0.5$\frac{1^2}{2}$

= 100 – 0-5x0.5

= 100-0.25

Hp = 99.75mm

Step 4: Ac = $\frac{0.648}{6550.9}$ = $9.89 \times 10^{-5} m^2$ = $98.9 mm^2$

Radius = $\sqrt{\frac{98.9}{3.1416}} = \sqrt{31.48}$ =5-61mm. Diameter = 11.22mm

Sprue Inlet Area = $A_2 \frac{\sqrt{150}}{\sqrt{50}}$ = 98.9 x 1.73 = $171 mm^2$

Radius = $\sqrt{\frac{171}{3.1416}}$ = $\sqrt{54.4}$ = 7.37mm. Diameter = 14.74mm

Step 6: Ingate and Runner cross-sectional Area using gating ratio of 3:2:1

Runner cross-sectional Area = 98.9x2/3 = $65.95 mm^2$

Length of runner = Breadth of runner =8.119mm

Total ingates cross sectional area = 98.9 x 1/3 = 32.96 $mm^2$

There are two mould cavities, so there are two ingates, the cross sectional area of each ingate is

Total plate thickness = 2+2=4mm

$\frac{2}{4}$ x 32.96 = 16.48 $mm^2$

Plate ingate cross section area = 16.48 $mm^2$

Ingate cross sectional area is 2x8.24 $mm^2$

**Bottom/ Side Gating for 3mm Plates**

Step 1: W = 2x0.486kg = 0.972kg

Step 2: R = $\frac{\sqrt{0.985}}{1.557}$ = 0.929kg/s

Ra = $\frac{0.632}{0.68}$ = 0’929kg/s

t = $\frac{W}{R_a}$ 1.05seconds

Step 3; Hp = 100 - $\frac{1^2}{3}$ = 100 – 0.5x.033

Hp= 100-0.165 = 99.83mm

Step 4: Ac = $\frac{0.972}{8462.87}$ = $1.148 \times 10^{-4} m^2$ = $114.8 mm^2$

Radius at Choke = $\sqrt{\frac{114.8}{3.1416}}$ = $\sqrt{36.56}$ = 6.04mm. Diameter = 12.09mm

Step 5: Area of sprue inlet = 114.8 $x \frac{\sqrt{150}}{\sqrt{50}}$ = 114.8x1.43 = $198.6 mm^2$

Radius of sprue inlet = $\sqrt{\frac{198.6}{3.1416}}$ = $\sqrt{63.21}$ = 7.95mm. Diameter = 15.9mm

Step 6: Ingate and Runner cross-sectional Area using gating ratio of 3:2:1

Runner cross-sectional Area = 98.9x2/3 = 65.95mm$^2$

Length of runner = Breadth of runner =8.119mm

Total ingates cross sectional area = 98.9 x 1/3 = 32.96 mm$^2$

There are two mould cavities, so there are two ingates, the cross sectional area of each ingate is determined as follows:

Total plate thickness = 3+3=6mm

$\frac{3}{6}$ x 32.96 = 16.48 mm$^2$

Plate ingate cross section area = 16.48 mm$^2$

Ingate cross sectional area is 3x54.9 mm$^2$

**Bottom/ Side Gating for 4mm Plates**

Step 1 W = 2x0.648 = 1.296kg

Step 2: R = $\frac{\sqrt{1.296}}{1.63}$ = 0.698kg/s

Ra = $\frac{0.698}{0.68}$ = 1.026kg/s

t = $\frac{1.296}{1.026}$ = 1.263seconds

Step 3: Hp = 100 – 0.5$\frac{1^2}{4}$

Hp = 100 – 0.125 = 99.875mm

Ac = $\frac{1.296}{10182.2}$ = 1.272 x 10$^{-4}$m$^2$ = 127.2mm$^2$

Radius at choke = $\sqrt{\frac{127.2}{3.1416}}$ = $\sqrt{40.48}$ = 6.36mm. Diameter = 12.72mm

$A_1 = A_2\frac{\sqrt{150}}{\sqrt{50}}$ = 127.2 x 1.73 = 220.05mm$^2$

Radius at sprue inlet = $\sqrt{\frac{220.5}{3.1416}}$ = $\sqrt{70.04}$ = 8.37mm. Diameter = 16.73mm

Step 6: Ingate and Runner cross-sectional Area using gating ratio of 3:2:1

Runner cross-sectional Area = 98.9x2/3 = 65.95mm$^2$

Length of runner = Breadth of runner =8.119mm

Total ingates cross sectional area = 98.9 x 1/3 = 32.96 mm$^2$

There are two mould cavities, so there are two ingates, the cross sectional area of each ingate is determined as follows:

Total plate thickness = 4+4=8mm

$\frac{4}{8}$ X 32.96 = 16.48 mm$^2$

Plate ingate cross section area = 16.48 mm$^2$

Ingate cross sectional area is 4 x 4.12mm$^2$

**Nodularity and Nodule Count Calculations**

$$\text{Nodularity \%} = \frac{\text{area (number) of acceptable particles}}{\text{area (number) of all particles}} \text{ x } 100 \qquad \text{(A7)}$$

## APPENDIX B

Table B1: Dimension of Pattern Plates

| Thickness(mm) | Length(mm) | Width(mm) | Volume($mm^3$) | Weight(Kg) |
|---|---|---|---|---|
| 2 | 150 | 150 | 45,000 | 0.324 |
| 3 | 150 | 150 | 67,500 | 0.486 |
| 4 | 150 | 150 | 90,000 | 0.648 |

Table B2: Chemical Composition of Aluminium Dross
(Quality Control Department, Aluminium Rolling Mill, Ota. Ogun State Nigeria)

| Const. | $Al_2O_3$ | $SiO_2$ | MgO | NaO | $K_2O$ | CaO | $Fe_2O_3$ | Sulpha | Chlorid | Al |
|---|---|---|---|---|---|---|---|---|---|---|
| Wt. % in RHA | 43.38 | 3.12 | 0.12 | 9.84 | 0.72 | 1.57 | 0.70 | 0.60 | 1.98 | 37.97 |

Table B3: Chemical Composition of Rice Husk Ash

| Const. | $SiO_2$ | $Al_2O_3$ | $TiO_2$ | $Fe_2O_3$ | CaO | MgO | $K_2O$ | $Na_2O$ | LOI |
|---|---|---|---|---|---|---|---|---|---|
| Wt. % in RHA | 93.15 | 0.21 | 0 | 0.21 | 0.41 | 0.45 | 3.21 | 0 | 2.36 |

Table B4: BHN responses of cast TWDI samples with sprue height

| | | **Sprue Height (mm)** | | | | | |
|---|---|---|---|---|---|---|---|
| **TWDI Sample Thickness (mm)** | 50 | 100 | 150 | 200 | 250 | 300 | 350 |
| 2 | 153 | 141 | 145 | 148 | 160 | 169 | 198 |
| 3 | 142 | 124 | 139 | 140 | 148 | 164 | 193 |
| 4 | 151 | 129 | 131 | 147 | 169 | 207 | 215 |

Table B5: UTS (MPa) of cast TWDI samples with sprue height

| | | **Sprue Height (mm)** | | | | | |
|---|---|---|---|---|---|---|---|
| **TWDI Sample Thickness (mm)** | 50 | 100 | 150 | 200 | 250 | 300 | 350 |
| 2 | 181 | 596 | 503 | 411 | 233 | 190 | 101 |
| 3 | 136 | 578 | 486 | 436 | 293 | 167 | 123 |
| 4 | 153 | 651 | 627 | 432 | 309 | 183 | 134 |

Table B6: Percent elongation of cast TWDI samples with Sprue Height

| | | **Sprue Height (mm)** | | | | | |
|---|---|---|---|---|---|---|---|
| **TWDI Sample Thickness (mm)** | 50 | 100 | 150 | 200 | 250 | 300 | 350 |
| 2 | 0.4 | 2.2 | 2.0 | 1.2 | 0.4 | 0.3 | 0.3 |
| 3 | 0.5 | 2.3 | 2.2 | 1.6 | 0.7 | 0.5 | 0.2 |
| 4 | 0.5 | 4.4 | 1.9 | 1.6 | 0.7 | 0.4 | 0.3 |

Table B7: BHN values of cast TWDI samples with Treatment Temperature.

| | | **Treatment Temp.($^0$C)** | | | | | |
|---|---|---|---|---|---|---|---|
| **TWDI Sample Thickness (mm)** | **1430** | **1450** | **1470** | **1490** | **1510** | **1530** | **1550** |
| 2 | 101 | 123 | 105 | 90 | 115 | 113 | 108 |
| 3 | 118 | 139 | 118 | 112 | 118 | 117 | 106 |
| 4 | 116 | 172 | 104 | 114 | 111 | 112 | 115 |

Table B8: UTS of cast TWDI samples with Treatment Temperature

| | | **Treatment Temp.($^0$C)** | | | | | |
|---|---|---|---|---|---|---|---|
| **TWDI Sample Thickness (mm)** | **1430** | **1450** | **1470** | **1490** | **1510** | **1530** | **1550** |
| 2 | 250 | 389 | 274 | 187 | 264 | 177 | 244 |
| 3 | 331 | 409 | 397 | 191 | 386 | 140 | 270 |
| 4 | 329 | 514 | 248 | 355 | 323 | 321 | 330 |

Table B9: Percent elongation of cast TWDI samples with treatment temperature

| | | **Treatment Temp.($^0$C)** | | | | | |
|---|---|---|---|---|---|---|---|
| **TWDI Sample Thickness (mm)** | **1430** | **1450** | **1470** | **1490** | **1510** | **1530** | **1550** |
| 2 | 1.2 | 2.6 | 1.8 | 1.6 | 1.2 | 1.0 | 0.7 |
| 3 | 1.3 | 2.9 | 1.8 | 1.5 | 1.3 | 1.0 | 0.8 |
| 4 | 1.5 | 3.0 | 2.1 | 1.6 | 1.4 | 1.1 | 0.8 |

Table B10: Effect of the Aluminium Dross Additive on moulding sand properties

| S/No | wt% Al. Dross | Green Shear Str. (KN/m$^2$) | Permeability (cm/s) | % Compact. | Moist. Content (%) | Shatter Index (%) |
|---|---|---|---|---|---|---|
| D | 0 | 89(65-120) | 130(70-130) | 78.5(40-80) | 4.0(2.8-4.0) | 69(65-100) |
| D1 | 2 | 82 | 162 | 70 | 4.0 | 68.8 |
| D2 | 4 | 75 | 160 | 65 | 4.0 | 68.6 |
| D3 | 6 | 61 | 156 | 61 | 4.0 | 68.4 |
| D4 | 8 | 57 | 141 | 53 | 4.2 | 68.4 |
| D5 | 10 | 52 | 134 | 42 | 4.2 | 68.2 |
| D6 | 12 | 48 | 122 | 39 | 4.2 | 66.8 |

Table B11: Effect of Aluminium Dross Additive on thermal conductivity of sand mix

| S/No | Wt% Al. Dross | Temp.($^0$C) | Thermal conductivity (W/m.K) |
|---|---|---|---|
| 1 | D | 29.00 | 1.631 |
| 2 | D1 | 28.83 | 1.654 |
| 3 | D2 | 28.63 | 1.720 |
| 4 | D3 | 28.63 | 1.787 |
| 5 | D4 | 28.39 | 1.753 |
| 6 | D5 | 28.83 | 1.718 |
| 7 | D6 | 28.63 | 1.540 |

Table B12: BHN results of cast TWDI samples with wt. % Al. Dross

| | | **Weight % Al. Dross** | | | | | |
|---|---|---|---|---|---|---|---|
| **TWDI Sample Thickness (mm)** | **0** | **2** | **4** | **6** | **8** | **10** | **12** |
| 2 | 179 | 26 | 37 | 48 | 55 | 47 | 67 |
| 3 | 195 | 30 | 33 | 63 | 52 | 52 | 54 |
| 4 | 123 | 25 | 48 | 69 | 63 | 42 | 71 |

Table B13: UTS (MPa) results of cast TWDI samples with wt. % Al. Dross

| | | **Weight % Al. Dross** | | | | | |
|---|---|---|---|---|---|---|---|
| **TWDI Sample Thickness (mm)** | **0** | **2** | **4** | **6** | **8** | **10** | **12** |
| 2 | 248 | 148 | 115 | 76 | 172 | 143 | 208 |
| 3 | 300 | 197 | 100 | 89 | 159 | 158 | 168 |
| 4 | 389 | 215 | 150 | 75 | 195 | 145 | 221 |

Table B14: Percent Elongation of cast TWDI samples with wt. % Al. Dross

| | | **Weight % Al. Dross** | | | | | |
|---|---|---|---|---|---|---|---|
| **TWDI Sample Thickness (mm)** | **0** | **2** | **4** | **6** | **8** | **10** | **12** |
| 2 | 2.1 | 1.9 | 2.5 | 0.8 | 2.6 | 3.6 | 4.5 |
| 3 | 3.2 | 2.8 | 3.0 | 1.0 | 2.8 | 5.5 | 7.3 |
| 4 | 4.2 | 3.1 | 3.1 | 1.6 | 2.6 | 5.8 | 4.7 |

Table B15: Effect of the RHA (Rice Husk Ash) Additive on moulding sand properties

| S/No | Specimen wt% RHA | Green Shear Str. ($KN/m^2$) | Permeability cm/s | % Comp. | Moist. Content % | Shatter Index % |
|---|---|---|---|---|---|---|
| 1 | R | 89(65-120) | 130(70-130) | 78.5(40-80) | 4.0(2.8-4.0) | 69(65-100) |
| 2 | R1 | 97 | 110 | 53.8 | 2.8 | 66.8 |
| 3 | R2 | 94 | 90 | 49.25 | 2.8 | 66.2 |
| 4 | R3 | 90 | 72 | 42 | 2.8 | 64.4 |
| 5 | R4 | 78 | 68 | 39 | 2.8 | 64.0 |
| 6 | R5 | 68 | 65 | 36 | 2.8 | 62.8 |
| 7 | R6 | 64 | 60 | 33 | 2.8 | 60.2 |

Table B16: Effect of Rice Husk Ash (RHA) additive on thermal conductivity of sand mix

| S/No | Specimen wt% RHA | Temp.($^0C$) | Thermal conductivity(W/m. K) |
|---|---|---|---|
| 1 | R | 29.00 | 1.631 |
| 2 | R1 | 28.89 | 1.502 |
| 3 | R2 | 28.90 | 1.327 |
| 4 | R3 | 28.81 | 1.149 |
| 5 | R4 | 28.89 | 1.073 |
| 6 | R5 | 28.72 | 0.996 |
| 7 | R6 | 28.74 | 0.921 |

Table B17: BHN results of cast TWDI samples with wt. % RHA

| | | **Weight % RHA** | | | | | |
|---|---|---|---|---|---|---|---|
| **TWDI Sample Thickness (mm)** | **0** | **1** | **2** | **3** | **4** | **5** | **6** |
| 2 | 179 | 127 | 123 | 131 | 189 | 157 | 137 |
| 3 | 195 | 131 | 150 | 154 | 207 | 192 | 171 |
| 4 | 123 | 125 | 158 | 161 | 219 | 201 | 181 |

Table B18: UTS (MPa) results of cast TWDI samples with wt. % RHA

| | | **Weight % RHA** | | | | | |
|---|---|---|---|---|---|---|---|
| **TWDI Sample Thickness (mm)** | **0** | **1** | **2** | **3** | **4** | **5** | **6** |
| 2 | 248 | 250 | 329 | 339 | 564 | 441 | 383 |
| 3 | 300 | 309 | 420 | 435 | 575 | 567 | 552 |
| 4 | 389 | 397 | 486 | 496 | 596 | 573 | 567 |

Table B19: Percent Elongation of cast TWDI samples with wt. % RHA

| | | **Weight % RHA** | | | | | |
|---|---|---|---|---|---|---|---|
| **TWDI Sample Thickness (mm)** | **0** | **1** | **2** | **3** | **4** | **5** | **6** |
| 2 | 2.1 | 2.3 | 3.0 | 3.3 | 3.5 | 3.9 | 4.7 |
| 3 | 3.2 | 3.6 | 3.8 | 4.0 | 4.3 | 4.9 | 5.8 |
| 4 | 4.2 | 4.5 | 4.7 | 4.8 | 5.0 | 5.2 | 6.1 |

Table B20: Nodularity and nodule count calculations for Gating sprue height samples

| **No** | **Sample** | **Nodularity (%)** | **Nodule Count (nodules/mm$^2$)** |
|---|---|---|---|
| 1 | A12 | $\frac{55}{70}$ = 78.5 | 55 |
| 2 | A13 | $\frac{105}{115}$ = 91.3 | 105 |
| 3 | A14 | $\frac{190}{208}$ = 91.3 | 190 |
| 4 | A22 | $\frac{140}{180}$ = 77.7 | 140 |
| 5 | A23 | $\frac{125}{180}$ = 69.4 | 125 |
| 6 | A24 | $\frac{152}{198}$ = 76.7 | 152 |
| 7 | A32 | $\frac{200}{230}$ = 86.9 | 200 |
| 8 | A33 | $\frac{260}{283}$ = 91.87 | 260 |
| 9 | A34 | $\frac{149}{195}$ = 76.4 | 149 |
| 10 | A42 | $\frac{520}{575}$ = 90.4 | 520 |
| 11 | A43 | $\frac{480}{496}$ = 96.7 | 480 |
| 12 | A44 | $\frac{420}{441}$ = 95.2 | 420 |
| 13 | A52 | $\frac{401}{427}$ = 93.9 | 401 |
| 14 | A53 | $\frac{347}{355}$ = 97.7 | 347 |
| 15 | A54 | $\frac{396}{401}$ = 98.7 | 396 |
| 16 | A62 | $\frac{1364}{1380}$ = 98.8 | 1364 |
| 17 | A63 | $\frac{463}{481}$ = 96.2 | 463 |
| 18 | A64 | $\frac{546}{552}$ = 98.9 | 546 |
| 19 | A72 | $\frac{22}{53}$ = 41.5 | 22 |
| 20 | A73 | $\frac{64}{139}$ = 46.0 | 64 |
| 21 | A74 | $\frac{17}{51}$ = 33.3 | 17 |

Table B21: Nodularity and nodule count calculations for Treatment temperature Samples

| No | Sample | Nodularity (%) | Nodule Count (nodules/mm$^2$) |
|---|---|---|---|
| 1 | T12 | $\frac{184}{194}$ = 93.4 | 184 |
| 2 | T13 | $\frac{121}{169}$ = 71 | 121 |
| 3 | T14 | $\frac{65}{97}$ = 67 | 65 |
| 4 | T22 | $\frac{192}{336}$ = 57.1 | 192 |
| 5 | T23 | $\frac{387}{534}$ = 72.4 | 387 |
| 6 | T24 | $\frac{57}{107}$ = 53.2 | 57 |
| 7 | T32 | $\frac{180}{250}$ = 72 | 180 |
| 8 | T33 | $\frac{113}{168}$ = 67.2 | 113 |
| 9 | T34 | $\frac{276}{343}$ = 80.4 | 276 |
| 10 | T42 | $\frac{416}{441}$ = 94 | 416 |
| 11 | T43 | $\frac{311}{365}$ = 85.2 | 311 |
| 12 | T44 | $\frac{484}{525}$ = 92.1 | 484 |
| 13 | T52 | $\frac{543}{581}$ = 93.4 | 543 |
| 14 | T53 | $\frac{521}{564}$ = 92.3 | 521 |
| 15 | T54 | $\frac{271}{282}$ = 96 | 271 |
| 16 | T62 | $\frac{610}{619}$ = 98.5 | 610 |
| 17 | T63 | $\frac{512}{538}$ = 95.1 | 512 |
| 18 | T64 | $\frac{458}{470}$ = 97.4 | 458 |
| 19 | T72 | $\frac{97}{142}$ = 68.3 | 97 |
| 20 | T73 | $\frac{77}{93}$ = 82.7 | 77 |
| 21 | T74 | $\frac{59}{74}$ = 79.7 | 59 |

B22: Nodularity and nodule count calculations for moulding sand-RHA cast samples

| **No** | **Sample** | **Nodularity (%)** | **Nodule Count (nodules/mm$^2$)** |
|---|---|---|---|
| 1 | RH2 | $\frac{341}{405}$ = 84.1 | 341 |
| 2 | RH3 | $\frac{361}{431}$ = 83.7 | 361 |
| 3 | RH4 | $\frac{347}{461}$ = 75.2 | 347 |
| 4 | RH12 | $\frac{678}{691}$ = 98.1 | 678 |
| 5 | RH13 | $\frac{497}{521}$ = 95.3 | 497 |
| 6 | RH14 | $\frac{364}{388}$ = 93.8 | 364 |
| 7 | RH22 | $\frac{547}{560}$ = 97.6 | 547 |
| 8 | RH23 | $\frac{533}{549}$ = 97.0 | 533 |
| 9 | RH24 | $\frac{627}{641}$ = 97.8 | 627 |
| 10 | RH32 | $\frac{721}{805}$ = 89.5 | 721 |
| 11 | RH33 | $\frac{544}{561}$ = 96.9 | 544 |
| 12 | RH34 | $\frac{496}{515}$ = 96.3 | 496 |
| 13 | RH42 | $\frac{1376}{1418}$= 97.0 | 1376 |
| 14 | RH43 | $\frac{1458}{1500}$ = 97.2 | 1458 |
| 15 | RH44 | $\frac{521}{540}$ = 96.4 | 521 |
| 16 | RH52 | $\frac{1693}{1738}$=97.4 | 1693 |
| 17 | RH53 | $\frac{1431}{1449}$ = 98.7 | 1431 |
| 18 | RH54 | $\frac{1373}{1388}$ = 98.9 | 1373 |
| 19 | RH62 | $\frac{1974}{2008}$ = 98.3 | 1974 |
| 20 | RH63 | $\frac{1521}{1568}$= 97.0 | 1521 |
| 21 | RH64 | $\frac{1344}{1410}$ = 95.3 | 1344 |

## APPENDIX C

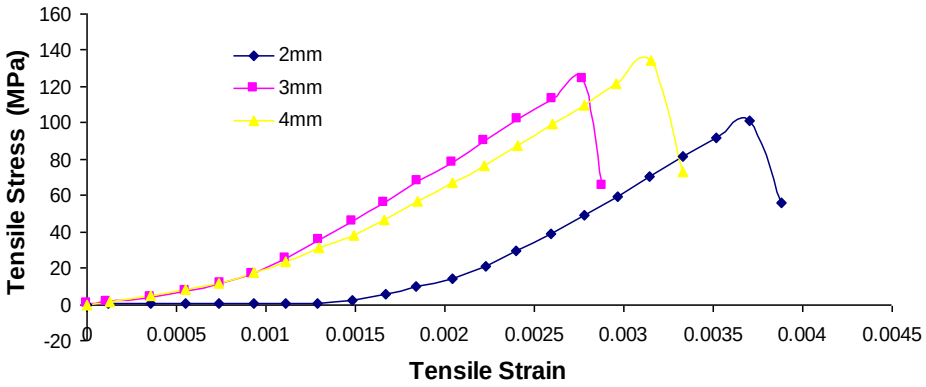


Figure C1: Stress versus Strain curve for A1 (Sprue Height 350mm) samples.

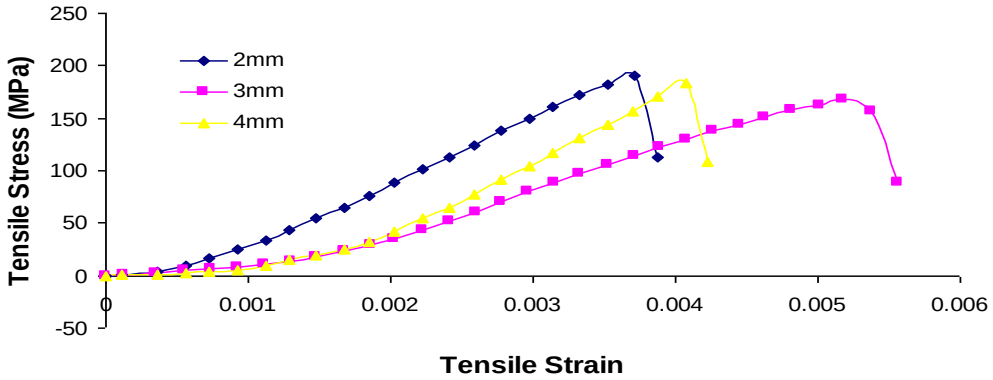


Figure C2: Stress versus Strain curve for A2 (Sprue Height 300mm) samples

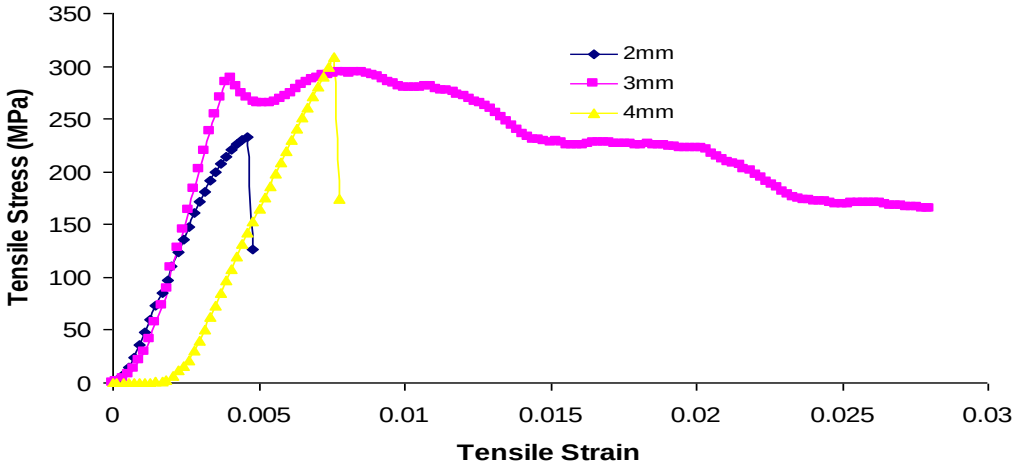


Figure C3: Stress versus Strain curve for A3 (Sprue Height 250mm) samples

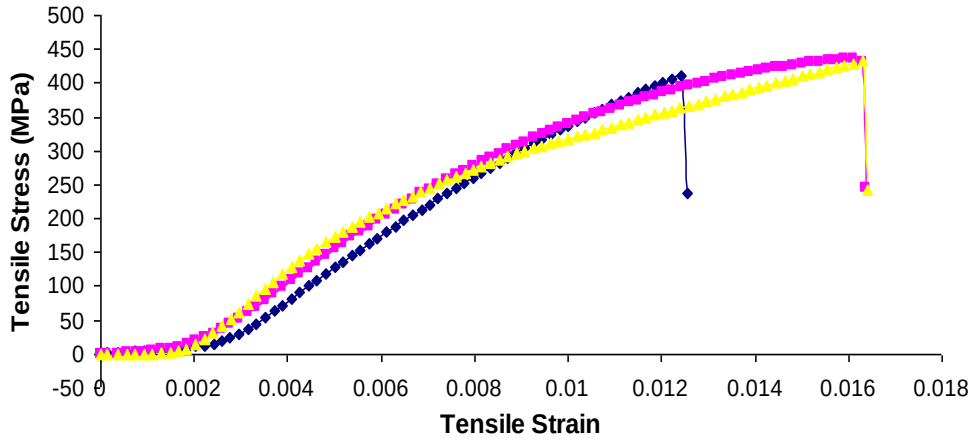


Figure C4: Stress versus Strain curve for A4 (Sprue Height 200mm) samples

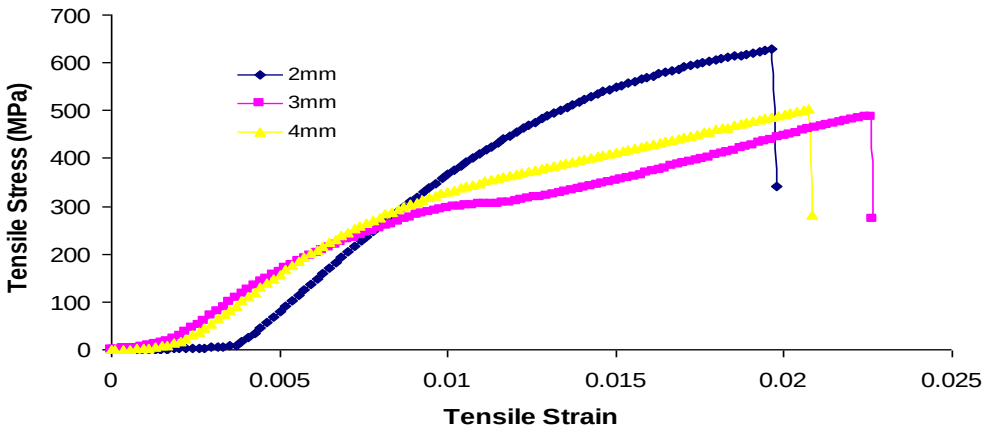


Figure C5: Stress versus Strain curve for A5 (Sprue Height 150mm) samples

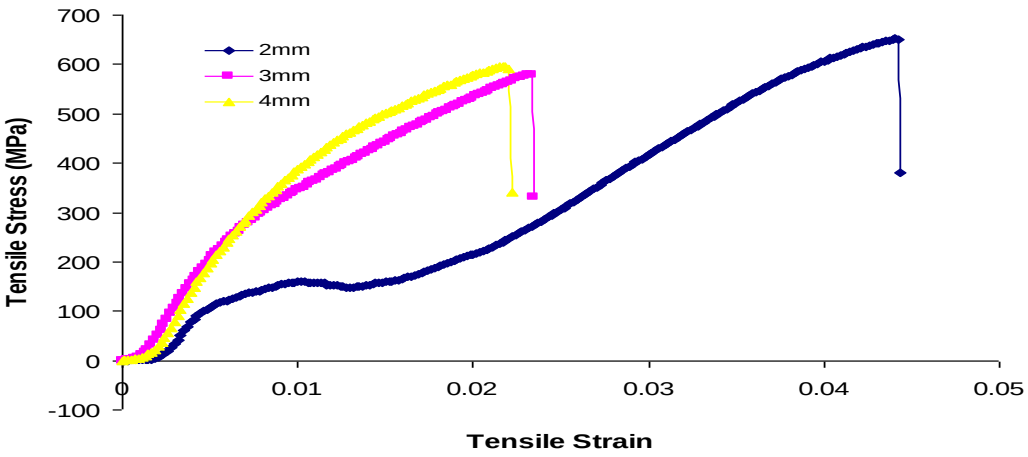


Figure C6: Stress versus Strain curve for A6 (Sprue Height 100mm) samples

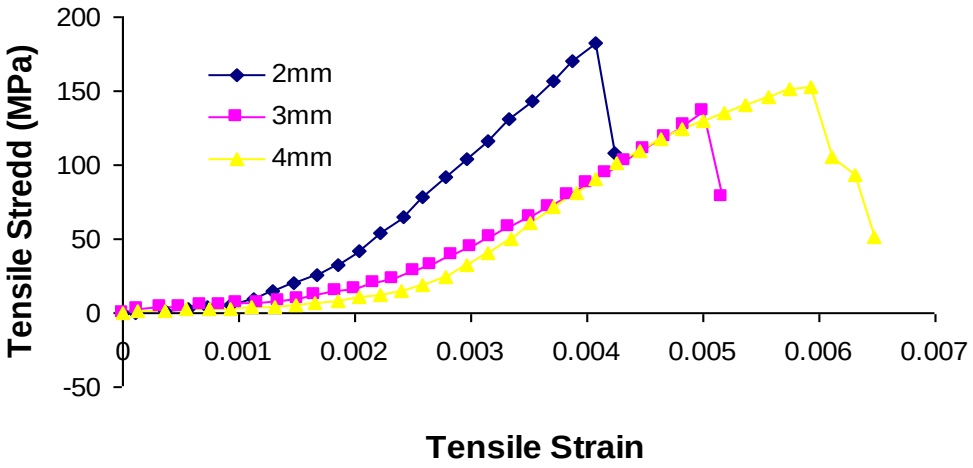


Figure C7: Stress versus Strain curve for A7 (Sprue Height 50mm) samples

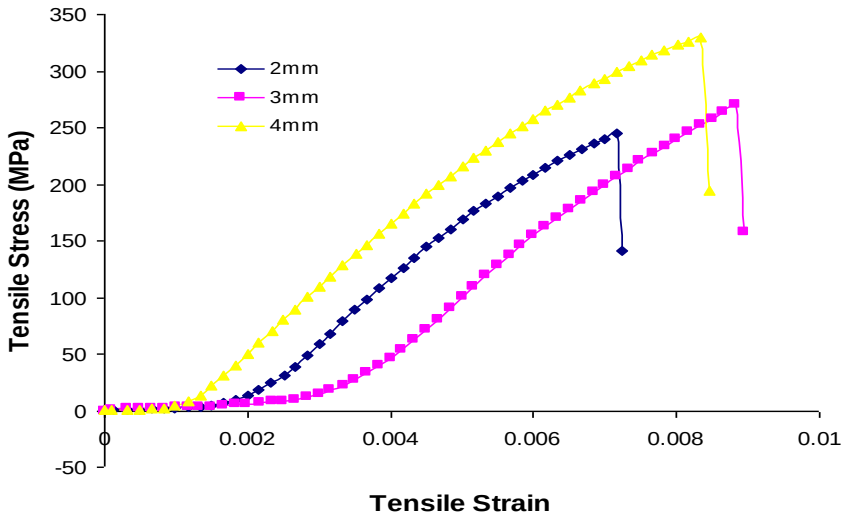


Figure C8: Stress Strain curve for T1 Samples

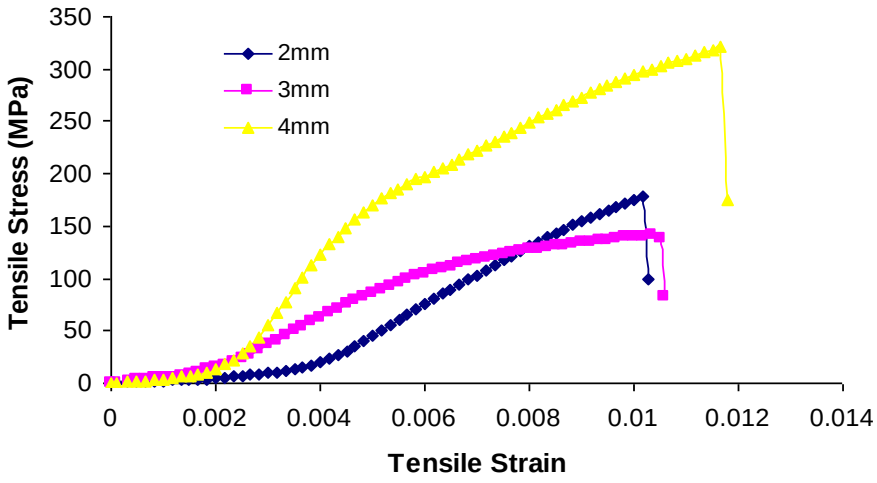


Figure C9: Stress Strain curve for T2 Samples

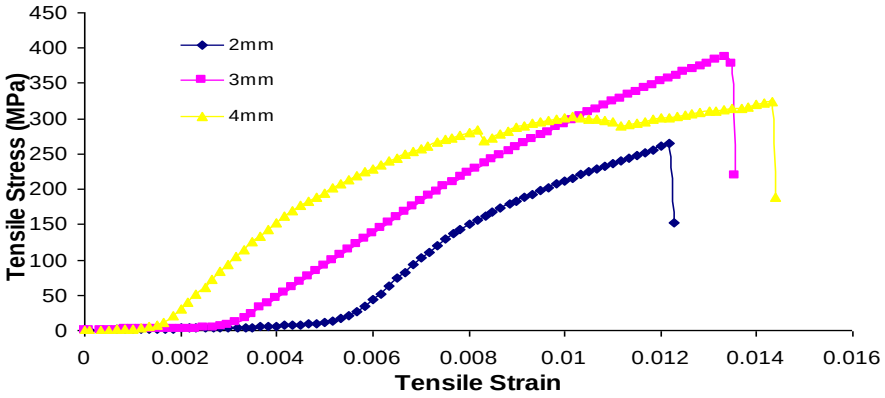


Figure C10: Stress Strain curve for T3 Samples

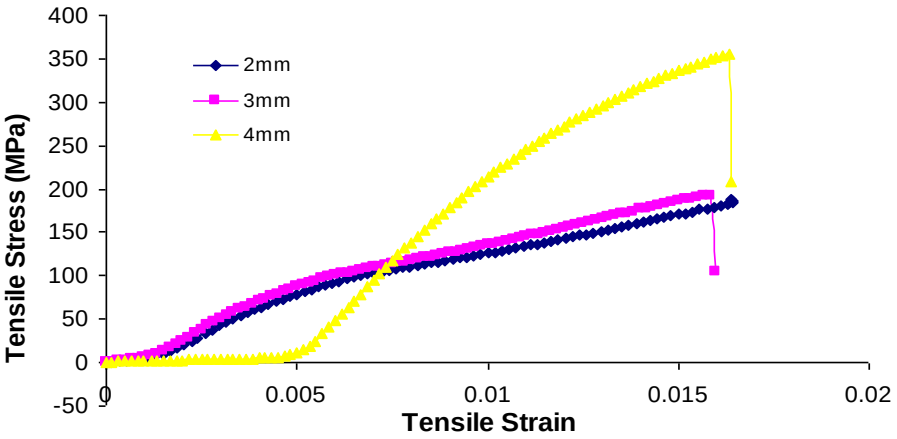


Figure C11: Stress Strain curve for T4 Samples

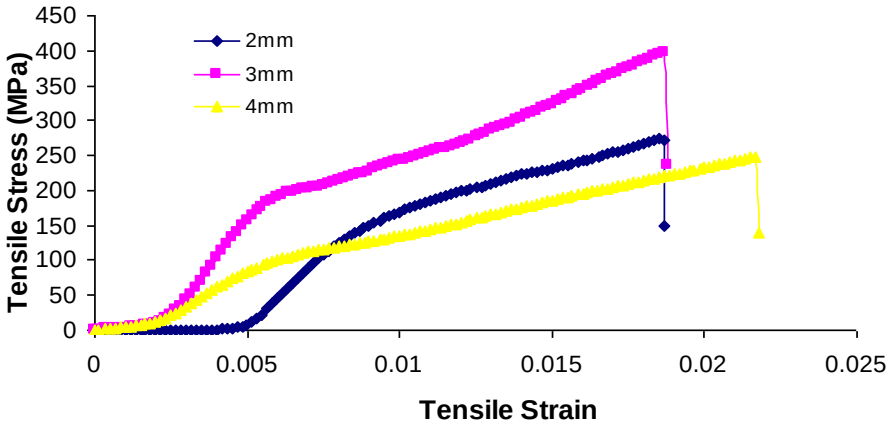


Figure C12: Stress Strain curve for T5 Samples

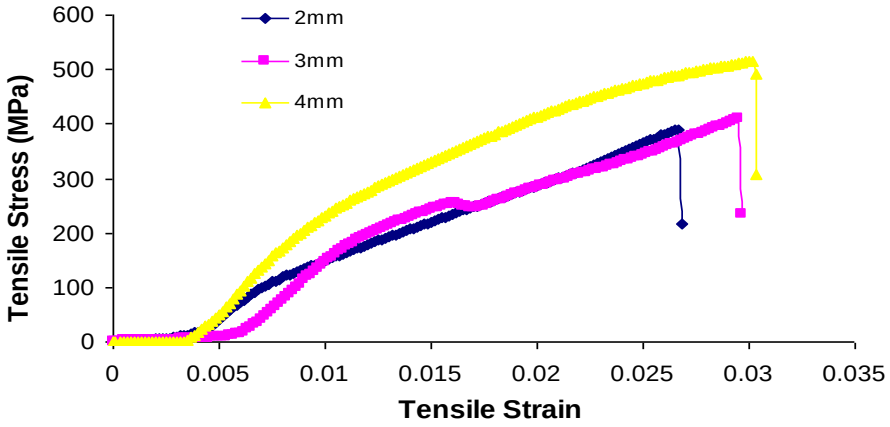


Figure C13: Stress Strain curve for T6 Samples

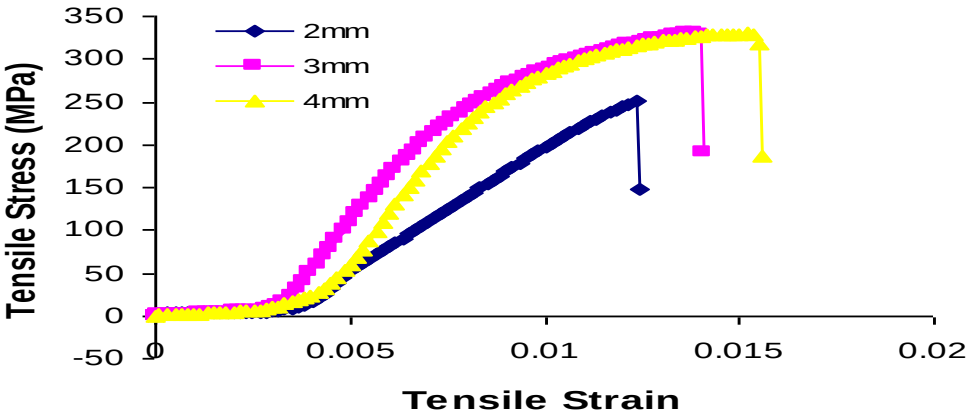


Figure C14: Stress Strain curve for T7 Samples

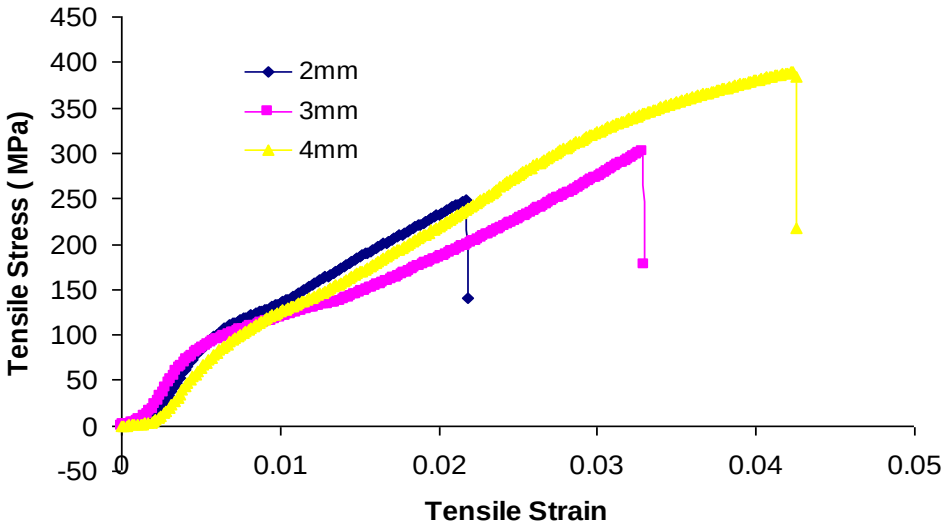


Figure C15: Stress versus strain curve for D Samples (0 wt% Al.Dr)

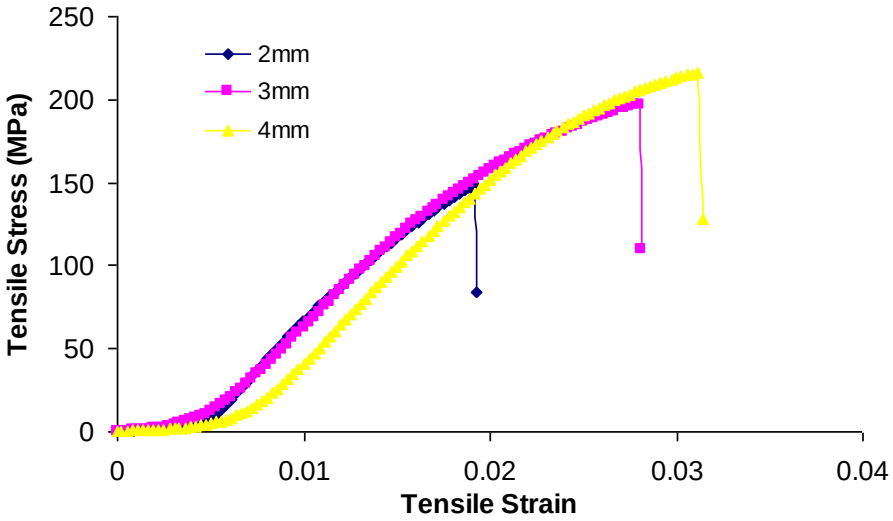


Figure C16: Stress versus strain curve for D1 samples (2wt% Al.Dr)

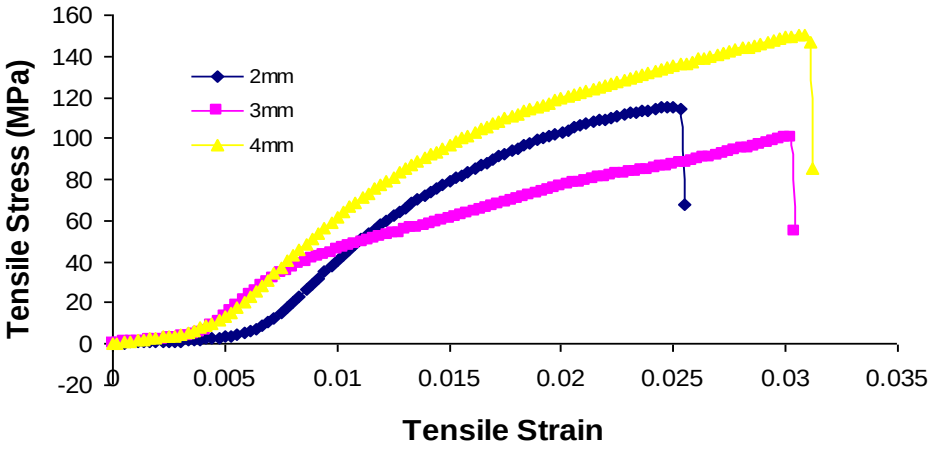


Figure C17: Stress versus strain curve for D2 Samples (4wt% Al.Dr)

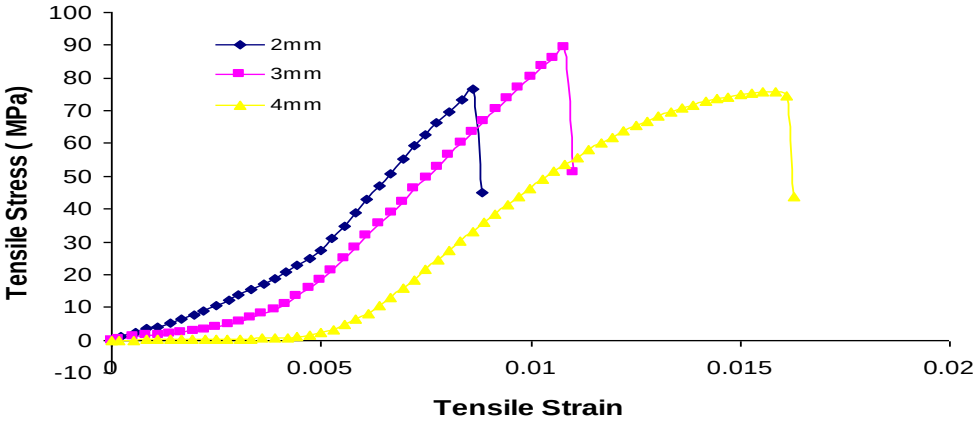


Figure C18: Stress versus strain curve for D3 Samples (6wt% Al.Dr)

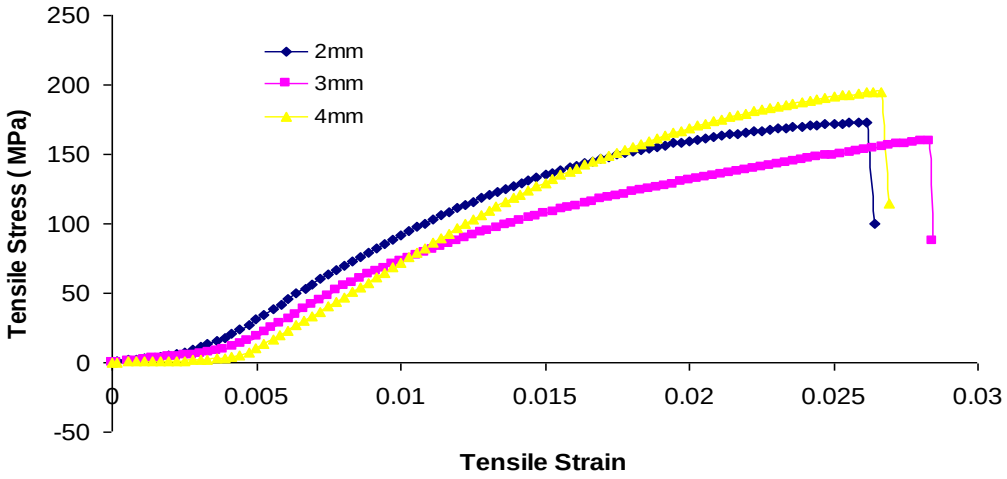


Figure C19: Stress versus strain curve for D4 Samples (8wt% Al.Dr)

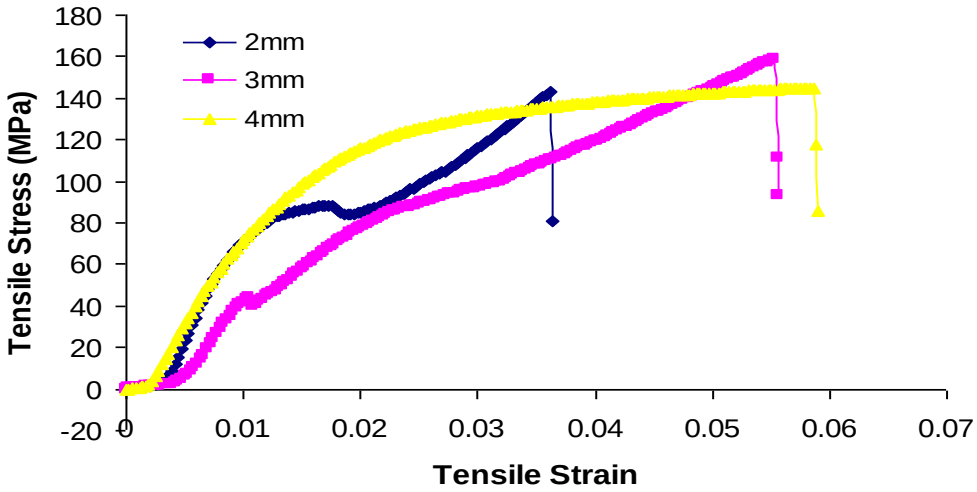


Figure C20: Stress versus strain curve for D5 Samples (10wt% Al.Dr)

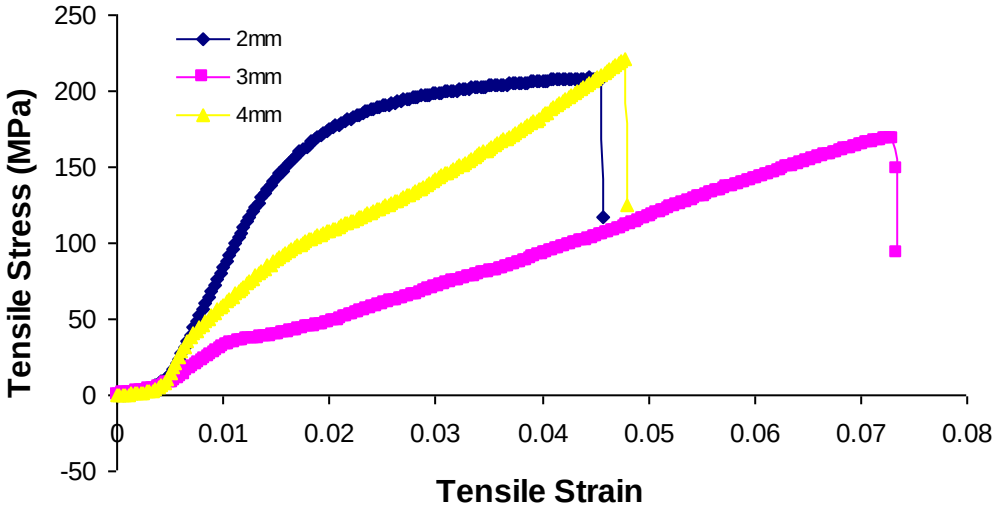


Figure C21: Stress versus strain curve for D6 Samples (12wt% Al.Dr)

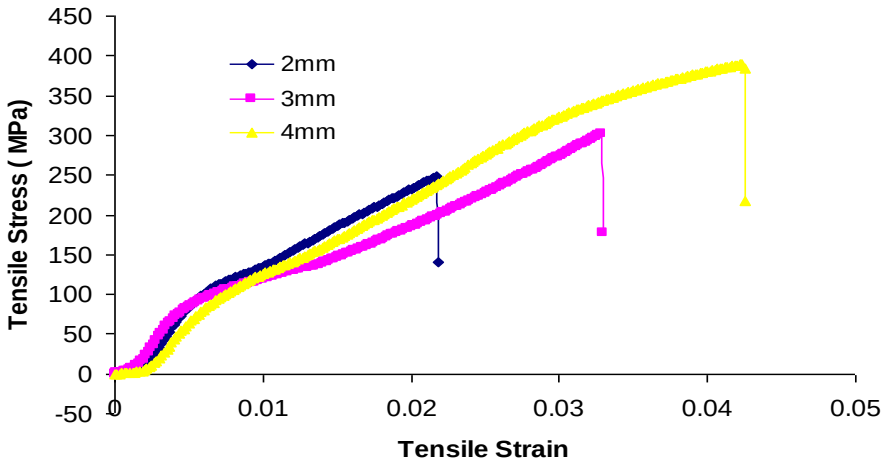


Figure C22: Stress versus strain curve for RH Samples (0 wt. % RHA)

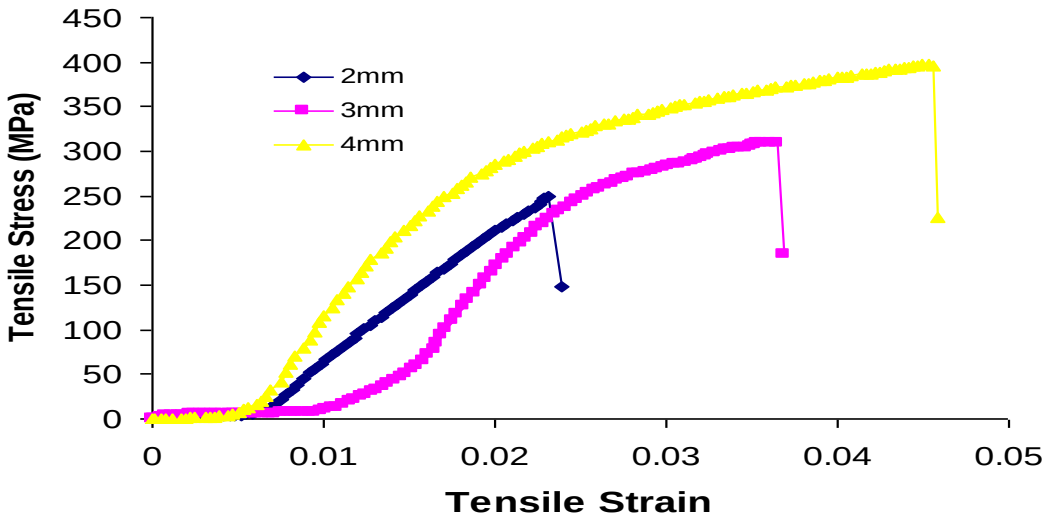


Figure C23: Stress versus strain curve for RH1 Samples (1wt. % RHA)

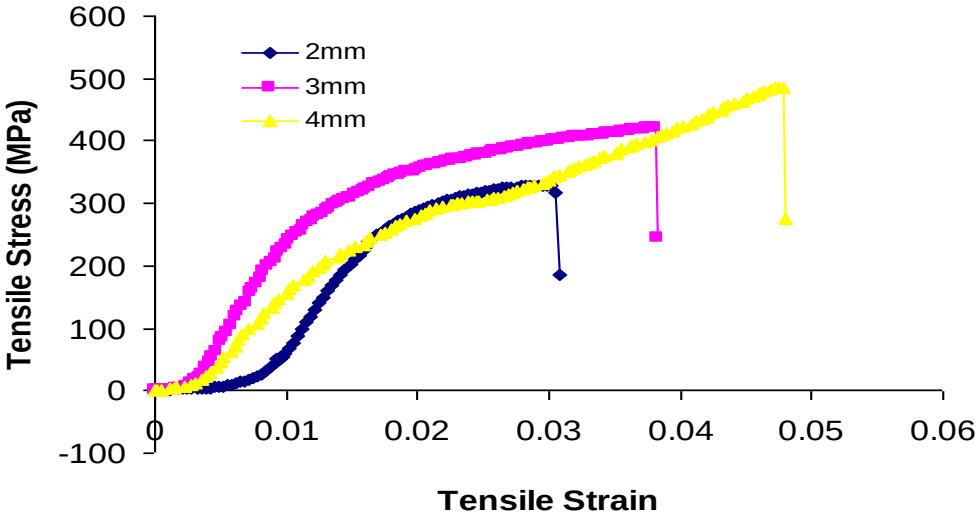


Figure C24: Stress versus strain curve for RH2 Samples (2 wt. % RHA)

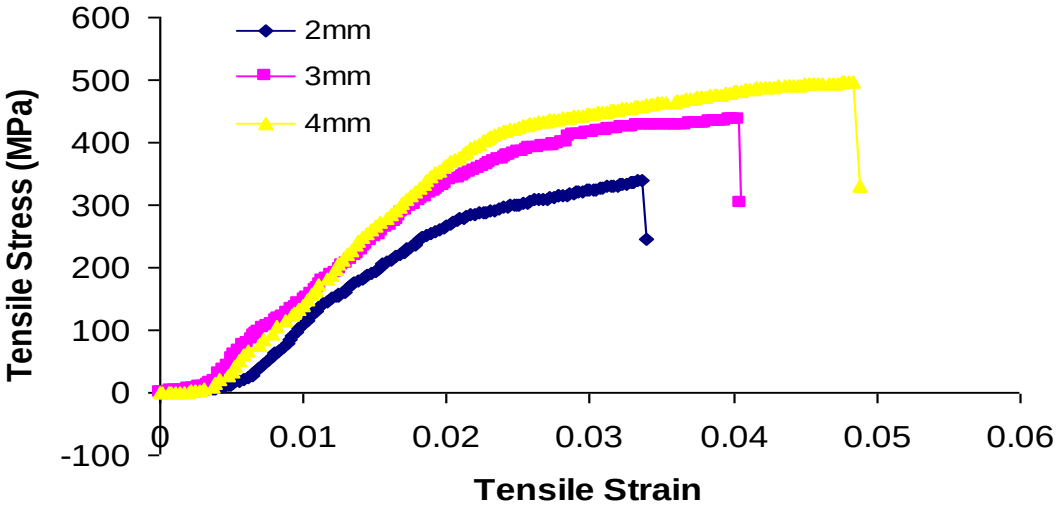


Figure C25: Stress versus strain curve for RH3 Samples (3 wt % RHA)

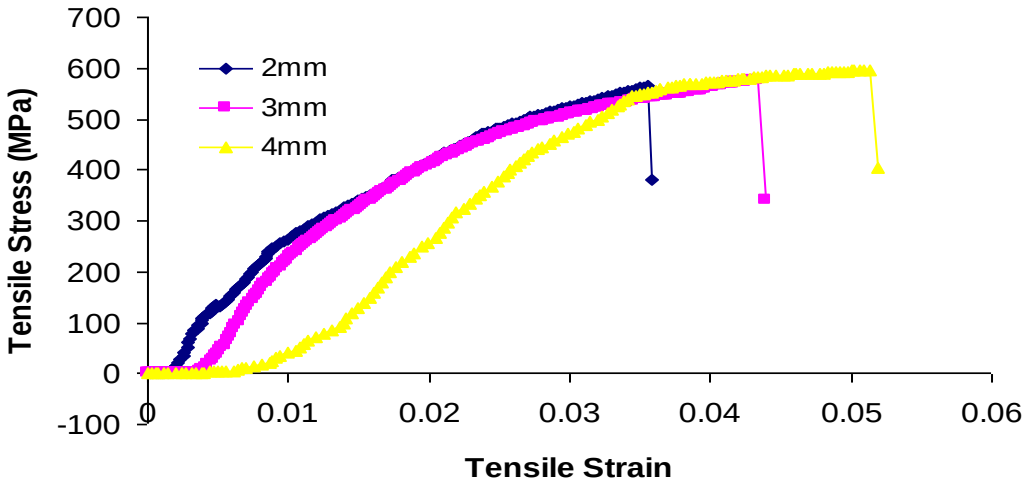


Figure C26: Stress versus strain curve for RH4 Samples (4wt. % RHA)

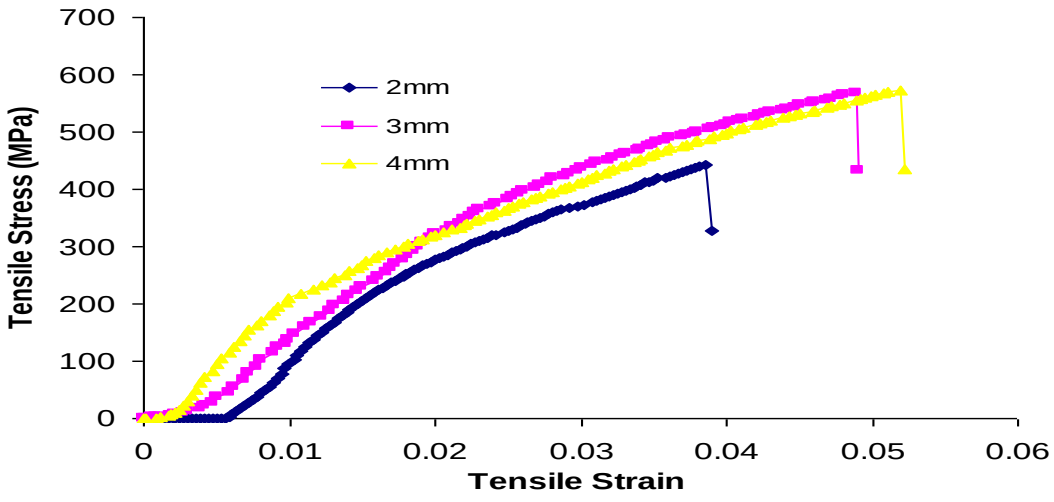


Figure C27: Stress versus strain curve for RH5 Samples (5 wt. % RHA)

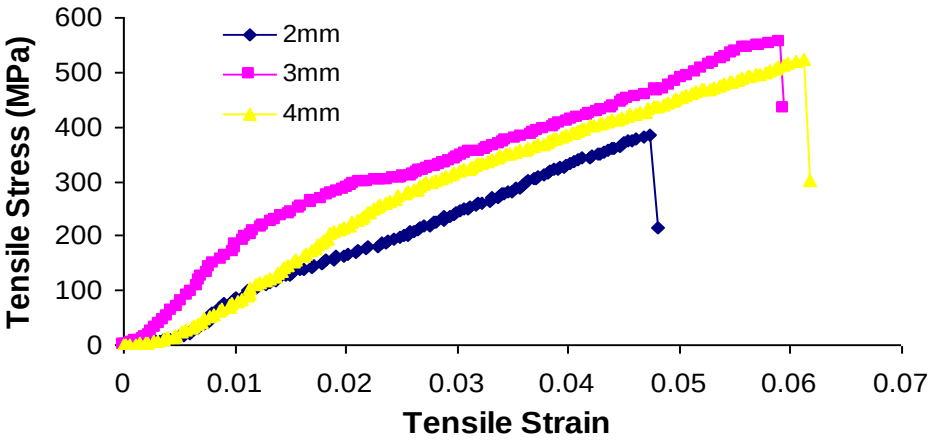


Figure C28: Stress versus strain curve for RH6 Samples (6 wt. % RHA)